ABSTRACT

UNDERWATER COMMUNICATION VIA PARTICLE VELOCITY CHANNELS: PRINCIPLES, CHANNEL MODELS, AND SYSTEM DESIGN

by
Huaihai Guo

A vector sensor is capable of measuring important non-scalar components of the acoustic field such as the particle velocity, which cannot be obtained by a single scalar pressure sensor. In the past few decades, extensive research has been conducted on the theory and design of vector sensors. On the other hand, underwater acoustic communication systems have been relying on scalar sensors only, which measure the pressure of the acoustic field. By taking advantage of the vector components of the acoustic field, such as the particle velocity, the vector sensor can be used for detecting the transmitted data. In this dissertation, the concept of data detection and equalization in underwater particle velocity channels using acoustic vector sensors was developed. System equations for such a receiver were derived and channel equalization using these sensors was formulated. A multiuser system using vector sensors and space time block codes was also developed, which does not use spreading codes and bandwidth expansion. This is particularly important in bandlimited underwater channels.

With regard to channel models for particle velocity channels, characterization of particle velocity channels and their impact on vector sensor communication systems performance were therefore of interest. In multipath channels such as shallow waters, a vector sensor receives the signal through several paths and each path has a different delay (travel time). Motion of the transmitter or receiver in a multipath channel introduces different Doppler shifts as well. Those introduce different levels of correlation in an array of vector sensors. Therefore, in this dissertation, a statistical framework for mathematical characterization of different types of correlations in acoustic vector sensor arrays was developed. Exact and closed-form approximation correlation expressions were derived

which related signal correlations to some key channel parameters such as mean angle of arrivals and angle spreads. Using these expressions, the correlations between the pressure and velocity channels of the sensors could be calculated, in terms of element spacing, frequency and time separation. The derived closed-form parametric expressions for the signal correlations can serve as useful tools to estimate some important physical parameters as well.

Knowledge of the delay and Doppler spreads in acoustic particle velocity channel is also important for efficient design of underwater vector sensor communication system. In this dissertation, these channel spreads were characterized using the zero crossing rates of channel responses in frequency and time domain. Useful expressions for delay and Doppler spreads were derived in terms of the key channel parameters, mean angle of arrivals and angle spreads. These results are needed for design and performance predication of communication systems in time-varying and frequency-selective underwater particle velocity channels.

UNDERWATER COMMUNICATION VIA PARTICLE VELOCITY CHANNELS: PRINCIPLES, CHANNEL MODELS, AND SYSTEM DESIGN

by
Huaihai Guo

A Dissertation
Submitted to the Faculty of
New Jersey Institute of Technology
in Partial Fulfillment of the Requirements for the Degree of
Doctor of Philosophy in Electrical Engineering

Department of Electrical and Computer Engineering

January 2011

APPROVAL PAGE

UNDERWATER COMMUNICATION VIA PARTICLE VELOCITY CHANNELS: PRINCIPLES, CHANNEL MODELS, AND SYSTEM DESIGN

Huaihai Guo

_____

Dr. Ali Abdi, Dissertation Advisor Date
Associate Professor, Electrical and Computer Engineering Department, NJIT

_____

Dr. Alexander M. Haimovich, Committee Member Date
Professor, Electrical and Computer Engineering Department, NJIT

_____

Dr. Hongya Ge, Committee Member Date
Associate Professor, Electrical and Computer Engineering Department, NJIT

_____

Dr. Osvaldo Simeone, Committee Member Date
Assistant Professor, Electrical and Computer Engineering Department, NJIT

_____

Dr. Aijun Song, Committee Member Date
Assistant Professor, College of Earth, Ocean, and Environment, University of Delaware

BIOGRAPHICAL SKETCH

Author: Huaihai Guo

Degree: Doctor of Philosophy

Date: January 2011

Undergraduate and Graduate Education:

- Doctor of Philosophy in Electrical Engineering
  New Jersey Institute of Technology, Newark, New Jersey, 2010
- Master of Science in Electrical Engineering
  Cleveland State University, Cleveland, OH, 2005
- Bachelor of Science in Electrical Engineering
  Beijing University of Aeronautics and Astronautics, Beijing, P.R. China, 1999

Major: Electrical Engineering

Presentations and Publications:

H. Guo, A. Abdi, A. Song and M. Badiey, "Delay and Doppler spreads in underwater acoustic particle velocity channels," accepted by *Journal of the Acoustical Society of America*.

H. Guo, A. Abdi, A. Song and M. Badiey, "Characterization of delay and Doppler spreads of underwater particle velocity channels using zero crossing rates," in *Proc. Conf. Inform. Sci. Syst.*, Princeton University, Princeton, NJ, 2010.

A. Abdi and H. Guo, "A new compact multichannel receiver for underwater wireless communication networks," *IEEE Trans. Wireless Commun.*, vol 8, pp. 3326 - 3329, 2009.

A. Abdi and H. Guo, "Signal correlation modeling in acoustic vector sensor arrays," *IEEE Trans. Signal Processing*, vol. 57, pp. 892-903, 2009.

H. Guo, A. Abdi, A. Song and M. Badiey, "Correlations for underwater acoustic particle velocity and pressure channels", in *Proc. Conf. Inform. Sci. Syst.*, John Hopkins University, Baltimore, MD, 2009.

H. Guo, A. Abdi, "Multiuser underwater communication with space-time block codes and acoustic vector sensors," in *Proc. MTS/IEEE Oceans*, Québec City, QC, Canada, 2008.

A. Abdi, H. Guo, "A correlation model for vector sensor arrays in underwater communication systems," in *Proc. MTS/IEEE Oceans*, Québec City, QC, Canada, 2008.

A. Abdi, H. Guo and P. Sutthiwan, "A new vector sensor receiver for underwater acoustic communication," in *Proc. MTS/IEEE Oceans*, Vancouver, BC, Canada, 2007.

This dissertation is dedicated to my parents and wife.

ACKNOWLEDGEMENT

I wish to express my sincere gratitude to my advisor, Prof. Ali Abdi, for introducing me into this new underwater communication research area. Without Dr Abdi's consistent guidance and support throughout my whole Ph.D program, I would not be able to reach this point.

I also want to thank Dr. Alexander M. Haimovich, Dr. Hongya Ge and Dr. Osvaldo Simeone from Electrical and Computer Engineering Department of NJIT to be the members of committee. I appreciate their insight and suggestions during this research.

Special thanks to Dr. Aijun Song, from College of Earth, Ocean, and Environment of University of Delaware for serving as a member of committee and providing expert assistance for the underwater communication study.

I also want to thank Center for Wireless Communication and Signal Processing Research, Dr. Yeheskel Bar-Ness, Mrs. Marlene Toeroek and all my lab-mates.

I'd like to send my special thanks to Dr. Fuqin Xiong, my MS. program advisor, from Cleveland State University, not only for the teaching and advising in my master study, but also for helping during my Ph.D study.

And as a research assistant, I'd like to thank National Science Foundation for supporting our new underwater acoustic communication research.

Finally, I'd like to thank all the people who helped, guided and encouraged me in my whole life.

TABLE OF CONTENTS

TABLE OF CONTENTS
(Continued)

LIST OF TABLES

LIST OF FIGURES

LIST OF FIGURES
(Continued)

LIST OF ACRONYMS

AOA	angle of arrival
AUV	autonomous underwater vehicle
BER	bit error rate
CDMA	code division multiple access
DFT	discrete Fourier transform
IR	impulse response
ISI	inter-symbol interference
MIMO	multiple-input multiple-output
MMSE	minimum mean square error
OFDM	orthogonal frequency division multiplexing
PDF	probability density function
RF	radio frequency
RMS	root-mean-squared
SIMO	single-input multiple-output
SNR	signal-to-noise ratio
UWA	underwater acoustic
ZCR	zero crossing rate
ZF	zero-forcing

CHAPTER 1

INTRODUCTION

1.1 Introduction

1.1.1 Overview of Underwater Communication

Data communication is of interest in numerous naval and civilian applications. Examples include communication among autonomous underwater vehicles (AUVs) for collaborative operations, harbor security systems, tactical surveillance applications, oceanographic data retrieval from underwater sensors over geographically large areas, offshore oil and gas explorations, … The harsh multipath, with delay spreads up to hundreds of symbols for high data rates, and temporal variations of the underwater acoustic channels, with Doppler spreads up to several ten Hz, are major issues in underwater acoustic communication [1]. After the first generation of analog modems, second generation digital modems in 80's used non-coherent techniques such as frequency shift keying and differentially coherent schemes like DPSK [1]. Due to the need for higher spectral efficiencies, coherent systems with phase shift keying and quadrature amplitude modulation were developed in 90's [2] [3]. Spatial diversity with arrays of hydrophones and different types of equalization, beamforming, coding, channel estimation and tracking are also used for underwater communication [1]. Underwater multiple-input multiple-output (MIMO) systems using spatially separated pressure sensors are also recently investigated [4]-[7].

1.1.2 Overview of Vector Sensor

The development of vector sensors dates back to 30's [8]. Since late 60's, the Navy has been using vector sensors in systems such as Directional Frequency Analysis and Recording (DIFAR) and Directional Command Activated Sonobuoy System (DICASS) [9] [10]. In the past few decades, a large volume of research has been conducted on

theory, performance evaluation, and design of vector sensors, mainly used in SONAR systems (see, for example, [11] and [12]). Examples include accurate azimuth and elevation estimation of a source [13] [14], avoiding the left-right ambiguity of linear towed arrays of scalar sensors, significant acoustic noise reduction due to the highly directive beam pattern [19] [20], etc. All these advantages are due to the directional information that vector sensors provide, by measuring the three orthogonal components of velocity, for example, as well as the pressure component, at a single point.

In general, there are two types of vector sensors: inertial and gradient [21]. Inertial sensors truly measure the velocity or acceleration by responding to the acoustic particle motion, whereas gradient sensors employ a finite-difference approximation to estimate the gradients of the acoustic field such as velocity and acceleration. Each sensor type has its own advantages and disadvantages. Inertial sensors offer a broad dynamic range, but proper supporting and packaging of the sensor without affecting its response to the motion is an issue. Furthermore, since they do not distinguish between acoustic waves and non-acoustic motion sources such as support structure vibrations, they must be properly shielded from such disturbances. Making accurate yet small inertial sensors at high frequencies could be challenging as well. On the other hand, gradient sensors can be manufactured in smaller sizes and thus are more suitable for high frequencies. However, the finite-difference approximation which is the basis of operation of these sensors limits their operating dynamic range. Moreover, the individual elements of a gradient sensor are required to have low self-noise and should be well calibrated and matched.

Recent progress in material science and manufacturing technologies for vector sensors is offering small size, low noise, and robust sensors (see [44] as an example). All these manufacturing advances certainly encourage the widespread use of vector sensors in many more underwater naval and civilian applications, including the vector sensor communication system proposed and developed in this dissertation. However, the proposed ideas, to take advantage of the vector components of the field at the receiver,

are not restricted to a particular sensor type. Of course the noise properties, input dynamic range, bandwidth, sensitivity, and other characteristics of a vector sensor affect the reception performance, but the principles, models, and concepts developed in this dissertation remain nearly the same. Depending on the application, system cost, required precision, etc., one can choose the proper sensor type and technology.

1.2 Motivation

A vector sensor is capable of measuring important non-scalar components of the acoustic field such as the particle velocity, which cannot be obtained by a single scalar pressure sensor. In the past few decades, extensive research has been conducted on the theory and design of vector sensors (see, for example, [11]-[13]). They have been used for SONAR and target localization [13]-[20], to accurately estimate the azimuth and elevation of a source [13] [14], to avoid the left-right ambiguity in linear towed arrays of scalar sensors, and to reduce acoustic noise due to their directive beam pattern [20].

On the other hand, underwater acoustic communication systems have been relying on scalar sensors only, which measure the pressure of the acoustic field. By taking advantage of the vector components of the acoustic field, such as the particle velocity, sensed by a vector sensor at the receiver, the vector sensor can be used for detecting the transmitted data. The small size of such receivers is due to the fact that a vector sensor measures the scalar and vector components of the acoustic field in a single point in space, therefore can serve as a compact multichannel receiver. This is different from the existing multichannel underwater receivers [2]-[22], which are composed of spatially separated pressure-only sensors, which may result in large-size arrays.

The exiting trend in multiuser underwater communication is to use a spread spectrum technique, which allows multiple users to communicate via spreading codes and bandwidth expansion. Examples include code division multiple access (CDMA) systems [23]. Bandwidth expansion is not a problem in radio frequency (RF) channels, due to the

very large bandwidths of such channels. However, spectrum spreading in seriously bandlimited underwater channels reduces the data rate of each user.

Recently, a multiple access scheme is developed which does not rely on bandwidth expansion [24] [25]. Therefore, it can accommodate multiple high data rates users, without reducing their transmission rates. The key idea is to use space time block codes [24] [25], to communicate over acoustic particle velocity channels using vector sensors [30] [31]. The algebraic structure of space-time block codes allows for multiple access without bandwidth expansion, whereas vector sensor receivers serve as compact multichannel equalizers. The smaller delay spread of some particle velocity channels [31] helps reduce the equalizer complexity as well. Reducing the size and complexity of the receiver is particularly important in systems which have serious size limitations.

An important underwater channel is the shallow water acoustic channel. It is basically a waveguide, bounded from bottom and the top. The sea floor is a rough surface which introduces scattering, reflection loss, and attenuation by sediments, whereas the sea surface is a rough surface that generates scattering and reflection loss and attenuation by turbidity and bubbles [32]. When compared with deep waters, shallow waters are more complex, due to the many interactions of acoustic waves with boundaries, which result in a significant amount of multipath propagation.

In underwater multipath channels, a vector sensor receives the signal through multiple paths. This introduces different levels of correlation in an array of vector sensors. Depending on the angle of arrivals (AOAs) and other channel characteristics, different types of correlation appear in a vector sensor array. These correlations affect the performance of a vector sensor communication system. Characterizations of these correlations in terms of the physical parameters of the channel are needed for proper system design, to achieve the required performance in the presence of correlations [33]-[35]. Furthermore, closed-form parametric expressions for the signal correlations serve as

useful tools to estimate some important physical parameters of the channel such as angle spread, mean angle of arrival, etc. [36]-[38].

In multipath channels such as shallow waters, a vector sensor receives the signal through several paths and each path has a different delay (travel time). Motion of the transmitter or receiver in a multipath channel introduces different Doppler shifts as well. Knowledge of the delay and Doppler spreads in acoustic particle velocity channel is important for efficient design of underwater vector sensor communication system. Characterization of delay and Doppler spreads in terms of the physical parameters of propagation environment is needed for system performance predication as well. It is well known that delay and Doppler spreads are proportional to the zero crossing rates (ZCRs) of the channel in frequency [39][40] and time [41][42] domains, respectively. By estimating the corresponding ZCRs, one can evaluate the delay and Doppler spreads in particle velocity channels.

Overall, as a new application of vector sensor in underwater communication area, in this dissertation, the new vector sensor communication system will be built up and the performances will be evaluated in several aspects. Also characterizations of pressure and particle velocity channels will be modeled and investigated in this dissertation.

1.3 Organization

This dissertation discusses in detail about the vector sensor underwater acoustic (UWA) communication system and the corresponding channel characteristics. It is organized as following:

Chapter 1 introduces the importance of and the issues leading to this study, illustrates application background and research objectives and outlines the organizations.

In Chapter 2, first, the new compact underwater acoustic communication system via vector sensor receiver for single user is established. Basic system equations are derived, including channel detection and equalization. Signal and noise power

characteristics in such sensors are also investigated. Via extensive simulations under different propagation scenarios, the performance of a vector sensor receiver is determined while some channel characteristics are given for different scenarios. Based on the single user system, by taking the advantage of space time block coding, the multiuser communication system with one vector sensor receiver but multiple pressure transmitters is derived also in this chapter.

The vector sensor collects the single via multipath environment, therefore different correlations of vector sensor receivers are analyzed and simulated in Chapter 3. First the statistical frame work for correlation analysis is built up and complete exact expressions are given to obtain the actual correlations. Then the closed non-integral forms for correlations are derived upon the small angle of arrival (AOA) spread. Finally the comparison example of this model with the experiment correlation is given to verify this mathematical model.

Based on the frequency and temporal correlations given in Chapter 3, a zero crossing rate (ZCR) framework is developed to model the channel delay and Doppler spreads in Chapter 4. Similar to Chapter 3, first the exact frequency and time domain ZCRs are obtained, then closed-form integral-free expressions are derived. The delay spreads and Doppler spreads are presented and discussed as the functions of mean of AOA and AOA spread.

Finally, the conclusion and remarks are given in Chapter 5. The future research and the possible study directions are provided also.

CHAPTER 2

UNDERWATER ACOUSTIC COMMUNICATION VIA VECTOR SENSOR RECEIVER

2.1 Single Vector Sensor Communication System

Our research starts with a single user underwater acoustic communication system via a vector sensor receiver. Since the vector sensor receiver measures not only the pressure of the acoustic wave but also the particle velocities, one vector sensor receiver can provide multiple signal outputs which can be considered as a multiple antenna receiver in the RF communication.

2.1.1 System Equations for Vector Sensor Receiver

In this section we derive basic system equations for data detection via a vector sensor. To demonstrate the basic concepts of how both the vector and scalar components of the acoustic field can be utilized for data reception, we consider a simple system in a two-dimensional (2D) depth-range underwater channel. As shown in Figure 2.1, there is one transmit pressure sensor, shown by a black dot, whereas for reception we use a vector sensor, shown by a black square, which measures the pressure and the y and z components of the particle velocity. This is basically a 1×3 single-input multiple-output (SIMO) system. With more pressure transmitters, one can have a multiple-input multiple-output (MIMO) system, which will be shown in Section 2.2.

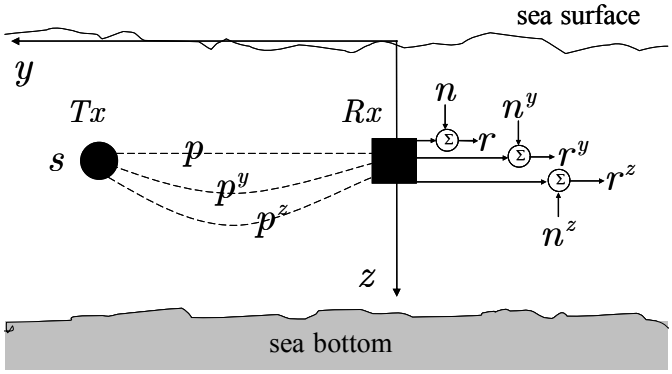

Figure 2.1 A 1×3 vector sensor communication system, with one pressure transmitter and one vector sensor receiver.

2.1.1.1 *Pressure and velocity channels and noises*

There are three channels in Figure 2.1: the pressure channel p, represented by a straight dashed line, and two *pressure-equivalent* velocity channels p^z and p^y, shown by curved dashed lines. To define p^z and p^y, we need to define the two velocity channels v^z and v^y, the vertical and horizontal components of the particle velocity, respectively. According to the linearized momentum equation [19], the z and y component of the velocity at the frequency f_0 are given by

$$v^z = -(j\rho_0\omega_0)^{-1}\partial p/\partial z,\ \ v^y = -(j\rho_0\omega_0)^{-1}\partial p/\partial y\,. \tag{2.1}$$

In the above equations, ρ_0 is the density of the fluid, $j^2 = -1$ and $\omega_0 = 2\pi f_0$. Eq. (2.1) simply states that the velocity in a certain direction is proportional to the spatial pressure gradient in that direction [19]. To simplify the notation, similar to [19], the velocity channels in (2.1) are multiplied by $-\rho_0 c$, the negative of the acoustic impedance of the fluid, where c is the speed of sound. This gives the associated pressure-equivalent velocity channels as $p^z = -\rho_0 c\, v^z$ and $p^y = -\rho_0 c\, v^y$. With λ as the wavelength and $k = 2\pi/\lambda = \omega_0/c$ as the wavenumber, we finally obtain

$$p^z = (jk)^{-1}\partial p/\partial z,\ \ p^y = (jk)^{-1}\partial p/\partial y\,. \tag{2.2}$$

The additive ambient noise pressure at the receiver is shown by n in Figure 2.1. At the same location, the z and y components of the ambient noise velocity, sensed by the vector sensor are $\eta^z = -(j\rho_0\omega_0)^{-1}\partial n/\partial z$ and $\eta^y = -(j\rho_0\omega_0)^{-1}\partial n/\partial y$, respectively, derived in the same manner as (2.1). So, the vertical and horizontal pressure-equivalent ambient noise velocities are $n^z = -\rho_0 c\ \eta^z = (jk)^{-1}\partial n/\partial z$ and $n^y = -\rho_0 c\ \eta^y = (jk)^{-1}\partial n/\partial y$, respectively, which resemble (2.2).

2.1.1.2 *Input-Output system equations*

According to Figure 2.1, the received pressure signal at *Rx* in response to the signal s transmitted from *Tx* can be written as $r = p \oplus s + n$, where $\oplus$ stands for convolution in

time. We also define the z and y components of the pressure-equivalent received velocity signals as $r^z = (jk)^{-1}\partial r/\partial z$ and $r^y = (jk)^{-1}\partial r/\partial y$, respectively. Based on (2.2) and by taking the spatial gradient of r with respect to z and y we easily obtain the key system equations

$$r = p \oplus s + n,\ r^y = p^y \oplus s + n^y,\ r^z = p^z \oplus s + n^z. \tag{2.3}$$

It is noteworthy that the three output signals r, r^y and r^z are measured at a single point in space.

2.1.1.3 *Pressure and velocity noise correlations*

We define the spatial pressure noise correlation between the two locations $(y+\ell_y, z+\ell_z)$ and (y,z) as $q_n(\ell_y,\ell_z) = E[n(y+\ell_y, z+\ell_z)n^*(y,z)]$, where * is the complex conjugate and ℓ_y and ℓ_z are real numbers. Using the correlation properties of a differentiator in p. 326 of [45], at the location (y,z) one can show $E[n\{n^y\}^*] = (jk)^{-1}\partial q_n/\partial \ell_y$, $E[n\{n^z\}^*] = (jk)^{-1}\partial q_n/\partial \ell_z$ and $E[n^z\{n^y\}^*] = -k^{-2}\partial^2 q_n/\partial \ell_z \partial \ell_y$, all calculated for $(\ell_y,\ell_z) = (0,0)$. For an isotropic noise field in the y-z plane we have $q_n(\ell_y,\ell_z) = J_0(k(\ell_y^2+\ell_z^2)^{1/2})$ [46], with $J_m(.)$ as the m-order Bessel function of the first kind. Using the properties of the Bessel functions and their derivatives [47], it is easy to verify that $E[n\{n^y\}^*] = E[n\{n^z\}^*] = E[n^z\{n^y\}^*] = 0$, i.e., all the noise terms in (2.3) are uncorrelated.

The above noise correlations may be derived using the general formulas of [48]. However, we have derived them from the first principles, to make it transparent to the readers under what conditions the noise terms in (2.3) are uncorrelated.

2.1.1.4 *Pressure and velocity average powers*

(a) *Noise Powers:* Using the statistical properties of a differentiator in p. 326 of [45], the powers of the y and z components of the pressure-equivalent noise velocity at (y,z) can be obtained as $\Omega_n^y = E[|n^y|^2] = -k^{-2}\partial^2 q_n/\partial \ell_y^2$ and $\Omega_n^z = E[|n^z|^2] = -k^{-2}\partial^2 q_n/\partial \ell_z^2$, respectively, both calculated at $(\ell_y,\ell_z) = (0,0)$. Based on the q_n of the 2D isotropic

noise model described previously, one can show $\Omega_n^y = \Omega_n^z = 1/2$. Note that the noise pressure power in this model is $\Omega_n = E[|n|^2] = q_n(0,0) = 1$. This means $\Omega_n = \Omega_n^y + \Omega_n^z$, consistent with [48].

(b) *Channel Powers:* The ambient noise is a superposition of several components coming from different angle of arrivals (AOAs) [46]. In multipath environments such as shallow waters, the channel is also a superposition of multiple subchannels. Based on this analogy between *n* and *p*, as well as their spatial gradients, one can obtain $\Omega_p = \Omega_p^y + \Omega_p^z$, where $\Omega_p = E[|p|^2]$, $\Omega_p^y = E[|p^y|^2]$ and $\Omega_p^z = E[|p^z|^2]$. The rigorous proof is not provided due to space limitations. In the 2D isotropic noise model the distribution of AOA is uniform over $[0, 2\pi)$ [46], which yields $\Omega_n^y = \Omega_n^z = \Omega_n / 2$. However, this is not necessarily the case in multipath channels such as shallow waters, which means Ω_p^y and Ω_p^z could be different.

2.1.1.5 *Signal-to-Noise ratios*

To define the average signal-to-noise ratio (SNR) per channel in BER plots of Section 2.1.4, let $\mathbf{p} = [p(0) \ldots p(M-1)]^T$, $\mathbf{p}^y = [p^y(0) \ldots p^y(M-1)]^T$ and $\mathbf{p}^z = [p^z(0) \ldots p^z(M-1)]^T$ be the taps of the pressure, *y*- and *z*-velocity IRs, respectively. Then the pressure, *y*- and *z*-velocity SNRs are $\zeta_p = \Omega_p / \Omega_n$, $\zeta_p^y = \Omega_p^y / \Omega_n^y$ and $\zeta_p^z = \Omega_p^z / \Omega_n^z$, respectively, such that $\Omega_p = \mathbf{p}^\dagger \mathbf{p}$, $\Omega_p^y = (\mathbf{p}^y)^\dagger \mathbf{p}^y$ and $\Omega_p^z = (\mathbf{p}^z)^\dagger \mathbf{p}^z$. By definition, the average SNR per channel for the vector sensor receiver is $\overline{\zeta} = (\zeta_p + \zeta_p^y + \zeta_p^z)/3$. Also $\mathbf{p}$ is normalized such that $\Omega_p = 1$. Based on Subsection 2.1.1.4, this implies that $\Omega_p^y + \Omega_p^z = 1$ in our simulations. Since $\Omega_n^y = \Omega_n^z = \Omega_n / 2$ in a 2D isotropic noise model, we finally obtain $\overline{\zeta} = 1/\Omega_n$, which is the same as the SNR of a unit-power pressure channel ζ_p.

2.1.2 Vector Sensor as A Multichannel Equalizer

In this section we use the basic zero forcing equalizer. Of course there are different types of equalizers [49] [50] and we are not suggesting the zero forcing algorithm as the best

possible equalization method. However, since here our emphasis is not on equalizer design, we just use a simple equalizer to verify the concept. The idea is just to demonstrate the feasibility of multichannel inter-symbol interference (ISI) removal using a compact vector sensor. Here the system equation is

$$\mathbf{R} = \mathbf{HS} + \mathbf{N}, \text{ where } \mathbf{R} = \begin{bmatrix} \mathbf{R}_1 \\ \mathbf{R}_2 \\ \mathbf{R}_3 \end{bmatrix}, \mathbf{H} = \begin{bmatrix} \mathbf{H}_1 \\ \mathbf{H}_2 \\ \mathbf{H}_3 \end{bmatrix}, \text{ and } \mathbf{N} = \begin{bmatrix} \mathbf{N}_1 \\ \mathbf{N}_2 \\ \mathbf{N}_3 \end{bmatrix}. \tag{2.4}$$

In (2.4) $\mathbf{S} = [s_0 \ldots s_{K-1}]^T$ includes K transmitted symbols and ^{T} is the transpose. With M as the number of channel taps, the same for all l, $l = 1,2,3$, $\mathbf{R}_l = [r_l(0) \ldots r_l(K+M-2)]^T$ and $\mathbf{N}_l = [n_l(0) \ldots n_l(K+M-2)]^T$ are the l-th $(K+M-1)\times 1$ received signal and noise vectors, respectively. Also the l-th $(K+M-1)\times K$ banded channel matrix is given by

$$\mathbf{H}_l = \begin{bmatrix} h_l(0) & & \\ \vdots & \ddots & h_l(0) \\ h_l(M-1) & \ddots & \vdots \\ & & h_l(M-1) \end{bmatrix}. \tag{2.5}$$

Note that for a vector sensor receiver, the channel indices 1, 2 and 3 in (2.4) represent the pressure, pressure-equivalent horizontal velocity and pressure-equivalent vertical velocity, respectively. So, based on (2.3), for an arbitrary discrete time index t we have $r_1(t) = r(t)$, $r_2(t) = r^y(t)$, $r_3(t) = r^z(t)$, $h_1(t) = p(t)$, $h_2(t) = p^y(t)$, $h_3(t) = p^z(t)$, $n_1(t) = n(t)$, $n_2(t) = n^y(t)$ and $n_3(t) = n^z(t)$. Furthermore, according to (2.5), the channel convolution matrices $\mathbf{H}_1$, $\mathbf{H}_2$, and $\mathbf{H}_3$ in (2.4) for a vector sensor receiver are given by

$$\mathbf{H}_1 = \begin{bmatrix} p(0) & & \\ \vdots & & \\ p(M-1) & \ddots & p(0) \\ & & \vdots \\ & & p(M-1) \end{bmatrix}, \mathbf{H}_2 = \begin{bmatrix} p^y(0) & & \\ \vdots & & \\ p^y(M-1) & \ddots & p^y(0) \\ & & \vdots \\ & & p^y(M-1) \end{bmatrix},$$

$$\mathbf{H}_3 = \begin{bmatrix} p^z(0) & & \\ \vdots & & \\ p^z(M-1) & \ddots & p^z(0) \\ & & \vdots \\ & & p^z(M-1) \end{bmatrix}.$$

Assuming perfect channel knowledge at the receiver, the zero forcing equalizer is given by

$$\hat{\mathbf{S}} = (\mathbf{H}^{\dagger}\boldsymbol{\Sigma}^{-1}\mathbf{H})^{-1}\,\mathbf{H}^{\dagger}\boldsymbol{\Sigma}^{-1}\mathbf{R}\,. \tag{2.6}$$

In this equation $\hat{\mathbf{S}}$ is the minimum variance unbiased estimate of $\mathbf{S}$ [52], † is the transpose conjugate and $\boldsymbol{\Sigma} = E[\mathbf{N}\mathbf{N}^{\dagger}]$ is the covariance matrix of the noise vector $\mathbf{N}$ in (2.4). The simulations of Subsection 2.1.4.4 show the performance of (2.6).

Since it is difficult to obtain perfect channel estimates at the receiver, in this section we also study the impact of imperfect channel estimate on the vector sensor equalizer performance. We model the effect of channel estimation error using an additive Gaussian perturbation term

$$\begin{aligned} \hat{\mathbf{p}} &= \sqrt{\zeta_p/(1+\zeta_p)}\,\mathbf{p} + \sqrt{1/(1+\zeta_p)}\,\mathbf{e}, \\ \hat{\mathbf{p}}^y &= \sqrt{\zeta_p^y/(1+\zeta_p^y)}\,\mathbf{p}^y + \sqrt{1/(1+\zeta_p^y)}\,\mathbf{e}^y, \\ \hat{\mathbf{p}}^z &= \sqrt{\zeta_p^z/(1+\zeta_p^z)}\,\mathbf{p}^z + \sqrt{1/(1+\zeta_p^z)}\,\mathbf{e}^z, \end{aligned} \tag{2.7}$$

where $\hat{\mathbf{p}}$, $\hat{\mathbf{p}}^y$, and $\hat{\mathbf{p}}^z$ are imperfect estimates of $\mathbf{p}$, $\mathbf{p}^y$, and $\mathbf{p}^z$, respectively. Moreover, $\mathbf{e}$, $\mathbf{e}^y$, and $\mathbf{e}^z$ are $M \times 1$ complex Gaussian random vectors that represent channel estimation errors. Note that for each equation in (2.7), when the corresponding SNR is small, i.e., ζ_p, ζ_p^y or ζ_p^z, the estimation error term becomes dominant, as expected. On the other hand, when SNRs are large, we reasonably get $\hat{\mathbf{p}} \approx \mathbf{p}$, $\hat{\mathbf{p}}^y \approx \mathbf{p}^y$, and $\hat{\mathbf{p}}^z \approx \mathbf{p}^z$.

The vectors $\mathbf{e}$, $\mathbf{e}^y$, and $\mathbf{e}^z$ are independent, and elements of each vector are independent and identically distributed zero-mean complex Gaussian random variables

with standard deviations $\sigma_p = \sqrt{\Omega_p / M}$, $\sigma_p^y = \sqrt{\Omega_p^y / M}$ and $\sigma_p^z = \sqrt{\Omega_p^z / M}$, respectively. Note that these choices for the standard deviations guarantee that the powers of the true channel coefficient vectors and their estimates are the same, i.e., $\hat{\Omega}_p = E[\hat{\mathbf{p}}^\dagger \hat{\mathbf{p}}] = \Omega_p$, $\hat{\Omega}_p^y = E[(\hat{\mathbf{p}}^y)^\dagger \hat{\mathbf{p}}^y] = \Omega_p^y$ and $\hat{\Omega}_p^z = E[(\hat{\mathbf{p}}^z)^\dagger \hat{\mathbf{p}}^z] = \Omega_p^z$.

In the presence of channel estimation error, the zero forcing equalizer can be written as

$$\hat{\mathbf{S}}_{\text{ChEstErr}} = (\hat{\mathbf{H}}^\dagger \boldsymbol{\Sigma}^{-1} \hat{\mathbf{H}})^{-1} \hat{\mathbf{H}}^\dagger \boldsymbol{\Sigma}^{-1} \mathbf{R} , \tag{2.8}$$

where $\hat{\mathbf{S}}_{\text{ChEstErr}}$ is the estimate of $\mathbf{S}$, when $\mathbf{H}$ is not perfectly estimated, and $\hat{\mathbf{H}} = [\hat{\mathbf{H}}_1^T \; \hat{\mathbf{H}}_2^T \; \hat{\mathbf{H}}_3^T]^T$.

2.1.3 Simulation Setup and Parameters

In this section we basically simulate and compare the performance of the vector sensor equalizer in (2.6) and (2.8) with a vertical three-element pressure-only uniform linear array (ULA), as well as a single pressure sensor receiver that perform zero forcing equalization (with and without perfect channel estimate).

The ULA equations and equalizers are the same as (2.4), (2.6) and (2.8), where the three channels represent three vertically separated pressure channels. The noise vectors $\mathbf{N}_1, \mathbf{N}_2$ and $\mathbf{N}_3$ in both receivers are considered to be complex Gaussians with white temporal auto- and cross-correlations. For the isotropic noise model discussed in Subsection 2.1.1.3, the noise vectors $\mathbf{N}_1, \mathbf{N}_2$ and $\mathbf{N}_3$ are uncorrelated in the vector sensor receiver. Therefore its noise covariance matrix $\boldsymbol{\Sigma}_{\text{vector sensor}} = E[\mathbf{N}_{\text{vector sensor}} \mathbf{N}_{\text{vector sensor}}^\dagger]$ is given by

$$\boldsymbol{\Sigma}_{\text{vector sensor}} = \begin{bmatrix} \Omega_n \mathbf{I}_{K+M-1} & \mathbf{0} & \mathbf{0} \\ \mathbf{0} & (\Omega_n / 2)\mathbf{I}_{K+M-1} & \mathbf{0} \\ \mathbf{0} & \mathbf{0} & (\Omega_n / 2)\mathbf{I}_{K+M-1} \end{bmatrix}, \tag{2.9}$$

where $\mathbf{I}_m$ is an $m \times m$ identity matrix and $\mathbf{0}$ is a matrix whose elements are all zero. For the pressure-only ULA with the element spacing of L, there are some pressure correlations of $J_0(kL)$ and $J_0(2kL)$ for the separations of L and $2L$, respectively. This means that the noise covariance matrix $\mathbf{\Sigma}_{\text{pressure-only ULA}} = E[\mathbf{N}_{\text{pressure-only ULA}} \mathbf{N}^{\dagger}_{\text{pressure-only ULA}}]$ can be written as

$$\mathbf{\Sigma}_{\text{pressure-only ULA}} = \begin{bmatrix} \Omega_n \mathbf{I}_{K+M-1} & J_0(kL)\mathbf{I}_{K+M-1} & J_0(2kL)\mathbf{I}_{K+M-1} \\ J_0(kL)\mathbf{I}_{K+M-1} & \Omega_n \mathbf{I}_{K+M-1} & J_0(kL)\mathbf{I}_{K+M-1} \\ J_0(2kL)\mathbf{I}_{K+M-1} & J_0(kL)\mathbf{I}_{K+M-1} & \Omega_n \mathbf{I}_{K+M-1} \end{bmatrix}. \tag{2.10}$$

To calculate the velocity channel impulse responses (IRs) p^y and p^z in simulations using the p channel IR generated by Bellhop [51], each spatial gradient in (2.2) is approximated by a finite difference. Therefore at location (y, z) we have $\partial p(y,z)/\partial z \approx [p(y, z+0.2\lambda) - p(y,z)]/(0.2\lambda)$ and $\partial p(y,z)/\partial y \approx [p(y+0.2\lambda, z) - p(y,z)]/(0.2\lambda)$.

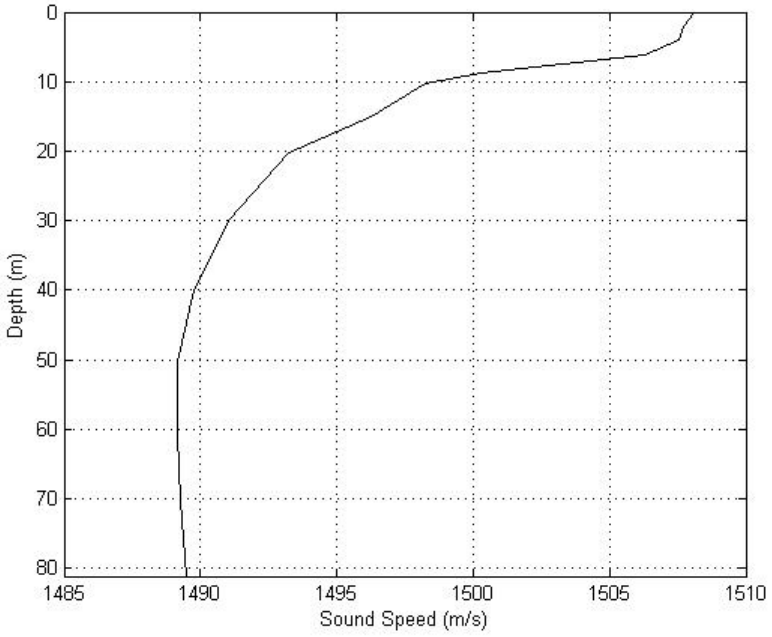

Figure 2.2 Sound speed versus the water depth.

With an **S** vector that includes $K = 200$ equal-probable ± 1 symbols, and the noise vector and channel matrix **N** and **H** generated as described above, the received vector **R** is calculated using (2.4). Then **S** is estimated using (2.6) and (2.8), and the bit error rate (BER) curves are plotted, as shown in subsection 2.1.4.4. The parameters chosen to generate channel IRs are the same as [53] and are listed in Table 2.1. Other receiver depths are considered in [54]. The sound speed profile we used was measured during the underwater communication experiments conducted on May 10, 2002, in waters off San Diego, CA [53], and is shown in Figure 2.2.

Table 2.1 Simulation and Channel Parameters

Water Depth (m)	81.158
Water Density (kg/m^3)	1024
Transmitter Depth (m)	25
Transmit Take-off Angle (degree)	-30 to 30
Number of Beams	2001
Bottom Types	Coarse silt, Very fine sand
Receiver Depth (m)	63
Receiver Range (km)	5, 10
Carrier Frequency (kHz)	12
Sampling Frequency (kHz)	48
Data Rate (kbps)	2.4
Nominal Sound Speed (m/s)	1500
Wavelength (m)	0.125

2.1.4 Simulation Results and Performance Comparison

According to Table 2.1, we have four propagation scenarios:

Scenario 1: 5 km range and coarse silt bottom;

Scenario 2: 10 km range and coarse silt bottom;

Scenario 3: 5 km range and very fine sand bottom;

Scenario 4: 10 km range and very fine sand bottom.

In the following subsections, the data and analysis of all four scenarios will be given. However, to limit the pages of the whole document, only the figures belong to scenario 1 are shown. All the figures for the other scenarios can be found in [31].

First we show channel impulse responses and frequency responses. Then we study the delay spread and the horizontal to vertical velocity power ratio versus range and depth, for different bottom types. Afterwards, we present BER and eigenvalue curves, which demonstrate the performance of the proposed vector sensor receiver, as well as a pressure-only array receiver and a single pressure sensor receiver. At the end the impact of channel estimation error is discussed.

2.1.4.1 *Impulse response and frequency response*

The amplitudes of the complex impulse responses for scenario 1 are shown in Figure 2.3, which includes the impulse responses of the pressure, horizontal velocity and vertical velocity channels, with powers Ω_p , Ω_p^y and Ω_p^z defined in Subsection 2.1.1.5, respectively. The number of channel taps and the powers of horizontal and vertical velocity channels in the simulations are given as:

Scenario 1: $M = 147,\ \Omega_p^y = 0.42,\ \Omega_p^z = 0.58$;

Scenario 2: $M = 197,\ \Omega_p^y = 0,\ \Omega_p^z = 1$;

Scenario 3: $M = 460,\ \Omega_p^y = 0.39,\ \Omega_p^z = 0.61$;

Scenario 4: $M = 846,\ \Omega_p^y = 0.03,\ \Omega_p^z = 0.97$.

As mentioned in Section 2.1.3, the pressure channel in simulations is normalized to have unit power, i.e., $\Omega_p = 1$, and also $\Omega_p^y + \Omega_p^z = 1$. The amplitudes of the Fourier transforms of the impulse responses of Figure 2.3 are shown in Figure 2.4.

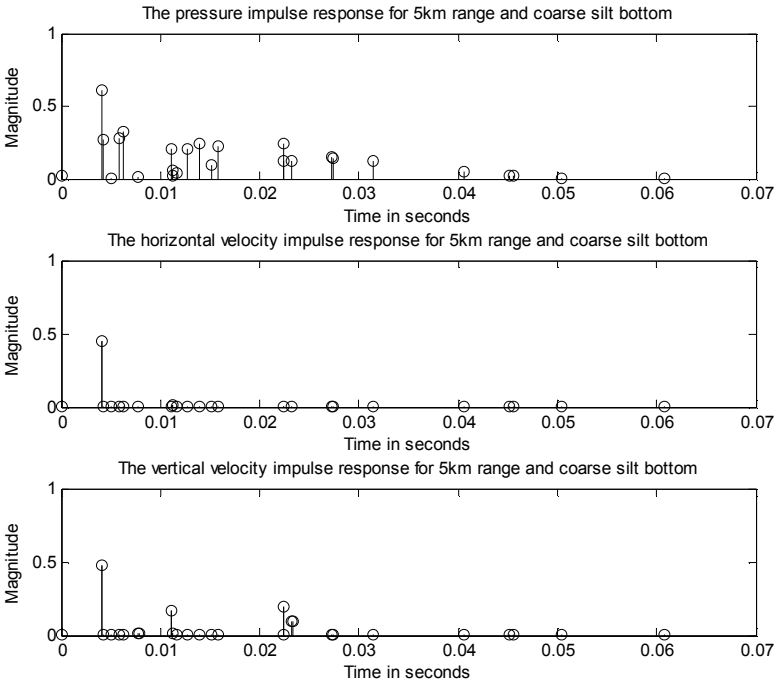

Figure 2.3 The amplitude of the impulse responses in Scenario 1.

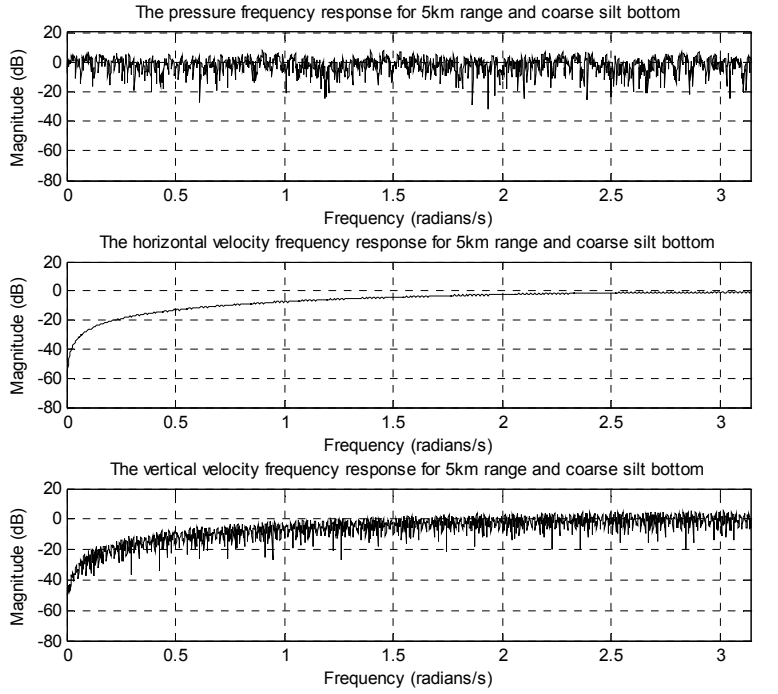

Figure 2.4 The amplitude of the frequency responses in Scenario 1.

2.1.4.2 *Delay spread*

Here we look at the root-mean-squared (RMS) delay spread τ_{rms} [55] as a measure of the frequency selectivity of a channel. Typically a large delay spread indicates a highly frequency selective channel. The values of τ_{rms} are given in Table 2.2.

Table 2.2 RMS Delay Spreads (MSEC.) in Four Propagation Scenarios

	Pressure channel	Horizontal velocity channel	Vertical velocity channel
Scenario 1	7.7	0.26	6.8
Scenario 2	14.8	12.9	11.4
Scenario 3	48.1	0.28	44.1
Scenario 4	90.3	4.3	68.3

In Figure 2.5, τ_{rms} of p, p^y and p^z impulse responses are plotted versus range, at 20, 40, and 60 m depths, for the coarse silt bottom. Then by averaging over these three depths, an average curve versus range is obtained for each of the p, p^y and p^z channels, as shown in Figure 2.6 for the coarse silt bottom.

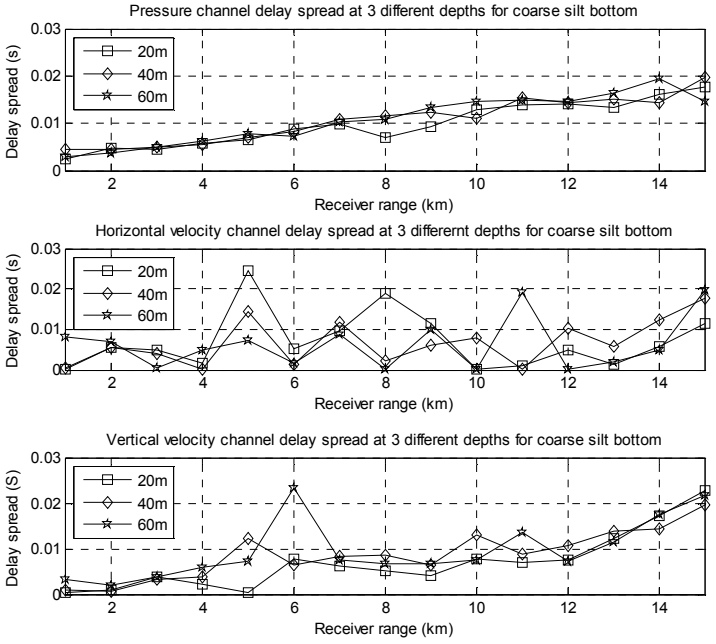

Figure 2.5 Delay spread versus range for the coarse silt bottom at different depths. Top: pressure channel, Middle: y-velocity channel, Bottom: z-velocity channel.

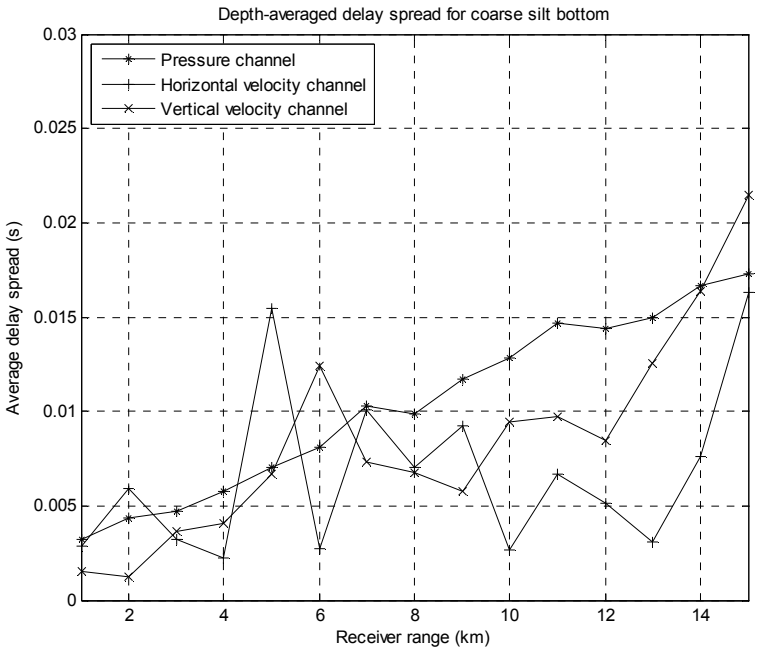

Figure 2.6 Depth-averaged delay spread versus range for the coarse silt bottom.

According to Figure 2.5, delay spread of the p channel do not noticeably change with depth, compared to the delay spreads of p^y and p^z channels. For the coarse silt bottom in Figure 2.6, one can see more variations among the depth-averaged delay spreads of all the channels.

2.1.4.3 *Horizontal to vertical velocity power ratio*

The ratio Ω_p^y / Ω_p^z is plotted versus the receiver range in Figure 2.7 for coarse bottoms. First Ω_p^y / Ω_p^z is presented at three different depths which are 20, 40 and 60 m. Then by averaging over these three depths, a single average curve versus range is obtained for each bottom. For the coarse silt bottom Ω_p^y / Ω_p^z can take large values at certain depths and ranges, as shown in Figure 2.7. For the very fine sand bottom we have $\Omega_p^y / \Omega_p^z < 1$, for ranges up to 14 km, which is shown in [30] and [31].

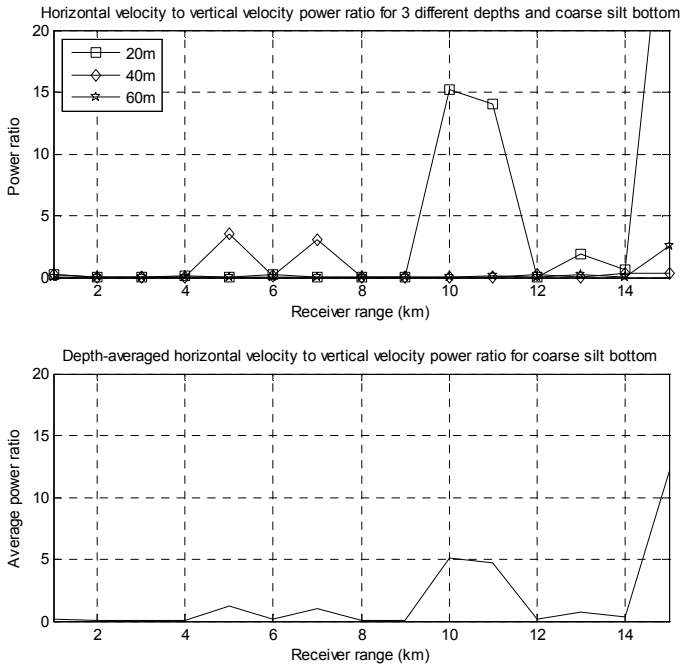

Figure 2.7 Horizontal to vertical velocity power ratio versus range for the coarse silt bottom. Top: different depths, Bottom: averaged over different depths.

2.1.4.4 *Bit error rate*

The BER curves versus the average SNR per channel $\overline{\zeta}$, defined in Subsection 2.1.1.5, are shown in Figure 2.8, for Scenarios 1, which includes the BERs of a vector sensor receiver, a three-element pressure-only array receiver with element spacing λ, 5λ and 50 λ and a single pressure sensor receiver. Performance of the three-element pressure-only array depends on its element spacing L, as shown in Figure 2.8. As L increases, the noise spatial correlation decreases and also the three pressure channels become less correlated. These both result in a reduction in BER, as L increases. According to Figure 2.8, the pressure-only array receiver with $L = 50\lambda$ outperforms the vector sensor receiver. By changing the simulation scenario, for example the bottom type, the pressure-only array may outperform the vector sensor receiver with an element spacing smaller than 50λ. However, the general picture does not change, i.e., both the vector sensor and pressure-only array receivers are much better than a single pressure sensor receiver. The advantage of the vector sensor receiver is it smaller size, compared to the pressure-only array.

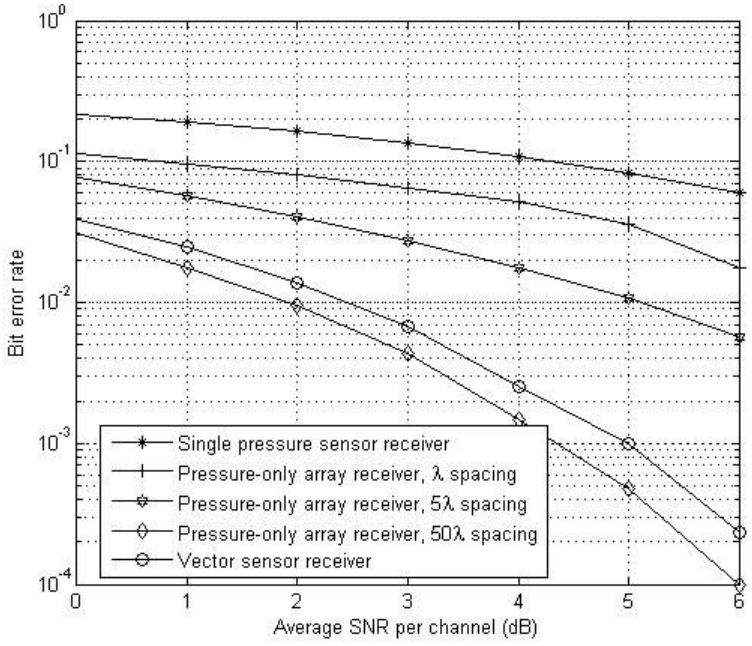

Figure 2.8 Performance comparison of a vector sensor receiver, a single pressure sensor receiver, and a uniform linear array receiver with three pressure sensors and different element spacings $L = \lambda$, 5λ and 50λ in Scenario 1.

To confirm the accuracy of the BER results shown in Figure 2.8, one can look at the level of error in symbol estimates, which are obtained using the equalizer in (2.6). The covariance matrix of the symbol estimation error vector $\hat{\mathbf{S}} - \mathbf{S}$ can be shown to be [52]

$$E[(\hat{\mathbf{S}} - \mathbf{S})(\hat{\mathbf{S}} - \mathbf{S})^{\dagger}] = (\mathbf{H}^{\dagger}\boldsymbol{\Sigma}^{-1}\mathbf{H})^{-1}, \tag{2.11}$$

where $\mathbf{H}$ and $\boldsymbol{\Sigma}$ are the channel matrix and the noise covariance matrix, respectively. In Figure 2.9 the square root of the sorted diagonal elements of $(\mathbf{H}^{\dagger}\boldsymbol{\Sigma}^{-1}\mathbf{H})^{-1}$ in (2.11) are plotted, which are the standard deviations of the symbol estimation errors. As expected, the estimation error standard deviations of the pressure-only array decrease as L increases. Furthermore, the estimation error standard deviations of the vector sensor are much smaller than those of a single pressure sensor and pressure-only arrays with small element spacings. All these are consistent with the BER results of Figure 2.8.

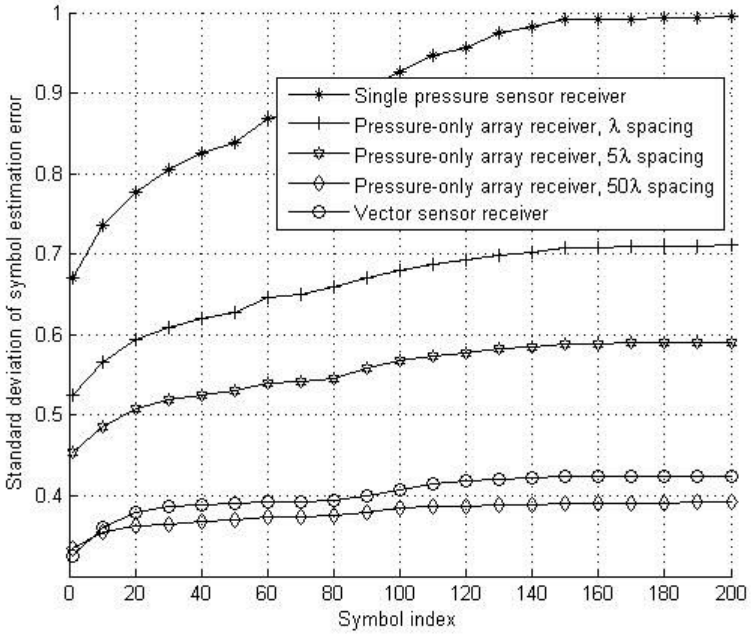

Figure 2.9 Square root of the sorted diagonal elements of the symbol estimation error covariance matrix, given in (2.11). The receivers are a vector sensor, a single pressure sensor and a uniform linear array with three pressure sensors and different element spacings $L = \lambda$, 5λ and 50λ. The average SNR per channel for each receiver is 6 dB.

As expected, the performance of the single pressure sensor receiver is much worse than the other two receivers. The performance of the vector sensor receiver is slightly worse than the pressure-only array with 50λ element spacing. According to the summary of SNRs provided in Table 2.3, the difference in performance ranges from 0.3 dB to 2.4 dB, among all the four scenarios. By changing the simulation scenario, for example the bottom type, frequency of operation, or inclusion of the flow noise and non-acoustic disturbances which are particularly important for inertial (motion) vector sensors, one may observe a worse performance for the vector sensor equalizer, compared to the pressure-only array equalizer.

One simple way of explaining the performance of these three zero forcing equalizers is to look at the condition number of $\mathbf{H}^{\dagger}\mathbf{H}$ in (2.6). By definition, the condition number of a matrix is the ratio of its largest singular value to the smallest one, and a large condition number implies that the matrix is nearly singular. This corresponds

to more noise enhancement in the zero forcing equalizer, due to the inverse of $\mathbf{H}^{\dagger}\mathbf{H}$. Based on the condition numbers provided in Table 2.3, calculated in Matlab®, one can see a better equalizer typically has a smaller condition number, as expected.

All the other BER performance for different scenarios can be found in [31].

Table 2.3 A Summary of the Required SNRs for Specific BERs

	Equalizer	Condition no.	Average. SNR per channel (dB)	
			BER = 10^{-3}	BER = 10^{-2}
Scenario 1	**Vector sensor**	**99**	**4.6**	**2.1**
	Pressure-only array	126	7	4.3
	Single pressure sensor	174	14	9.7
Scenario 2	**Vector sensor**	**16**	**5.2**	**2.7**
	Pressure-only array	292	6.7	4.2
	Single pressure sensor	297	9.2	6.8
Scenario 3	**Vector sensor**	**83**	**4.3**	**1.8**
	Pressure-only array	57	4.6	2.2
	Single pressure sensor	58	9.8	7.4
Scenario 4	**Vector sensor**	**12**	**2.5**	**0**
	Pressure-only array	23	4	1.4
	Single pressure sensor	25	8.6	6

2.1.4.5 *Effect of imperfect channel estimates*

In Figure 2.10 we present the BERs for Scenario 1, with and without perfect channel estimates. As expected, equalization without exact knowledge of the channel matrix **H** results in a loss in SNR for all types of receivers. For example, at BER = 10^{-2}, the SNR loss for the vector sensor receiver is 3 dB.

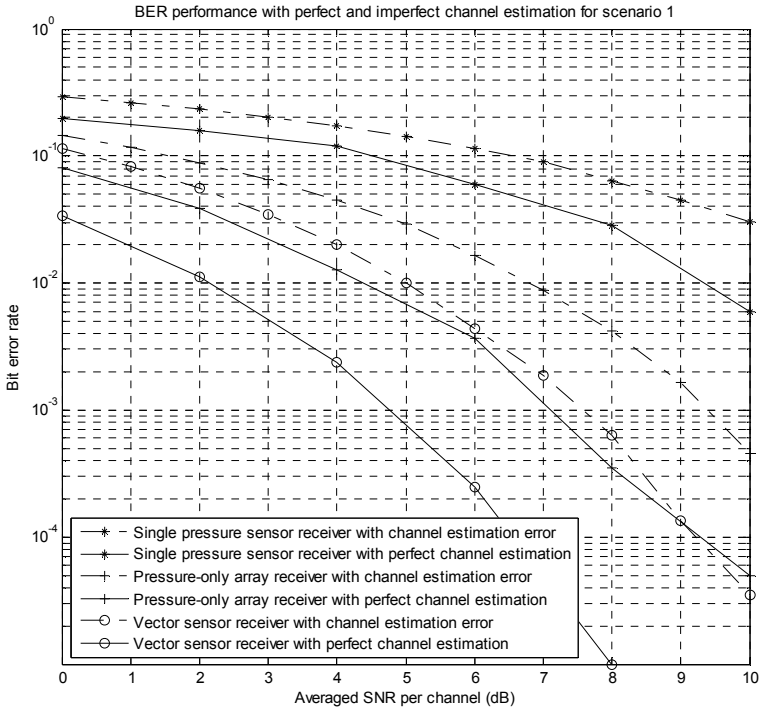

Figure 2.10 The impact of imperfect channel estimate on the performance of vector sensor and pressure-only equalizers in Scenario 1.

2.2 The Multiuser Communication via Vector Sensor Receiver

In Section 2.1, the vector sensor underwater communication system is introduced as a new multiple channels acoustic receiver. Therefore, by taking the advantage of multiple input multiple output (MIMO) scheme, multiuser underwater communication system without bandwidth expansion can be realized.

2.2.1 The Multiuser System

First we explain the system through a three user's example. Extension to more users is straightforward. Consider the scenario shown in Figure 2.11, where three users are transmitting data to one receiver. Each user has two pressure sensors, whereas the receiver is equipped with only one vector sensor. Extension to three dimension propagation is straightforward, where the vector sensor measures the x component of

particle velocity channel as well. To make the figure easy to read, only the channels of the first transmitter of user 2, i.e., *Tx*21 are shown.

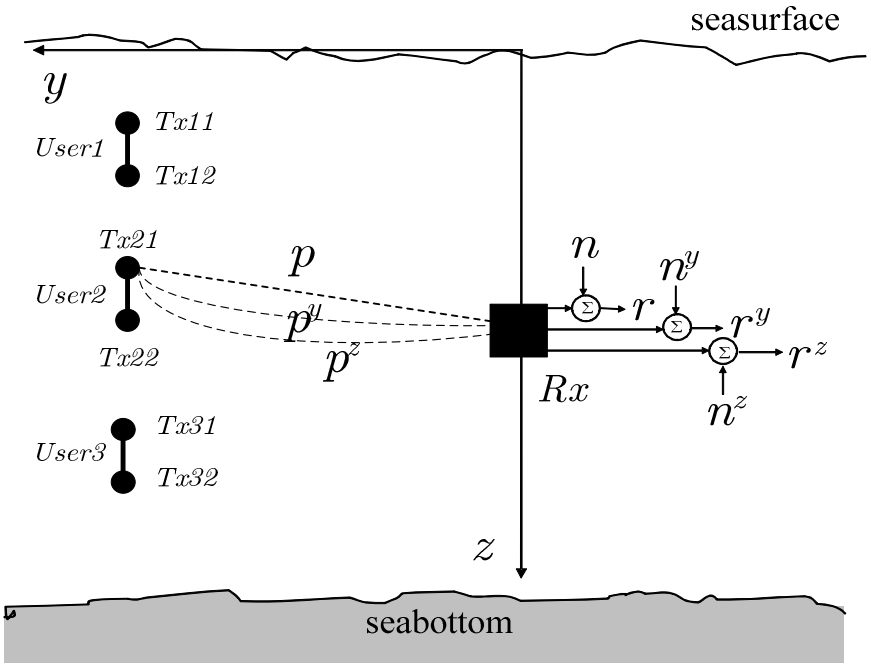

Figure 2.11 A three-user vector sensor communication system, with two pressure sensor transmitters (black dots) per user and a single vector sensor receiver (black square).

Each user transmits its own data from the two pressure sensors using Alamouti code. It can be shown that a three channel receiver can separate up to three users [24]-[26]. Therefore, the proposed three channel vector sensor receiver in Figure 2.11 can successfully recover the data of each user. Note that all the users are simultaneously sharing the same bandwidth, without spreading codes, and still can be separated at the receiver.

2.2.2 System Equations

For the users shown in Figure 2.11, Alamouti code is used [28]. Each user has two pressure transmitters. Formulas for the channel impulse response of pressure and velocity channels and vector sensor equations and communication concepts are given as (2.1)-(2.2). In this section, we provide the system equations for single and multiple users, both with Alamouti code.

2.2.2.1 *Single user system*

Consider a single user system, where the user is equipped with two pressure transmitter in a frequency-selective acoustic channel, and the receiver has K receive channels. The Alamouti encoder maps every pair of blocks $\mathbf{s}_i(u)$ and $\mathbf{s}_{i+1}(u)$ with length u into the transmission matrix $\mathbf{X}$ at time index i [27]-[28]:

$$\mathbf{X} = \begin{pmatrix} s_i(u) & -s_{i+1}^*(u) \\ s_{i+1}(u) & s_i^*(u) \end{pmatrix}, \tag{2.12}$$

where * is complex conjugation. Let $\mathbf{y}_{k,i}$ and $\mathbf{y}_{k,i+1}$ denote the blocks received by the k^{th} receive channel, which $k = 1,2 \ldots K$, in tow successive slots at instants i and i+1. This gives the following I/O relationships [27]-[28]:

$$\begin{aligned} \mathbf{y}_{k,i} &= \mathbf{h}_{1k} \oplus \mathbf{s}_i + \mathbf{h}_{2k} \oplus \mathbf{s}_{i+1} + \mathbf{n}_{k,i} \ , \\ \mathbf{y}_{k,i+1} &= -\mathbf{h}_{1k} \oplus \mathbf{s}_{i+1}^* + \mathbf{h}_{2k} \oplus \mathbf{s}_i^* + \mathbf{n}_{k,i+1} \ , \end{aligned} \tag{2.13}$$

where $\oplus$ stands for convolution in time domain and $\mathbf{h}_{1k}$ and $\mathbf{h}_{2k}$ are the channel impulse responses between transmit antenna 1 and 2 to k^{th} receive channel with the maximum channel memory v, respectively. Any channel impulse response $\mathbf{h}$ with length less than v will be zero-padded to length v. $\mathbf{n}$ is the zero mean and σ^2 variance white complex Gaussian noise vector with length u+v-1. To avoid the inter-block interference and to make all the channel matrix circulant, a cyclic prefix of length v is added to each transmitted block $\mathbf{s}$. Each channel impulse response can be written into a circulant toeplitz $(u+v\text{-}1)\times(u+v\text{-}1)$ matrix $\mathbf{H}$, [25]

$$\mathbf{H}_{jk} = \begin{pmatrix} \mathbf{h}_{jk}(0) & 0 & \ldots & \mathbf{h}_{jk}(v) & \cdots & \mathbf{h}_{jk}(1) \\ \vdots & \ddots & \ddots & \ddots & \ddots & \vdots \\ \mathbf{h}_{jk}(v-1) & \cdots & \mathbf{h}_{jk}(0) & 0 & \cdots & \mathbf{h}_{jk}(v) \\ \mathbf{h}_{jk}(v) & \mathbf{h}_{jk}(v-1) & \cdots & \mathbf{h}_{jk}(0) & 0 & \cdots \\ \vdots & \ddots & \ddots & \ddots & \ddots & \vdots \\ 0 & 0 & \mathbf{h}_{jk}(v) & \mathbf{h}_{jk}(v-1) & \cdots & \mathbf{h}_{jk}(0) \end{pmatrix},$$

where j = 1, 2 indicates the j^{th} transmitter. This changes (2.13) to

$$\begin{aligned}\mathbf{y}_{k,i} &= \mathbf{H}_{1k}\mathbf{s}_i + \mathbf{H}_{2k}\mathbf{s}_{i+1} + \mathbf{n}_{k,i} \ , \\ \mathbf{y}_{k,i+1} &= -\mathbf{H}_{1k}\mathbf{s}^*_{i+1} + \mathbf{H}_{2k}\mathbf{s}^*_i + \mathbf{n}_{k,i+1} \ .\end{aligned} \tag{2.14}$$

Now we multiply the received signal blocks $\mathbf{y}$ with the N-point orthonormal discrete Fourier transform (DFT) matrix $\mathbf{Q}$

$$\mathbf{Q}(p,q) = \frac{1}{\sqrt{N}} \exp(-jpq\frac{2\pi}{N}),$$

where $0 \le p,q \le N-1$ and $N = u+v-1$. This allows us to write the I/O relations in frequency domain and in terms of frequency-transformed variables [27]

$$\begin{aligned}\mathbf{Y}_{k,i} &= \mathbf{\Phi}_{1k}\mathbf{S}_i + \mathbf{\Phi}_{2k}\mathbf{S}_{i+1} + \mathbf{N}_{k,i} \ , \\ \mathbf{Y}_{k,i+1} &= -\mathbf{\Phi}_{1k}\mathbf{S}^*_{i+1} + \mathbf{\Phi}_{2k}\mathbf{S}^*_i + \mathbf{N}_{k,i+1} \ .\end{aligned} \tag{2.15}$$

Here $\mathbf{S}_i = \mathbf{Q}\mathbf{s}_i$, $\mathbf{N}_{k,i} = \mathbf{Q}\mathbf{n}_{k,i}$, $\mathbf{Y}_{k,i} = \mathbf{Q}\mathbf{y}_{k,i}$, $\mathbf{\Phi}_{jk}$ is a diagonal matrix given by $\mathbf{\Phi}_{\text{jk}} = \mathbf{Q}\mathbf{H}_{\text{jk}}\mathbf{Q}^{\dagger}$, and † denotes complex conjugate transpose. Rewriting (2.15) in matrix form results in:

$$\mathbf{Y}_k = \begin{pmatrix} \mathbf{Y}_{k,i} \\ \mathbf{Y}^*_{k,i+1} \end{pmatrix} = \begin{pmatrix} \mathbf{\Phi}_{1k} & \mathbf{\Phi}_{2k} \\ \mathbf{\Phi}^*_{2k} & -\mathbf{\Phi}^*_{1k} \end{pmatrix} \begin{pmatrix} \mathbf{S}_i \\ \mathbf{S}_{i+1} \end{pmatrix} + \begin{pmatrix} \mathbf{N}_{k,i} \\ \mathbf{N}^*_{k,i+1} \end{pmatrix} \ . \tag{2.16}$$

2.2.2.2 *Multiple user system*

In general, the received data at the k^{th} receiver from m^{th} user in an M user system, which $M > 1$, can be written as:

$$\mathbf{Y}_k = \mathbf{\Lambda}^m_k \mathbf{S}^m + \mathbf{N}_k \ . \tag{2.17}$$

Here m = 1, 2…M, $K \ge M$ and

$$\mathbf{\Lambda}^m_k = \begin{pmatrix} \mathbf{\Phi}^m_{1k} & \mathbf{\Phi}^m_{2k} \\ \mathbf{\Phi}^{m\,*}_{2k} & -\mathbf{\Phi}^{m\,*}_{1k} \end{pmatrix} \tag{2.18}$$

is the Alamouti-like frequency domain channel impulse response matrix from the m^{th} user to the k^{th} receive channel [25]. And

$$\mathbf{S}^m = \begin{pmatrix} \mathbf{S}_i^m \\ \mathbf{S}_{i+1}^m \end{pmatrix}, \mathbf{N}_k = \begin{pmatrix} \mathbf{N}_{k,i} \\ \mathbf{N}_{k,i+1}^* \end{pmatrix} \tag{2.19}$$

are the transmit signal vector from the m^{th} user and the noise vector at the k^{th} receiver, respectively.

$\mathbf{\Lambda}_k^m$ has an Alamouti-like structure, which means that it is an orthogonal matrix. So $\mathbf{\Lambda}_k^m \mathbf{\Lambda}_k^{m\dagger}$ becomes a diagonal matrix. This characteristic will be used throughout this section, to recover the signal from the noisy observations $\mathbf{Y}$ via a simple linear operation, as explained in Section 2.2.3.

Overall, the I/O equations in the multiuser system with M users and K receive channels are given by

$$\mathbf{Y} = \begin{pmatrix} \mathbf{Y}_1 \\ \mathbf{Y}_2 \\ \vdots \\ \mathbf{Y}_K \end{pmatrix} = \begin{pmatrix} \mathbf{\Lambda}_1^1 & \mathbf{\Lambda}_1^2 & \cdots & \mathbf{\Lambda}_1^M \\ \mathbf{\Lambda}_2^1 & \mathbf{\Lambda}_2^2 & \cdots & \mathbf{\Lambda}_2^M \\ \vdots & \vdots & \ddots & \vdots \\ \mathbf{\Lambda}_K^1 & \mathbf{\Lambda}_K^2 & \cdots & \mathbf{\Lambda}_K^M \end{pmatrix} \begin{pmatrix} \mathbf{S}^1 \\ \mathbf{S}^2 \\ \vdots \\ \mathbf{S}^M \end{pmatrix} + \begin{pmatrix} \mathbf{N}_1 \\ \mathbf{N}_2 \\ \vdots \\ \mathbf{N}_K \end{pmatrix}. \tag{2.20}$$

For the three user system shown in Figure 2.11 with the vector sensor receiver, system I/O equation can be written in frequency domain as

$$\begin{pmatrix} \mathbf{Y} \\ \mathbf{Y}_y \\ \mathbf{Y}_z \end{pmatrix} = \begin{pmatrix} \mathbf{P}^1 & \mathbf{P}^2 & \mathbf{P}^3 \\ \mathbf{P}_y^1 & \mathbf{P}_y^2 & \mathbf{P}_y^3 \\ \mathbf{P}_z^1 & \mathbf{P}_z^2 & \mathbf{P}_z^3 \end{pmatrix} \begin{pmatrix} \mathbf{S}^1 \\ \mathbf{S}^2 \\ \mathbf{S}^3 \end{pmatrix} + \begin{pmatrix} \mathbf{N} \\ \mathbf{N}_y \\ \mathbf{N}_z \end{pmatrix}, \tag{2.21}$$

where the vectors $\mathbf{Y}$, $\mathbf{Y}_y$ and $\mathbf{Y}_z$ are the received signals at the pressure, y-velocity and z-velocity channels of the vector sensor, respectively. Moreover, with m = 1, 2, 3, $\mathbf{P}^m$ is the pressure channel from the m^{th} user, $\mathbf{P}_y^m$ and $\mathbf{P}_z^m$ are the y and z component of the velocity channel from the m^{th} user, respectively.

2.2.3 Interference Cancelation and Equalization

There are two ways to recover the signal of each user: (a) Decouple the user (interference cancelation) and then apply a zero-forcing (ZF) or minimum mean square error (MMSE) equalizer to eliminate inter-symbol interference (ISI) [24][29]; (b) apply a joint MMSE decoupler and equalizer to overcome the noise enhancement at the decoupling stage of (a) and retrieve the signal at the same time. To illuminate the joint MMSE decoupler/equalizer, we first explain the approach where decoupling and equalization are separated. This shows how the Alamouti-like structure can be used to decouple multiple signals at the receiver.

2.2.3.1 *ZF decoupler and MMSE equalizer*

We begin with the ZF decoupler for a single user. Assume that the channel state information is completely known at the receiver. By multiplying the both sides of (2.16) with $\mathbf{\Lambda}_k^{\dagger}$, because of the orthogonal structure of the Alamouti-like channel matrix $\mathbf{\Lambda}_k$, one obtains

$$\tilde{\mathbf{Y}}_k = \mathbf{\Lambda}_k^{\dagger}\mathbf{Y}_k = \begin{pmatrix} \mathbf{\Psi}_k & 0 \\ 0 & \mathbf{\Psi}_k \end{pmatrix}\begin{pmatrix} \mathbf{S}_i \\ \mathbf{S}_{i+1} \end{pmatrix} + \tilde{\mathbf{N}}_k \ . \tag{2.22}$$

Here $\mathbf{\Psi}_k = |\mathbf{\Phi}_{1k}|^2 + |\mathbf{\Phi}_{2k}|^2$ is a $(u+v\text{-}1)\times(u+v\text{-}1)$ diagonal matrix with (i, i) element equal to $|\mathbf{\Phi}_{1k}(i, i)|^2+|\mathbf{\Phi}_{2k}(i, i)|^2$, which is the sum of the squared i^{th} DFT coefficients of first and second channel impulse responses [27]. $\tilde{\mathbf{N}}_k$ is the filtered noise vector with a diagonal covariance matrix equal to diag($\mathbf{\Psi}_k$, $\mathbf{\Psi}_k$). In (2.22), we can see how the signals $\mathbf{S}_i$ and $\mathbf{S}_{i+1}$ of the user are decoupled from the received vector $\mathbf{Y}_k$ using a ZF algorithm.

After the ZF decoupling process, the MMSE equalizer for the m^{th} user, by giving the decoupled signal vector $\tilde{\mathbf{Y}}_k$ in (2.22), can be written as [24]-[29]:

$$\hat{\mathbf{S}}^m = \left(\mathbf{\Lambda}_k^m \mathbf{\Lambda}_k^{m\dagger} + \frac{1}{\gamma_k}\mathbf{I} \right)^{-1} \tilde{\mathbf{Y}}_k \tag{2.23}$$

where $\hat{\mathbf{S}}^m$ includes estimations of $\mathbf{S}_i$ and $\mathbf{S}_{i+1}$ of the m^{th} user, γ_k is the signal-to-noise ratio (SNR) at the k^{th} receiver, $\mathbf{I}$ is the $2(u+v\text{-}1)\times 2(u+v\text{-}1)$ identity matrix. By multiplying $\hat{\mathbf{S}}^m$ with $\mathbf{Q}^{-1}$, the inverse DFT matrix, we obtain the original data, i.e. $\mathbf{s}_i$ and $\mathbf{s}_{i+1}$ in (2.15), in time domain.

The above ZF decouple process can be extended to multiple user system via an iterative algorithm [24]-[29]. Let us rewrite (2.20) as

$$\mathbf{Y}=\begin{pmatrix}\mathbf{Y}_1\\ \mathbf{Y}_2\\ \vdots\\ \mathbf{Y}_K\end{pmatrix}=\left(\begin{array}{ccc|c} \overbrace{\boldsymbol{\Lambda}_1^1 & \boldsymbol{\Lambda}_1^2 & \cdots}^{A} & \overbrace{\boldsymbol{\Lambda}_1^M}^{B}\\ \boldsymbol{\Lambda}_2^1 & \boldsymbol{\Lambda}_2^2 & \cdots & \boldsymbol{\Lambda}_2^M\\ \vdots & \vdots & \ddots & \vdots\\ \underbrace{\boldsymbol{\Lambda}_K^1 & \boldsymbol{\Lambda}_K^2 & \cdots}_{C} & \underbrace{\boldsymbol{\Lambda}_K^M}_{D}\end{array}\right)\begin{pmatrix}\mathbf{S}^1\\ \mathbf{S}^2\\ \vdots\\ \mathbf{S}^M\end{pmatrix}+\begin{pmatrix}\mathbf{N}_1\\ \mathbf{N}_2\\ \cdots\\ \mathbf{N}_K\end{pmatrix}. \tag{2.24}$$

The above equation can be written in the following compact form

$$\begin{pmatrix}\mathbf{Y}_{-K}\\ \mathbf{Y}_K\end{pmatrix}=\begin{pmatrix}\mathbf{A} & \mathbf{B}\\ \mathbf{C} & \mathbf{D}\end{pmatrix}\begin{pmatrix}\mathbf{S}^{-M}\\ \mathbf{S}^M\end{pmatrix}+\begin{pmatrix}\mathbf{N}_{-K}\\ \mathbf{N}_K\end{pmatrix}, \tag{2.25}$$

where $\mathbf{Y}_{\text{-K}}$ is the $2(K\text{-}1)$ size vector containing the received signal vectors, $\mathbf{Y}_1,\mathbf{Y}_2,\ldots\mathbf{Y}_{K\text{-}1}$. Similarly, $\mathbf{S}^{-M}$ is the $2(M\text{-}1)$ signal block vector and $\mathbf{N}_{-K}$ is the $2(K\text{-}1)$ noise vectors. The matrices $\mathbf{A}$, $\mathbf{B}$, $\mathbf{C}$, and $\mathbf{D}$ are $2(K\text{-}1)\times 2(M\text{-}1)$, $2(K\text{-}1)\times 2$, $2\times 2(M\text{-}1)$ and 2×2 channel impulse response matrices respectively. Note that to clarify the rough dimension of $\mathbf{A}$, $\mathbf{B}$, $\mathbf{C}$, $\mathbf{D}$, $\mathbf{Y}$, $\mathbf{S}$ and $\mathbf{N}$, the length of channel output u+v-1 is omitted in above matrices size description. The decoupling matrix for the $m = M^{\text{th}}$ user can be constructed as [24]-[26]

$$\mathbf{G}^M=\begin{pmatrix}\mathbf{I}_{2(K-1)} & -\mathbf{B}\mathbf{D}^{-1}\\ -\mathbf{C}\mathbf{A}^{-1} & \mathbf{I}_2\end{pmatrix}. \tag{2.26}$$

After multiplying $\mathbf{G}^M$ with $\mathbf{Y}$ in (2.24), an equation similar to (2.22) can be obtained

$$\begin{pmatrix}\mathbf{R}^{-M}\\ \mathbf{R}^M\end{pmatrix}=\mathbf{G}^M\mathbf{Y}=\begin{pmatrix}(\mathbf{A}-\mathbf{B}\mathbf{D}^{-1}\mathbf{C})\mathbf{S}^{-M}\\ (\mathbf{D}-\mathbf{C}\mathbf{A}^{-1}\mathbf{B})\mathbf{S}^M\end{pmatrix}+\begin{pmatrix}\tilde{\mathbf{N}}^{-M}\\ \tilde{\mathbf{N}}^M\end{pmatrix}. \tag{2.27}$$

Note that $\mathbf{R}^M$, which is the received signal from the M^{th} user, is separated out from the other users. The matrices $\mathbf{A}\text{-}\mathbf{B}\mathbf{D}^{-1}\mathbf{C}$ and $\mathbf{D}\text{-}\mathbf{C}\mathbf{A}^{-1}\mathbf{B}$ have the Alamouti-like structure also [27]. So, by further iteration on the processed received signal vector $\mathbf{R}^{-M}$ as (2.22)-(2.27), all the data vectors of other users can be recovered.

According to (2.27), it is clear that the decoupled signal vector $\mathbf{R}^M$ can be considered as the transmitted signal symbol vector $\mathbf{S}^M$ convolved with the channel $\tilde{\mathbf{\Lambda}}^M = \mathbf{D} - \mathbf{C}\mathbf{A}^{-1}\mathbf{B}$ in time domain. So, MMSE equalizer for $\mathbf{R}^M$ can be realized by replacing $\mathbf{\Lambda}$ in (2.23) with $\tilde{\mathbf{\Lambda}}^M$.

2.2.3.2 *MMSE joint decoupling and equalizer*

The ZF decouple process enhances the impact of noise. To avoid this, a joint MMSE solution can be developed to recover all the data symbols of all the users directly from (2.20) as

$$\widehat{\mathbf{S}} = \mathbf{\Delta}^{\dagger}\left(\mathbf{\Delta}\mathbf{\Delta}^{\dagger} + \frac{1}{\gamma}\mathbf{J}\right)^{-1}\mathbf{Y}\ . \tag{2.28}$$

Here

$$\mathbf{\Delta} = \begin{pmatrix} \mathbf{\Lambda}_1^1 & \mathbf{\Lambda}_1^2 & \cdots & \mathbf{\Lambda}_1^M \\ \mathbf{\Lambda}_2^1 & \mathbf{\Lambda}_2^2 & \cdots & \mathbf{\Lambda}_2^M \\ \vdots & \vdots & \ddots & \vdots \\ \mathbf{\Lambda}_K^1 & \mathbf{\Lambda}_K^1 & \cdots & \mathbf{\Lambda}_K^M \end{pmatrix}, \mathbf{J} = \begin{pmatrix} \mathbf{I} & \mathbf{I} & \cdots & \mathbf{I} \\ \mathbf{I} & \mathbf{I} & \cdots & \mathbf{I} \\ \vdots & \vdots & \ddots & \vdots \\ \mathbf{I} & \mathbf{I} & \cdots & \mathbf{I} \end{pmatrix},$$

and $\mathbf{I}$ is the identity matrix with the size as each Λ and γ is the average SNR. Transmitted symbols in time domain can be obtained by multiplying $\widehat{\mathbf{S}}$ in (2.28) with the inverse DFT matrix $\mathbf{Q}^{-1}$ with the corresponding size. The disadvantage of joint decoupling and equalization is its higher computational complexity. We have used this approach in the simulation of next section.

2.2.4 Simulation Setup and Performance Comparison

Monte-Carlo simulations are performed for system performance analysis. The same shallow water channel as Section 2.1.3 is used to simulate the proposed multiuser vector sensor system. Simulation parameters are shown in Table 2.4.

The three users are vertically lined up at depths 25, 35 and 45 m below the water surface, as shown in Figure 2.11. The vector sensor receiver is 63 m below the water surface. The two transmit pressure sensors of each user are vertically separated by λ, the wavelength. Each user is transmitting space-time block coded BPSK symbols with a bit rate of 2400 bits/sec. The signal vector **s** for each user includes equi-probable ±1 iid symbols. Alamouti's space-time block code [28] is used in simulations.

Table 2.4 Simulation and Channel Parameters

Water Depth (m)	81.158
Transmitters Depth (m), User 1	25
Transmitters Depth (m), User 2	35
Transmitters Depth (m), User 3	45
Bottom Types	Coarse silt
Receiver Depth (m)	63
Receiver Range (km)	1
Carrier Frequency (kHz)	12
Sampling Frequency (kHz)	48
Data Rate (kbps)	2.4
Nominal Sound Speed (m/s)	1500
Wavelength λ (m)	0.125
Transmit sensor spacing of each user	λ

2.2.4.1 *System Performance*

Figure 2.12 shows the bit error rate (BER) performance of three systems: a single user system with two pressure transmitters and one pressure receiver; a three user system similar to Figure 2.11, where the vector sensor receiver is replaced by a three element pressure sensor array with λ element spacing; and a three user vector sensor system of Figure 2.11.

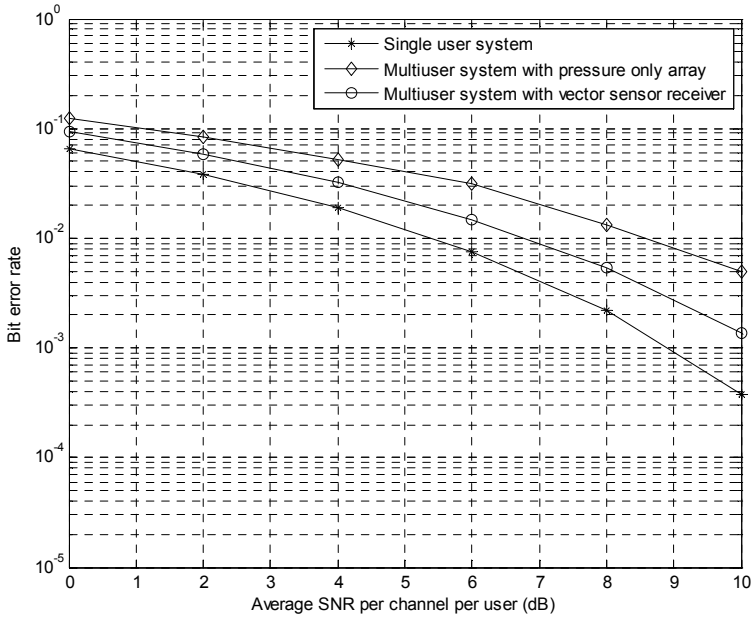

Figure 2.12 BER performance for single and multiuser systems.

According to Figure 2.12, the vector sensor system has a better BER performance than the pressure only array receiver. This could be because of the correlations among the pressure channels. To investigate this, let the normalized channels in the vector sensor be defined as $\tilde{\mathbf{p}} = (\mathbf{p} - \mu_p)/\sigma_p$, $\tilde{\mathbf{p}}^y = (\mathbf{p}^y - \mu_p^y)/\sigma_p^y$ and $\tilde{\mathbf{p}}^z = (\mathbf{p}^z - \mu_p^z)/\sigma_p^z$, where μ and σ are sample mean and standard deviation, respectively. Also let |**A**| denote a matrix whose elements are the absolute values of the elements of the matrix. In what follows, we calculate the average absolute value of the correlation coefficients among all the channels of the vector sensor receiver and the pressure-only array receiver, respectively:

$$\left|\begin{pmatrix}\tilde{\mathbf{p}}^{\dagger}\\(\tilde{\mathbf{p}}^{y})^{\dagger}\\(\tilde{\mathbf{p}}^{z})^{\dagger}\end{pmatrix}\begin{pmatrix}\tilde{\mathbf{p}} & \tilde{\mathbf{p}}^{y} & \tilde{\mathbf{p}}^{z}\end{pmatrix}\right| = \begin{pmatrix}1 & 0.84 & 0.14\\0.84 & 1 & 0.13\\0.14 & 0.13 & 1\end{pmatrix}, \quad \left|\begin{pmatrix}\tilde{\mathbf{p}}_1^{\dagger}\\\tilde{\mathbf{p}}_2^{\dagger}\\\tilde{\mathbf{p}}_3^{\dagger}\end{pmatrix}\begin{pmatrix}\tilde{\mathbf{p}}_1 & \tilde{\mathbf{p}}_2 & \tilde{\mathbf{p}}_3\end{pmatrix}\right| = \begin{pmatrix}1 & 0.99 & 0.97\\0.99 & 1 & 0.99\\0.97 & 0.99 & 1\end{pmatrix}.$$

(vector sensor receiver) (pressure-only array receiver)

The high correlations among the elements of the pressure sensor array, 0.97 and 0.99, may explain the inferior performance of the pressure-only array. By increasing the element spacing in the pressure-only array, its BER might be decreased [30]. A statistical model for correlations in a vector sensor will be given in Chapter 3.

2.2.4.2 *Impact of Imperfect Channel Estimation*

The BERs in Figure 2.12 are obtained assuming perfect knowledge of the channel matrices. Here we study the influence of error in channel estimation. Figure 2.13 shows the impact of channel estimation error on the multiuser vector sensor system. It results in a 4dB loss in SNR.

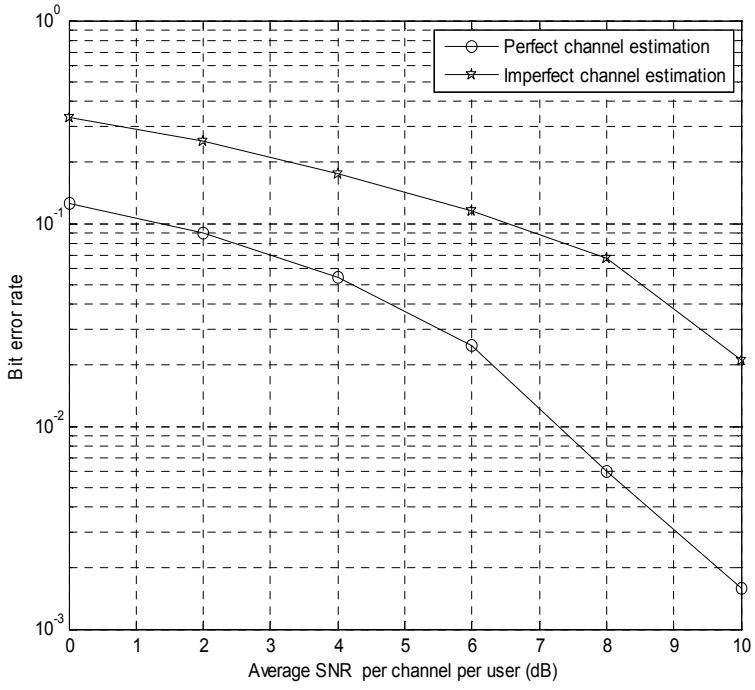

Figure 2.13 The impact of imperfect channel estimation on the performance of the multiuser vector sensor system.

2.2.4.3 *Effect of Transmit Sensor Spacing*

In the previous figures the transmit element spacing was fixed at λ. Since spatial correlation exists between the transmit pressure sensors also, it is important to study the effect of transmit sensor spacing. Figure 2.14 shows BERs for the three user vector sensor system with λ, 4λ and 8λ transmit sensor spacing at each user. We see that with the increase of the transmit sensor spacing, the system performance increases as well.

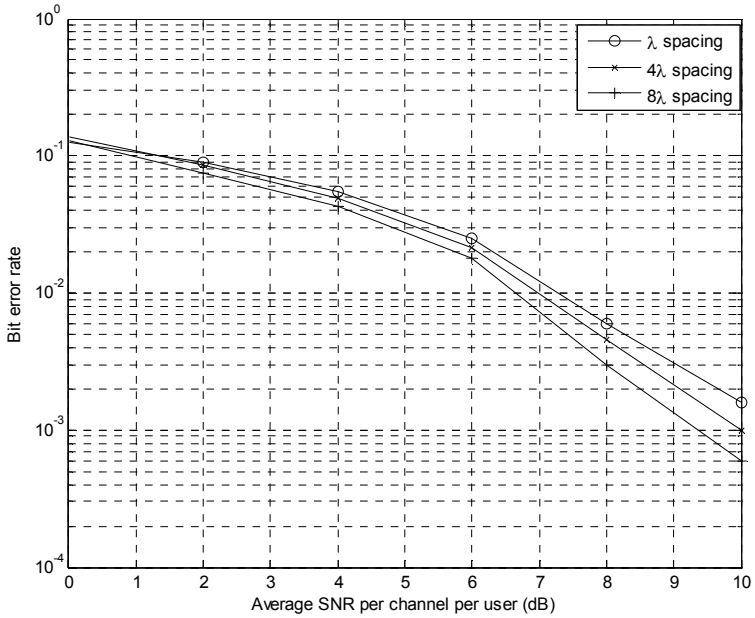

Figure 2.14 The impact of transmit element spacing on the multiuser vector sensor system.

2.2.4.4 *Individual User Performance*

The BER in Figure 2.12 is the multiuser system performance, obtained by averaging over the BERs of three users. In Figure 2.15, however, the individual BER of each user in the vector sensor multiuser system is shown. We observe that the performance of user 2 is much worse than the other users. This could be because user 2 is located in between the other two users in Figure 2.11. So, perhaps it receives more multiple access interference.

2.2.4.5 *Comparison of Separate and Joint Decoupling /Equalization Algorithms*

In Figure 2.16 the BERs performance are shown by using the separate and joint decoupling/equalization algorithms. There is a 3 dB SNR loss, possibly because of the noise enhancement by the ZF decoupler.

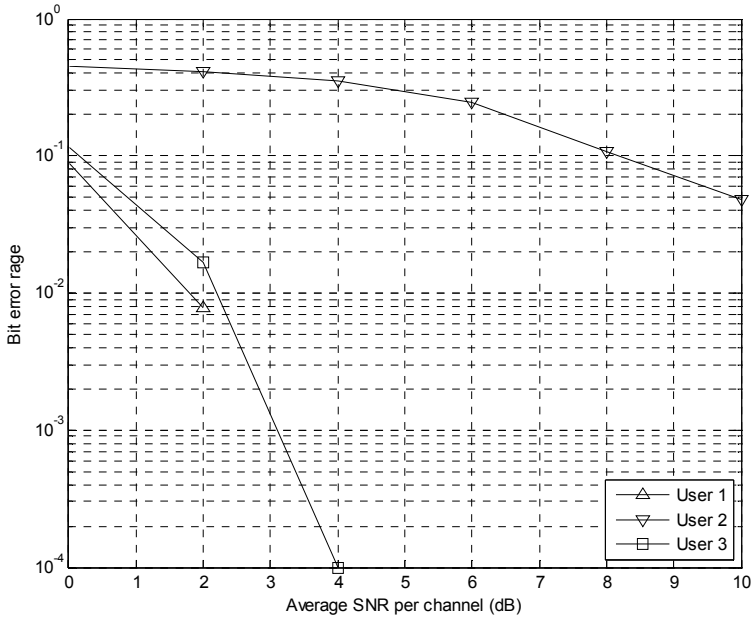

Figure 2.15 Individual BER of each user in the vector sensor multiuser system.

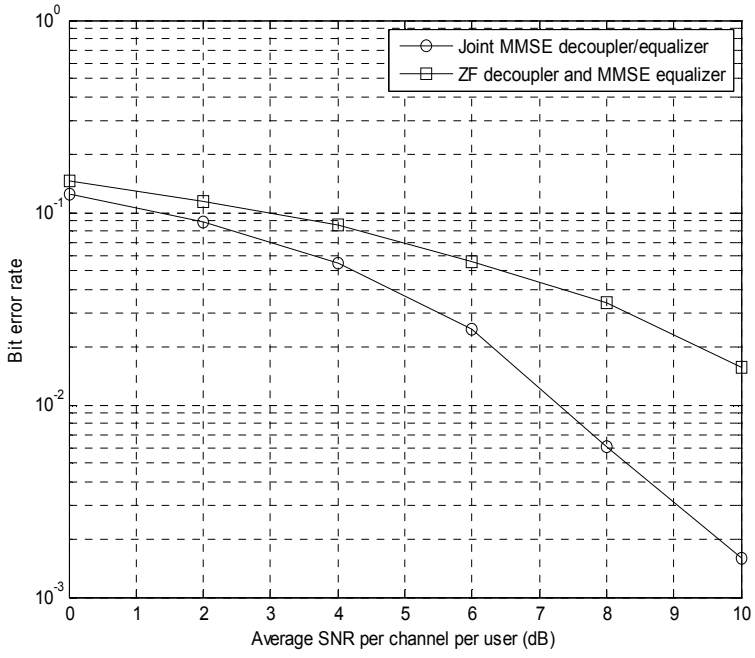

Figure 2.16 Performance of the vector sensor multiuser system with ZF decoupler/MMSE equalizer and joint MMSE decoupler/equalizer.

2.3 Summary and Conclusion

In this chapter, we have introduced and developed the concept of data detection and equalization in underwater communication channels using acoustic vector sensors. Basic system equations for such a receiver are derived and channel equalization using these sensors is formulated. Signal and noise power characteristics in such sensors are also investigated. Via extensive simulations under different propagation scenarios, the performance of a vector sensor equalizer is determined and compared with single and multiple pressure sensor receivers.

Furthermore, based on the new vector sensor receiver, a multiple users system for underwater channels is proposed that does not need spreading codes. Performance of a vector sensor receiver for three users is investigated also. The BER of the proposed multiuser space-time coded vector sensor system is close to the BER of the single user system. This means that the data symbols of the three users are successfully separated and estimated using a vector sensor.

In summary, we have shown that using the vector sensor receiver, one new underwater acoustic communication system can be built up. And by using space-time block codes over the scalar and vector components of the acoustic field, one can have a high rate underwater multiuser system without reduction in the transmission rate of each user. This is particularly useful in highly bandwidth-constrained underwater channels. Small size of the vector sensor receiver in the proposed system is noteworthy, as the compact vector sensor measures all particle velocity channels at a single point in space. This is important for systems which have size limitations such as unmanned underwater vehicles.

CHAPTER 3

CORRELATION STUDY FOR VECTOR SENSOR ARRAY

3.1 Signal Correlation Model

The new underwater communication system with vector sensor receivers was introduced in Chapter 2, in both single-user and multiuser cases. Since the underwater acoustic channel is a typical time-varying multipath channel, the study of the channel correlations is necessary to design or optimize the new vector sensor underwater communication system. In this chapter, we develop a statistical framework to represent the channel transfer functions, then we derive and discuss the spatial, frequency and temporal correlations for given scenarios. To discover the channel characteristics, a vector sensor array system with one pressure transmitter and three vector sensor receivers is setup which is shown in Figure 3.1. Each vector sensor measures the pressure, as well as the *y* and *z* component of the acoustic particle velocity, all in a single point.

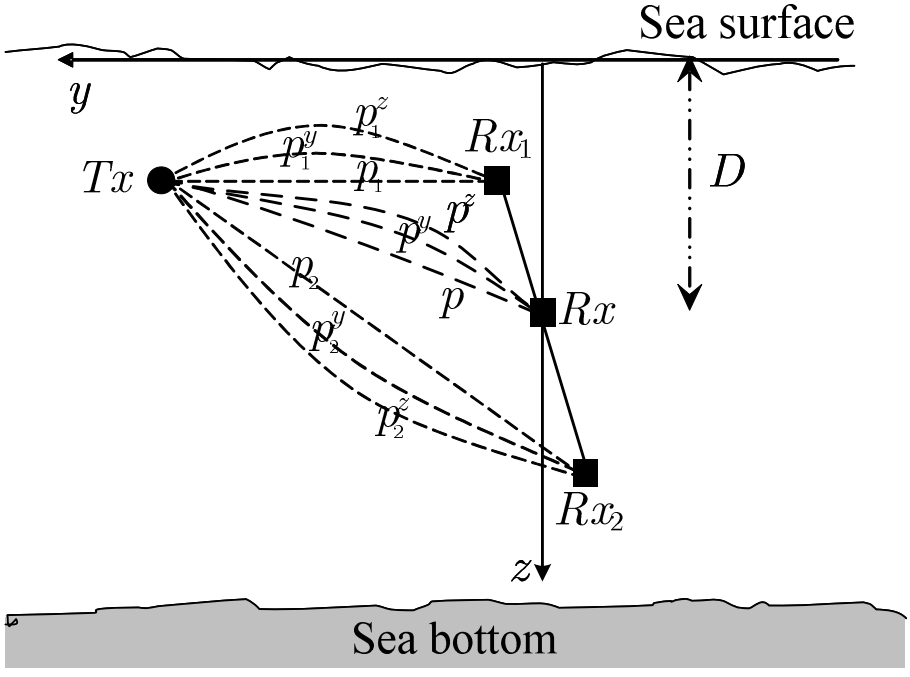

Figure 3.1 A vector sensor array with one pressure transmitter and three vector sensor receivers.

3.1.1 Statistical Representation of Pressure and Velocity Channels

First we develop a statistical framework, which concentrates on channel characterization using probabilistic models for the random components of the propagation environment. In this way, the statistical behavior of the channel can be imitated, and convenient closed-form expressions for the correlation functions of interest can be derived. These vector sensor parametric correlation expressions allow engineers to design, simulate, and asses a variety of design schemes under different channel conditions.

In what follows we provide proper statistical representations for pressure and velocity channels in shallow waters. These channel representations will be used in Section 3.1.2, to calculate different types of channel correlations.

3.1.1.1 *Pressure-related channel functions*

In this subsection we define and focus on the pressure channel functions over the angle, space, delay, frequency and time domains.

Figure 3.2 shows the system of Figure 3.1, as well as the geometrical details of the received rays in a shallow water channel, with three vector sensor receivers. Two-dimensional propagation of plane waves in the *y*-*z* (range-depth) plane is assumed, in a time-invariant environment with D_0 as the water depth. Vector sensor 1 is located at $y = L_y / 2$ and $z = D - (L_z / 2)$, vector sensor 2 is at $y = -L_y / 2$ and $z = D + (L_z / 2)$ and vector sensor *Rx* is located at $y = 0$ and $z = D$. Here, L_y and L_z are the projections of the array length L at *y* and *z* axis, respectively, such that $L = (L_y + L_z)^{1/2}$. All the angles are measured with respect to the positive direction of *y*, counterclockwise. We model the rough sea bottom and its surface as collections of N^b and N^s scatterers, respectively, such that $N^b >> 1$ and $N^s >> 1$. In this work, the small letters *b* and *s* refer to the bottom and surface, respectively. In Figure 3.2, for example, the *i*-th bottom scatterer is represented by O_i^b, $i = 1, 2, ..., N^b$, whereas O_m^s denotes the *m*-th surface scatterer, $m = 1, 2, ..., N^s$. Rays scattered from the bottom and the surface toward the vector sensors

are shown by solid lines. The rays scattered from O_i^b hit Rx_1 and Rx_2 at the angle of arrivals (AOAs) $\gamma_{i,1}^b$ and $\gamma_{i,2}^b$, respectively. The traveled distances are labeled by $\xi_{i,1}^b$ and $\xi_{i,2}^b$, respectively. Similarly, the scattered rays from O_m^s impinge Rx_1 and Rx_2 at the AOAs $\gamma_{m,1}^s$ and $\gamma_{m,2}^s$, respectively, with $\xi_{m,1}^s$ and $\xi_{m,2}^s$ as the traveled distances shown in Figure 3.2. The vector sensor receivers move at the speed *u*, in the direction specified by φ in Figure 3.2.

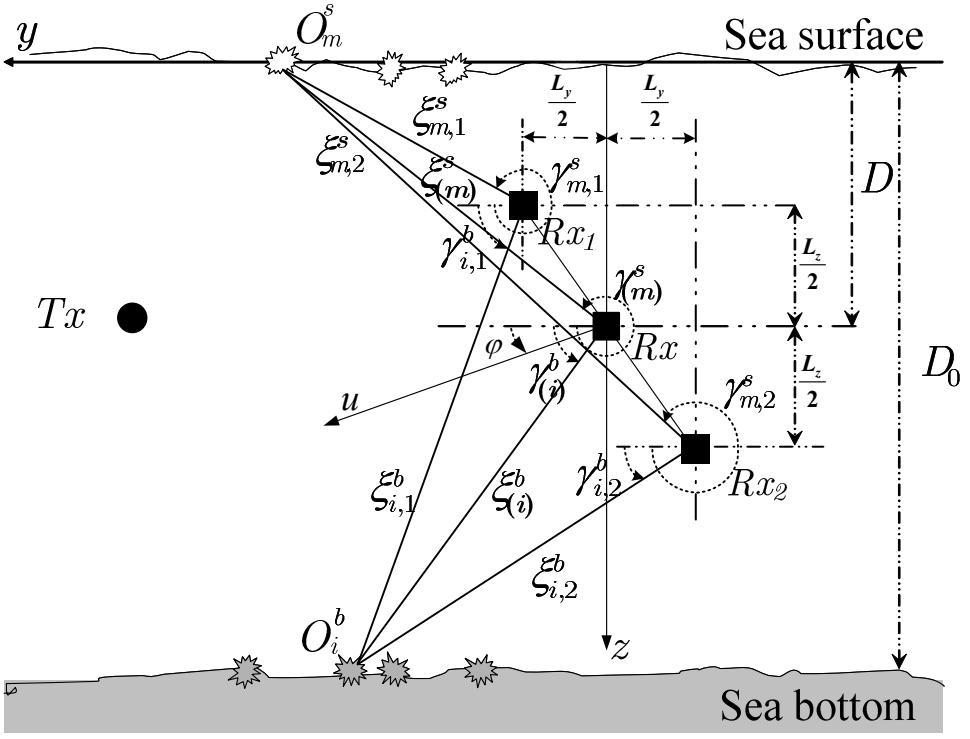

Figure 3.2 Geometrical representation of the received rays at a mobile vector sensor array in a shallow water multipath channel.

Let τ and γ represent the delay (travel time) and the AOA (measured with respect to the positive direction of *y*, counterclockwise). Then with the consideration of amplitude, phase and Doppler shift, in the angle-delay domain, the time varying impulse responses of the pressure subchannels $Tx - Rx_1$ and $Tx - Rx_2$, represented by $\chi_1(t,\gamma,\tau)$ and $\chi_2(t,\gamma,\tau)$, respectively, can be written as

$$\chi_1(t,\gamma,\tau)=\left(\frac{\Lambda_b}{N^b}\right)^{1/2}\sum_{i=1}^{N^b}a_i^b\exp(j\psi_i^b)\exp(j2\pi f_M\cos(\gamma_{i,1}^b-\varphi)t)\,\delta(\gamma-\gamma_{i,1}^b)\delta(\tau-\tau_{i,1}^b)+\left(\frac{1-\Lambda_b}{N^s}\right)^{1/2}\sum_{m=1}^{N^s}a_m^s\exp(j\psi_m^s)\exp(j2\pi f_M\cos(\gamma_{m,1}^s-\varphi)t)\,\delta(\gamma-\gamma_{m,1}^s)\delta(\tau-\tau_{m,1}^s), \tag{3.1}$$

$$\chi_2(t,\gamma,\tau)=\left(\frac{\Lambda_b}{N^b}\right)^{1/2}\sum_{i=1}^{N^b}a_i^b\exp(j\psi_i^b)\exp(j2\pi f_M\cos(\gamma_{i,2}^b-\varphi)t)\,\delta(\gamma-\gamma_{i,2}^b)\delta(\tau-\tau_{i,2}^b)+\left(\frac{1-\Lambda_b}{N^s}\right)^{1/2}\sum_{m=1}^{N^s}a_m^s\exp(j\psi_m^s)\exp(j2\pi f_M\cos(\gamma_{m,2}^s-\varphi)t)\,\delta(\gamma-\gamma_{m,2}^s)\delta(\tau-\tau_{m,2}^s). \tag{3.2}$$

In eq. (3.1) and (3.2), $\delta(.)$ is the Dirac delta, $a_i^b>0$ and $a_m^s>0$ represent the amplitudes of the rays scattered from S_i^b and S_m^s, respectively, whereas $\psi_i^b\in[0,2\pi)$ and $\psi_m^s\in[0,2\pi)$ stand for the associated phases. The four delay symbols in (3.1) and (3.2) represent the travel times from the bottom and surface scatterers to the two vector sensors. For example, $\tau_{i,1}^b$ denotes the travel time from S_i^b to Rx_1, and so on. As becomes clear in Appendix A, the factors $(N^b)^{-1/2}$ and $(N^s)^{-1/2}$ are included in (3.1), (3.2) and the subsequent channel functions, for power normalization. $\exp(j2\pi f_M\cos(\gamma-\varphi)t)$ corresponds to its Doppler shift introduced by the motion of the receiver [38][43]. Here $f_M=u/\lambda$ is the maximum Doppler shift. Also $0\le\Lambda_b\le1$ represents the amount of the contribution of the bottom scatterers, as explained immediately after eq. (A.5) in Appendix A. A close to one value for Λ_b indicates that most of the received power is coming from the bottom. Of course the amount of the contribution of the surface is given by $1-\Lambda_b$.

A Dirac delta in the angle domain such as $\delta(\gamma-\tilde{\gamma})$ corresponds to a plane wave with the AOA of $\tilde{\gamma}$, whose equation at an arbitrary point (y,z) is $\exp(jk[y\cos(\tilde{\gamma})+z\sin(\tilde{\gamma})])$. Using similar plane wave equations for the other angular delta functions in (3.1) and (3.2), the impulse responses of the pressure subchannels $Tx-Rx_1$ and $Tx-Rx_2$ in the delay-space domain can be respectively written as

$$p_1(\tau,t)=\left(\frac{\Lambda_b}{N^b}\right)^{1/2}\left.\sum_{i=1}^{N^b}a_i^b\exp(j\psi_i^b)\exp(jk[y\cos(\gamma_{i,1}^b)+z\sin(\gamma_{i,1}^b)])\right|_{\substack{y=L_y/2,\\ z=D-L_z/2}}$$
$$\left.\exp(j2\pi f_M\cos(\gamma_{i,1}^b-\varphi)t)\delta(\tau-\tau_{i,1}^b)\right.$$
$$+\left(\frac{1-\Lambda_b}{N^s}\right)^{1/2}\left.\sum_{m=1}^{N^s}a_m^s\exp(j\psi_m^s)\exp(jk[y\cos(\gamma_{m,1}^s)+z\sin(\gamma_{m,1}^s)])\right|_{\substack{y=L_y/2,\\ z=D-L_z/2}},\tag{3.3}$$
$$\left.\exp(j2\pi f_M\cos(\gamma_{m,1}^s-\varphi)t)\delta(\tau-\tau_{m,1}^s)\right.$$

$$p_2(\tau,t)=\left(\frac{\Lambda_b}{N^b}\right)^{1/2}\left.\sum_{i=1}^{N^b}a_i^b\exp(j\psi_i^b)\exp(jk[y\cos(\gamma_{i,2}^b)+z\sin(\gamma_{i,2}^b)])\right|_{\substack{y=-L_y/2,\\ z=D+L_z/2}}$$
$$\left.\exp(j2\pi f_M\cos(\gamma_{i,2}^b-\varphi)t)\delta(\tau-\tau_{i,2}^b)\right.$$
$$+\left(\frac{1-\Lambda_b}{N^s}\right)^{1/2}\left.\sum_{m=1}^{N^s}a_m^s\exp(j\psi_m^s)\exp(jk[y\cos(\gamma_{m,2}^s)+z\sin(\gamma_{m,2}^s)])\right|_{\substack{y=-L_y/2,\\ z=D+L_z/2}}.\tag{3.4}$$
$$\left.\exp(j2\pi f_M\cos(\gamma_{m,2}^s-\varphi)t)\delta(\tau-\tau_{m,2}^s)\right.$$

Based on the definition of the spatial Fourier transform [56], $p_1(\tau,t)$ and $p_2(\tau,t)$ can be considered as the spatial Fourier transforms of $\chi_1(t,\gamma,\tau)$ and $\chi_2(t,\gamma,\tau)$, respectively, with respect to γ. The terms y and z in (3.3) and (3.4) are intentionally maintained, as in the sequel we need to calculate the spatial gradients of the pressure with respect to y and z, to obtain the velocities.

By taking the Fourier transform of (3.3) and (3.4) with respect to τ, we respectively obtain the complex baseband transfer functions of the pressure subchannels $Tx-Rx_1$ and $Tx-Rx_2$ in the frequency, time and space domain

$$P_1(f,t)=\left(\frac{\Lambda_b}{N^b}\right)^{1/2}\left.\sum_{i=1}^{N^b}a_i^b\exp(j\psi_i^b)\exp(jk[y\cos(\gamma_{i,1}^b)+z\sin(\gamma_{i,1}^b)])\right|_{\substack{y=L_y/2,\\ z=D-L_z/2}}$$
$$\left.\exp(-j2\pi f\tau_{i,1}^b)\exp(j2\pi f_M\cos(\gamma_{i,1}^b-\varphi)t)\right.$$
$$+\left(\frac{1-\Lambda_b}{N^s}\right)^{1/2}\left.\sum_{m=1}^{N^s}a_m^s\exp(j\psi_m^s)\exp(jk[y\cos(\gamma_{m,1}^s)+z\sin(\gamma_{m,1}^s)])\right|_{\substack{y=L_y/2,\\ z=D-L_z/2}},\tag{3.5}$$
$$\left.\exp(-j2\pi f\tau_{m,1}^s)\exp(j2\pi f_M\cos(\gamma_{m,1}^s-\varphi)t)\right.$$

$$P_2(f,t)=\left(\frac{\Lambda_b}{N^b}\right)^{1/2}\left.\sum_{i=1}^{N^b}a_i^b\exp(j\psi_i^b)\exp(jk[y\cos(\gamma_{i,2}^b)+z\sin(\gamma_{i,2}^b)])\right|_{\substack{y=-L_y/2,\\ z=D+L_z/2}}$$
$$\left.\exp(-j2\pi f\tau_{i,2}^b)\exp(j2\pi f_M\cos(\gamma_{i,2}^b-\varphi)t)\right.$$
$$+\left(\frac{1-\Lambda_b}{N^s}\right)^{1/2}\left.\sum_{m=1}^{N^s}a_m^s\exp(j\psi_m^s)\exp(jk[y\cos(\gamma_{m,2}^s)+z\sin(\gamma_{m,2}^s)])\right|_{\substack{y=-L_y/2,\\ z=D+L_z/2}}.\tag{3.6}$$
$$\left.\exp(-j2\pi f\tau_{m,2}^s)\exp(j2\pi f_M\cos(\gamma_{m,2}^s-\varphi)t)\right.$$

3.1.1.2 *Velocity-related channel functions*

Following the definition of the pressure-equivalent velocity in (2.2), the velocity channels of interest in the delay-space and frequency-space domains can be written as

$$p_q^y(t,\tau) = (jk)^{-1}\dot{p}_q(t,\tau), \quad p_q^z(t,\tau) = (jk)^{-1}p_q'(t,\tau), \quad q = 1,\ 2, \tag{3.7}$$

$$P_q^y(f,t) = (jk)^{-1}\dot{P}_q(f,t), \quad P_q^z(f,t) = (jk)^{-1}P_q'(f,t), \quad q = 1,\ 2, \tag{3.8}$$

where $p_q(t,\tau)$ and $P_q(f,t)$, $q = 1,2$, are given in (3.3)-(3.6). Furthermore, dot and prime denote the partial spatial derivatives $\partial/\partial y$ and $\partial/\partial z$, respectively, of the spatial complex plane waves in (3.3)-(3.6). Clearly for $q = 1,2$, $p_q^y(t,\tau)$ and $p_q^z(t,\tau)$ are the pressure-equivalent impulse responses of the velocity subchannels in the y and z directions, respectively. Moreover, $P_q^y(f,t)$ and $P_q^z(f,t)$ represent the pressure-equivalent transfer functions of the velocity subchannels in the y and z directions, respectively, with $q = 1,2$.

3.1.2 Complete Channel Correlation Expressions

In a given shallow water channel, obviously the numerical values of all the amplitudes, phases, AOAs, delays and Doppler shift in (3.3)-(3.6) are complicated functions of environmental characteristics such as the irregular shape of the sea bottom and its layers/losses, volume microstructures, etc. Due to the uncertainty and complexity in exact determination of all these variables, we model them as random variables. More specifically, we assume all the amplitudes $\{a_i^b\}_i$ and $\{a_m^s\}_m$ are positive uncorrelated random variables, uncorrelated with the phases $\{\psi_i^b\}_i$ and $\{\psi_m^s\}_m$. In addition, all the phases $\{\psi_i^b\}_i$ and $\{\psi_m^s\}_m$ are uncorrelated, uniformly distributed over $[0,2\pi)$. The statistical properties of the AOAs, delays and Doppler shifts will be discussed later. Overall, all the pressure and velocity channel functions in (3.3)-(3.8) are random processes in space, frequency and time domains. In what follows, first we derive the exact expression for the pressure spatial, frequency and temporal correlation. Then we show how other correlations of interest can be calculated from the pressure correlation.

3.1.2.1 *Pressure channel correlation*

The definition of the pressure channel frequency-space correlation is given by $C_{P_2P_1}(\Delta f,\Delta t,L_z,L_y)=E[P_2(f+\Delta f,t+\Delta t)P_1^*(f,t)]$. Here Δf and Δt are the spacing in frequency and time domain, respectively. L_z and L_y are the vertical and horizontal distances between the two vector sensors, respectively, * is complex conjugate, and E is the expectation calculated over the distribution of AOAs from the bottom and the surface. As shown in Appendix A, based on (3.5) and (3.6), the complete frequency, temporal and spatial correlation of the pressure channel can be shown as

$$
\begin{aligned}
&C_{P_2P_1}(\Delta f,\Delta t,L_z,L_y)\\
&=\Lambda_b\int_{\gamma^b=0}^{\pi}\left\{\begin{array}{l} w^b(\gamma^b)\exp[-jkL_y(\cos(\gamma_2^b)+\cos(\gamma_1^b))/2]\exp[jkD(\sin(\gamma_2^b)-\sin(\gamma_1^b))]\\ \exp[jkL_z(\sin(\gamma_2^b)+\sin(\gamma_1^b))/2]\exp[j2\pi f(\tau_1^b-\tau_2^b)]\\ \exp[-j2\pi\Delta f\tau_2^b]\exp[j2\pi f_M\cos(\gamma^b-\varphi)\Delta t]d\gamma^b\end{array}\right\}\\
&+(1-\Lambda_b)\int_{\gamma^s=\pi}^{2\pi}\left\{\begin{array}{l} w^s(\gamma^s)\exp[-jkL_y(\cos(\gamma_2^s)+\cos(\gamma_1^s))/2]\exp[jkD(\sin(\gamma_2^s)-\sin(\gamma_1^s))]\\ \exp[jkL_z(\sin(\gamma_2^s)+\sin(\gamma_1^s))/2]\exp[j2\pi f(\tau_1^s-\tau_2^s)]\\ \exp[-j2\pi\Delta f\tau_2^s]\exp[j2\pi f_M\cos(\gamma^s-\varphi)\Delta t]d\gamma^s\end{array}\right\}.
\end{aligned}
\tag{3.9}
$$

Eq. (3.9) is a frequency, temporal and spatial correlation model for the pressure field which holds for any AOA probability density functions (PDFs) that may be chosen for $w^b(\gamma^b)$ and $w^s(\gamma^s)$. In what follows first we use (3.9) to derive expressions for various spatial, frequency and temporal correlations, which hold for any AOA PDF. Then in Section 3.2 we use a flexible parametric PDF for the AOA, to obtain easy-to-use and closed-from expressions for correlations of special case, vertical vector sensor array.

In (3.9), γ^b and γ^s are the AOAs of rays coming from bottom and surface toward the vector sensor array center, respectively. Eq. (3.9) can be expressed in terms of γ^b and γ^s, the bottom and surface AOAs, respectively, and also L_z, L_y, D and D_0. According to Figure 3.2, it is straightforward to verify

$$\begin{aligned}\sin(\gamma_1^b) &= (D_0 - D + (L_z/2))/\xi_1^b,\\ \sin(\gamma_2^b) &= (D_0 - D - (L_z/2))/\xi_2^b,\end{aligned} \tag{3.10}$$

$$\begin{aligned}\sin(\gamma_1^s) &= -(D - (L_z/2))/\xi_1^s,\\ \sin(\gamma_2^s) &= -(D + (L_z/2))/\xi_2^s,\end{aligned} \tag{3.11}$$

$$\begin{aligned}\cos(\gamma_1^b) &= [(D_0 - D)\cot(\gamma^b) - (L_y/2)]/\xi_1^b,\\ \cos(\gamma_2^b) &= [(D_0 - D)\cot(\gamma^b) + (L_y/2)]/\xi_2^b,\end{aligned} \tag{3.12}$$

$$\begin{aligned}\cos(\gamma_1^s) &= -[D\cot(\gamma^s) + (L_y/2)]/\xi_1^s,\\ \cos(\gamma_2^s) &= -[D\cot(\gamma^s) - (L_y/2)]/\xi_2^s,\end{aligned} \tag{3.13}$$

where $\cot(\cdot) = \cos(\cdot)/\sin(\cdot)$. Moreover, ξ_1^b, ξ_2^b, ξ_1^s and ξ_2^s are rays travel distances from the sea bottom and surface to Rx_1 and Rx_2, respectively, and can be expressed as

$$\xi_1^b = \sqrt{(D_0 - D)^2 + L^2\sin^2(\gamma^b) - 2(D_0 - D)L\cos\left(\frac{\pi}{2} + \gamma^b - \arctan(\frac{L_y}{L_z})\right)\sin(\gamma^b)}\Big/\sin(\gamma^b), \tag{3.14}$$

$$\xi_2^b = \sqrt{(D_0 - D)^2 + L^2\sin^2(\gamma^b) - 2(D_0 - D)L\cos(\frac{\pi}{2} - \gamma^b + \arctan(\frac{L_y}{L_z}))\sin(\gamma^b)}\Big/\sin(\gamma^b), \tag{3.15}$$

$$\xi_1^s = -\sqrt{D^2 + L^2\sin^2(\gamma^s) - 2DL\cos(\frac{\pi}{2} + \gamma^s - \arctan(\frac{L_y}{L_z}))\sin(\gamma^s)}\Big/\sin(\gamma^s), \tag{3.16}$$

$$\xi_2^s = -\sqrt{D^2 + L^2\sin^2(\gamma^s) - 2DL\cos(\frac{\pi}{2} - \gamma^s + \arctan(\frac{L_y}{L_z}))\sin(\gamma^s)}\Big/\sin(\gamma^s), \tag{3.17}$$

where, $L = (L_y + L_z)^{1/2}$. Moreover, τ_q^b and τ_q^s in (3.9), q = 1, 2, are the travel times from bottom and surface scatterers to the Rx_1 and Rx_2, respectively, which are given by

$$\tau_1^b = \frac{\xi_1^b}{c},\ \tau_2^b = \frac{\xi_2^b}{c},\ \tau_1^s = \frac{\xi_1^s}{c},\ \ \tau_2^s = \frac{\xi_2^s}{c}, \tag{3.18}$$

where c is the sound speed.

Pressure channel correlations of two special cases, vertical and horizontal arrays, can be obtained by setting $L_y = 0$ and $L_z = 0$ in (3.9), respectively. The results are given in (3.19) for a vertical array and (3.20) for a horizontal array. With $L_y = 0$ or $L_z = 0$ in (3.9), we obtain the pressure channel correlation functions for vertical vector sensor array or horizontal vector sensor array respectively.

$$\begin{aligned} & C_{P_2P_1}(\Delta f, \Delta t, L_z) \\ & = \Lambda_b \int_{\gamma^b=0}^{\pi} \left\{ \begin{matrix} w^b(\gamma^b)\exp[jkD(\sin(\gamma_2^b)-\sin(\gamma_1^b))]\exp[jkL_z(\sin(\gamma_1^b)+\sin(\gamma_2^b))/2] \\ \exp[j2\pi f(\tau_1^b-\tau_2^b)]\exp[-j2\pi\Delta f\tau_2^b]\exp[j2\pi f_M\cos(\gamma^b-\varphi)\Delta t]d\gamma^b \end{matrix} \right\} \\ & + (1-\Lambda_b)\int_{\gamma^s=\pi}^{2\pi} \left\{ \begin{matrix} w^s(\gamma^s)\exp[jkD(\sin(\gamma_2^s)-\sin(\gamma_1^s))]\exp[jkL_z(\sin(\gamma_1^s)+\sin(\gamma_2^s))/2] \\ \exp[j2\pi f(\tau_1^s-\tau_2^s)]\exp[-j2\pi\Delta f\tau_2^s]\exp[j2\pi f_M\cos(\gamma^s-\varphi)\Delta t]d\gamma^s \end{matrix} \right\}, \end{aligned} \tag{3.19}$$

$$\begin{aligned} & C_{P_2P_1}(\Delta f, \Delta t, L_y) \\ & = \Lambda_b \int_{\gamma^b=0}^{\pi} \left\{ \begin{matrix} w^b(\gamma^b)\exp[-jkL_y(\cos(\gamma_2^b)+\cos(\gamma_1^b))/2]\exp[jkD(\sin(\gamma_2^b)-\sin(\gamma_1^b))] \\ \exp[j2\pi f(\tau_1^b-\tau_2^b)]\exp[-j2\pi\Delta f\tau_2^b]\exp[j2\pi f_M\cos(\gamma^b-\varphi)\Delta t]d\gamma^b \end{matrix} \right\} \\ & + (1-\Lambda_b)\int_{\gamma^s=\pi}^{2\pi} \left\{ \begin{matrix} w^s(\gamma^s)\exp[-jkL_y(\cos(\gamma_2^s)+\cos(\gamma_1^s))/2]\exp[jkD(\sin(\gamma_2^s)-\sin(\gamma_1^s))] \\ \exp[j2\pi f(\tau_1^s-\tau_2^s)]\exp[-j2\pi\Delta f\tau_2^s]\exp[j2\pi f_M\cos(\gamma^s-\varphi)\Delta t]d\gamma^s \end{matrix} \right\}. \end{aligned} \tag{3.20}$$

3.1.2.2 *How to obtain velocity channel correlations*

Now we provide the following two formulas derived from [45], needed in the sequel to calculate velocity-related correlations. Let $\beta(y,z)$ denote a random field in the two-dimensional range-depth plane. Also let $C_\beta(\ell) = E[\beta(y,z+\ell)\beta^*(y,z)]$ be the spatial correlation in the z direction. Then the correlation functions of the derivative of $\beta(y,z)$ in the z direction, i.e., $\beta'(y,z) = \partial\beta(y,z)/\partial z$ can be written as

$$E\left[\beta(y,z+\ell)\{\beta'(y,z)\}^*\right] = -\partial C_\beta(\ell)/\partial\ell, \tag{3.21}$$

$$E\left[\beta'(y,z+\ell)\{\beta'(y,z)\}^*\right] = -\partial^2 C_\beta(\ell)/\partial\ell^2 . \tag{3.22}$$

Similar results hold for the derivative of $\beta(y,z)$ in the y direction, i.e., $\dot{\beta}(y,z) = \partial\beta(y,z)/\partial y$. Therefore, to obtain pressure-velocity and velocity-velocity

channel correlations, one need to take proper derivatives of the pressure channel correlation in (3.9), as summarized below

$$C_{P_2P_1^z}(\Delta f,\Delta t,L_z,L_y)=E[P_2(f+\Delta f,t+\Delta t)\{P_1^z(f,t)\}^*]=(jk)^{-1}\frac{\partial C_{P_2P_1}(\Delta f,\Delta t,L_z,L_y)}{\partial L_z}, \tag{3.23}$$

$$C_{P_2P_1^y}(\Delta f,\Delta t,L_z,L_y)=E[P_2(f+\Delta f,t+\Delta t)\{P_1^y(f,t)\}^*]=(jk)^{-1}\frac{\partial C_{P_2P_1}(\Delta f,\Delta t,L_z,L_y)}{\partial L_y}, \tag{3.24}$$

$$C_{P_2^zP_1^z}(\Delta f,\Delta t,L_z,L_y)=E[P_2^z(f+\Delta f,t+\Delta t)\{P_1^z(f,t)\}^*]=-k^{-2}\frac{\partial^2 C_{P_2P_1}(\Delta f,\Delta t,L_z,L_y)}{\partial L_z^2}, \tag{3.25}$$

$$C_{P_2^yP_1^y}(\Delta f,\Delta t,L_z,L_y)=E[P_2^y(f+\Delta f,t+\Delta t)\{P_1^y(f,t)\}^*]=-k^{-2}\frac{\partial^2 C_{P_2P_1}(\Delta f,\Delta t,L_z,L_y)}{\partial L_y^2}, \tag{3.26}$$

$$C_{P_2^zP_1^y}(\Delta f,\Delta t,L_z,L_y)=E[P_2^z(f+\Delta f,t+\Delta t)\{P_1^y(f,t)\}^*]=-k^{-2}\frac{\partial^2 C_{P_2P_1}(\Delta f,\Delta t,L_z,L_y)}{\partial L_z\partial L_y}. \tag{3.27}$$

In equations (3.23) to (3.27), the time-varying transfer functions for the pressure-equivalent velocity channels at the q-th vector sensor, q = 1, 2, are given in (3.8).

Using (3.9)-(3.18) and (3.23)-(3.27), one can numerically analyze the spatial, frequency and temporal correlations for pressure and velocity channels in an arbitrary vector sensor array. In the following subsection, for a given scenario, the numerical results of those correlations are shown and compared with the corresponding correlation results provided by Monte-Carlo simulation of (3.5), (3.6) and (3.8).

3.1.2.3 *Numerical results*

We still consider the case where the three-element vector sensor array in Figure 3.2 receives signal through two beams: one from the bottom with mean AOA μ_b and angle spread σ_b, and the other one from the surface with mean AOA μ_s and angle spread σ_s. For small angle spreads, we model AOAs as Gaussian distributions for both bottom and

surface components with means μ_b and μ_s and variances σ_b^2 and σ_s^2, respectively , which the PDFs are given as

$$\begin{aligned} w^b(\gamma^b) &= (2\pi\sigma_b^2)^{-1/2} \exp[-(\gamma^b - \mu_b)^2/(2\sigma_b^2)], \quad 0 < \gamma^b < \pi, \\ w^s(\gamma^s) &= (2\pi\sigma_s^2)^{-1/2} \exp[-(\gamma^s - \mu_s)^2/(2\sigma_s^2)], \quad \pi < \gamma^s < 2\pi. \end{aligned} \tag{3.28}$$

For large angle spreads, once can use the von Mises PDF [57] [58]. In Figure 3.3 these two PDFs are plotted in both linear and polar coordinates. The bottom and surface mean AOAs are 10 and 348 degrees, whereas the corresponding angle spread are 2 and 1.5 degrees. The center of the array is place at y = 0 and D = 50 meters, while the water depth is D_0 = 100m. The power ratio is $\Lambda_b = 0.4$.

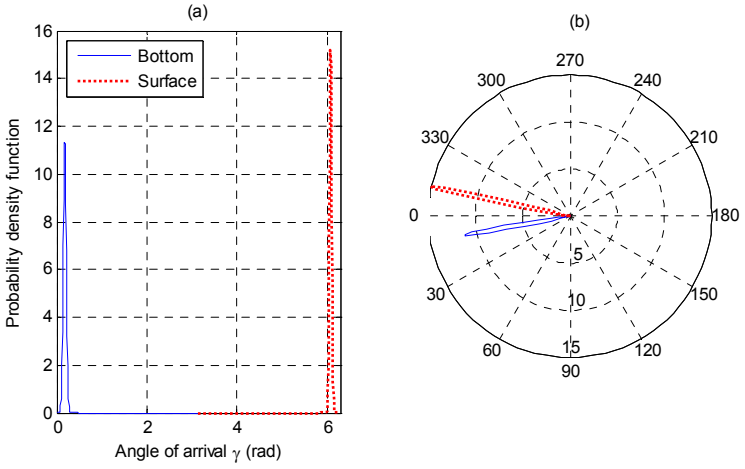

Figure 3.3 The bottom and surface angle-of-arrival Gaussian PDFs: (a) linear plot, (b) polar plot.

Figure 3.4 shows the spatial correlation magnitude of the pressure channel of the oblique array. Particle velocity channel correlations can be calculated by taking derivatives of the pressure channel correlation function in (3.9) with respect to L_z or L_y. Figure 3.5 and Figure 3.6 show the numerical results of frequency and temporal correlations for pressure and velocity channels.

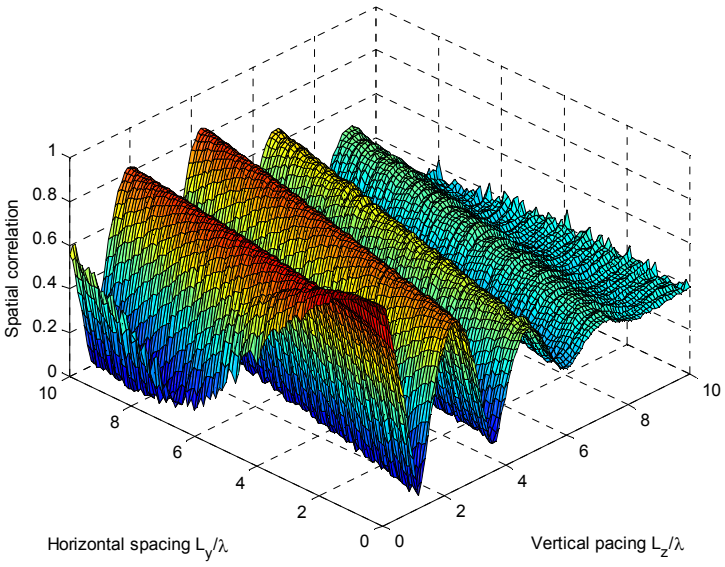

Figure 3.4 Magnitude of the pressure spatial correlations of a vector sensor array.

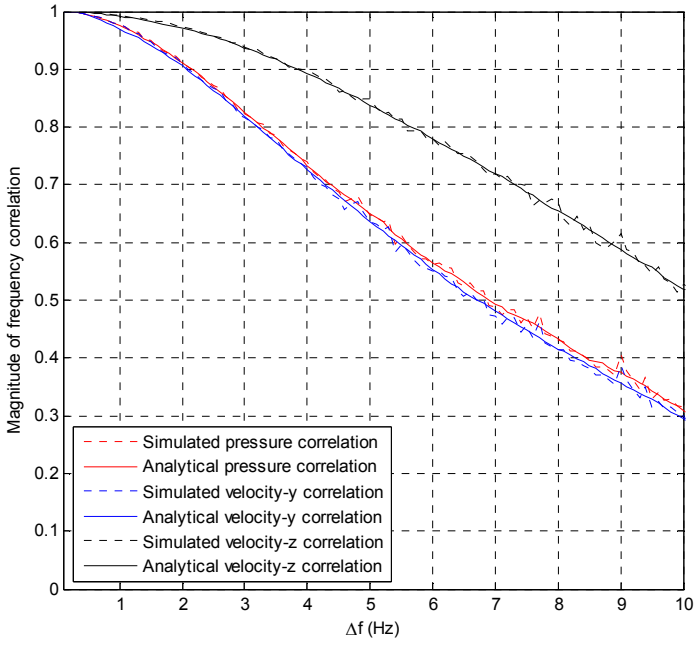

Figure 3.5 Magnitude of frequency correlations in a single vector sensor.

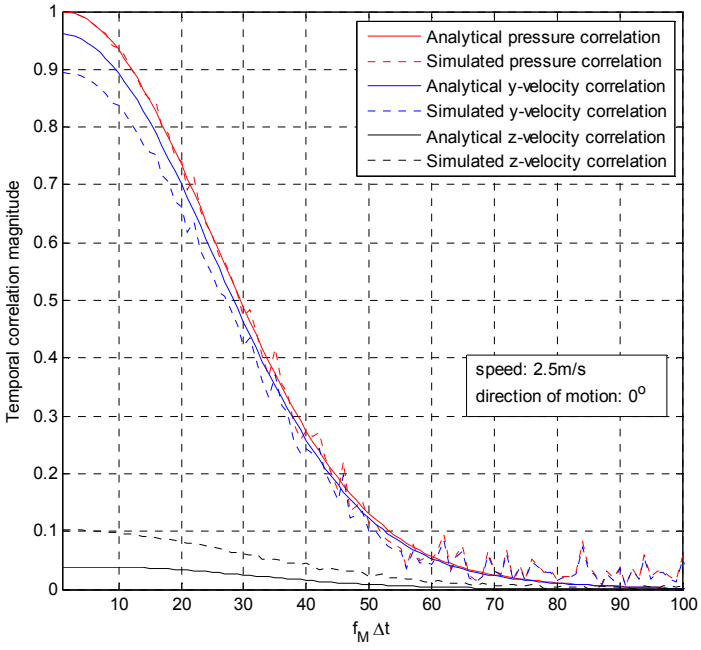

Figure 3.6 Magnitude of temporal correlations in a single vector sensor.

From Figure 3.5 and Figure 3.6, it is clear that for the given scenario and small AOA spread, velocity-y channel has similar correlations as the pressure channel whereas velocity-z channel correlations are significantly different.

3.2 Correlations in Vertical Vector Sensors

Exact correlation expressions include integrals over AOAs which are time consuming to compute. For small angle spread and under certain conditions such as small spacing between array elements, useful integral-free approximation, for vertical and horizontal arrays can be obtained using (3.19) and (3.20). The high order approximations of those two special cases are given in Appendix B. However, the most common use for vector sensor receiver is vertical vector sensor array, which the vector sensors are placed vertical to the sea surface. In this subsection, the detailed analyses for spatial, frequency and temporal correlations for vertical vector sensor array are given, based on the simple closed-form approximation of correlations from eq. (3.9).

3.2.1 Correlations Functions for A Vertical Vector Sensor Array

In what follows, first we derive a closed-form expression for the pressure correlation. Then we show how other correlations of interest can be calculated from the pressure correlation.

From (3.9) and Appendix A, we have derived the following expression

$$\begin{aligned} & C_{P_2P_1}(\Delta f, \Delta t, L_z, L_y) \\ & = \Lambda_b \int_{\gamma^b=0}^{\pi} \left\{ \begin{array}{l} w^b(\gamma^b)\exp[jk(L_y\cos(\gamma^b)+L_z\sin(\gamma^b))] \\ \exp[-j2\pi\Delta f\tau_2^b]\exp[j2\pi f_M\cos(\gamma^b-\varphi)\Delta t]d\gamma^b \end{array} \right\} \\ & + (1-\Lambda_b)\int_{\gamma^s=\pi}^{2\pi} \left\{ \begin{array}{l} w^s(\gamma^s)\exp[jk(L_y\cos(\gamma^s)+L_z\sin(\gamma^s))] \\ \exp[-j2\pi\Delta f\tau_2^s]\exp[j2\pi f_M\cos(\gamma^s-\varphi)\Delta t]d\gamma^s \end{array} \right\}, \text{ as } L_y \to 0, \end{aligned} \tag{3.29}$$

Eq. (3.29) is a spatial, frequency and temporal correlation model for the pressure field which holds for any AOA PDFs. In what follows first we use (3.29) to derive expressions for various spatial frequency and temporal correlations. Then in Section 3.2.2 we use a flexible parametric PDF given as (3.28), to obtain easy-to-use and closed-from expressions for correlations of practical interest. Please note that, L_y is still kept in the correlation functions to help describing the differentiation process.

3.2.1.1 *Spatial correlations for two vector sensors at the same frequency*

(a) Pressure Correlation: At a fixed initial position with $\Delta f = 0$ and $\Delta t = 0$, the spatial pressure correlation for vertical vector sensor array can be obtained from (3.29) as

$$C_{P_2P_1}(L_z) = C_{P_2P_1}(0,0,L_z,L_y) = \int_{\gamma=0}^{2\pi} w(\gamma)\exp(jk(L_y\cos(\gamma)+L_z\sin(\gamma)))d\gamma, \text{ as } L_y \to 0, \tag{3.30}$$

where the overall AOA PDF $w(\gamma)$ is defined as follows, to include both the bottom and surface AOAs and shorten the correlation expressions

$$w(\gamma) = \Lambda_b w^b(\gamma) + (1-\Lambda_b)w^s(\gamma). \tag{3.31}$$

Of course $w^b(\gamma) = 0$ for $\pi < \gamma < 2\pi$, whereas $w^s(\gamma) = 0$ for $0 < \gamma < \pi$.

(b) Pressure-Velocity Correlations: First we look at the *z*-component of the velocity. Here we are interested in $E[P_2(f,t)\{P_1^z(f,t)\}^*] = (-jk)^{-1}E[P_2(f,t)\{P_1'(f,t)\}^*]$, where $P_1^z(f,t)$ is replaced according to (3.8). On the other hand, using (3.23)-(3.27), one has $E[P_2(f,t)\{P_1'(f,t)\}^*] = -\partial E[P_2(f,t)P_1^*(f,t)]/\partial L_z = -\partial C_{P_2P_1}(0,0,L_z,L_y)/\partial L_z$. Therefore

$$\begin{aligned} C_{P_2P_1^z}(L_z) &= E[P_2(f,t)\{P_1^z(f,t)\}^*] = (jk)^{-1}\partial C_{P_2P_1}(0,0,L_z,L_y)/\partial L_z \\ &= \int_{\gamma=0}^{2\pi} w(\gamma)\sin(\gamma)\exp(jk[L_y\cos(\gamma)+L_z\sin(\gamma)])d\gamma, \text{ as } L_y \to 0, \end{aligned} \tag{3.32}$$

where the integral in (3.32) is coming from (3.30). An interesting observation can be made when $w(\gamma)$ is even-symmetric with respect to the *y* axis (symmetry of the AOAs from the bottom and the surface with respect to the horizontal axis *y*). Then with $L_z = 0$ in (3.32) we obtain $E[P_1(f,t)\{P_1^z(f,t)\}^*] = 0$, i.e., the co-located pressure and the *z*-component of the velocity are uncorrelated.

Now we focus on the *y*-component of the velocity. The correlation of interest is $E[P_2(f,t)\{P_1^y(f,t)\}^*] = (-jk)^{-1}E[P_2(f,t)\{\dot{P}_1(f,t)\}^*]$, where $P_1^y(f,t)$ is replaced according to (3.8). Note that according to the representations for $P_2(f,t)$ and $P_1(f,t)$ in (3.5) and (3.6), respectively, the location of the second vector sensor can be thought of as $(y,z) = (-L_y/2, D_0 + L_z/2)$, as $L_y \to 0$, whereas the first vector sensor is located at $(y,z) = (L_y/2, D_0 - L_z/2)$, as $L_y \to 0$. So, using the analogous of (3.21) in the *y* direction we obtain $E[P_2(f,t)\{\dot{P}_1(f,t)\}^*] = -\partial E[P_2(f,t)P_1^*(f,t)]/\partial L_y$, as $L_y \to 0$ $= -\partial C_{P_2P_1}(0,0,L_z,L_y)/\partial L_y$, as $L_y \to 0$. Differentiation of (3.30) with respect to L_y results in

$$\begin{aligned} C_{P_2P_1^y}(L_z) &= E[P_2(f,t)\{P_1^y(f,t)\}^*] = (jk)^{-1}\partial C_{P_2P_1}(0,0,L_z,L_y)/\partial L_y \\ &= \int_{\gamma=0}^{2\pi} w(\gamma)\cos(\gamma)\exp(jk[L_y\cos(\gamma)+L_z\sin(\gamma)])d\gamma, \text{ as } L_y \to 0. \end{aligned} \tag{3.33}$$

If $w(\gamma)$ is even-symmetric around the *z* axis, then with $L_y = 0$ in (3.33) we obtain $E[P_1(f,t)\{P_1^y(f,t)\}^*] = 0$, i.e., the co-located pressure and the *y*-component of the velocity become uncorrelated.

(c) Velocity Correlations: Here we start with the *z*-component of the velocity. We are going to calculate $E[P_2^z(f,t)\{P_1^z(f,t)\}^*] = k^{-2}E[P_2'(f,t)\{P_1'(f,t)\}^*]$, where $P_2^z(f,t)$ and $P_1^z(f,t)$ are replaced according to (3.8). On the other hand, similar to (3.22), one can write $E[P_2'(f,t)\{P_1'(f,t)\}^*] = -\partial^2 E[P_2(f,t)P_1^*(f,t)]/\partial L_z^2 = -\partial^2 C_{P_2P_1}(0,0,L_z,L_y)/\partial L_z^2$. Hence

$$\begin{aligned} C_{P_2^zP_1^z}(L_z) &= E[P_2^z(f,t)\{P_1^z(f,t)\}^*] = -k^{-2}\partial^2 C_{P_2P_1}(0,0,L_z,L_y)/\partial L_z^2 \\ &= \int_{\gamma=0}^{2\pi} w(\gamma)\sin^2(\gamma)\exp(jk[L_y\cos(\gamma)+L_z\sin(\gamma)])d\gamma, \text{as } L_y \to 0, \end{aligned} \tag{3.34}$$

where (3.30) is used to write the integral in (3.34).

Let us now concentrate on the *y*-component of the velocity. In this case the correlation is $E[P_2^y(f,t)\{P_1^y(f,t)\}^*] = k^{-2}E[\dot{P}_2(f,t)\{\dot{P}_1(f,t)\}^*]$, in which $P_2^y(f,t)$ and $P_1^y(f,t)$ are replaced using to (3.8). As mentioned before (3.33), the second and the first vector sensors are located at $(y,z) = (-L_y/2, D_0 + L_z/2)$, and $(y,z) = (L_y/2, D_0 - L_z/2)$, as $L_y \to 0$, respectively. Thus, by using the equivalent of (3.22) in the *y* direction we obtain $E[\dot{P}_2(f,t)\{\dot{P}_1(f,t)\}^*] = -\partial^2 E[P_2(f,t)P_1^*(f,t)]/\partial L_y^2$ as $L_y \to 0 = -\partial^2 C_{P_2P_1}(0,0,L_z,L_y)/\partial L_y^2$ as $L_y \to 0$. Taking the second derivative of (3.30) with respect to L_y results in

$$\begin{aligned} C_{P_2^yP_1^y}(L_z) &= E[P_2^y(f,t)\{P_1^y(f,t)\}^*] = -k^{-2}\partial^2 C_{P_2P_1}(0,0,L_z,L_y)/\partial L_y^2 \\ &= \int_{\gamma=0}^{2\pi} w(\gamma)\cos^2(\gamma)\exp(jk[L_y\cos(\gamma)+L_z\sin(\gamma)])d\gamma, \text{ as } L_y \to 0. \end{aligned} \tag{3.35}$$

The (average) received powers via the pressure-equivalent velocity channels in the *z* and *y* directions are $E[|P_1^z(f,t)|^2]$ and $E[|P_1^y(f,t)|^2]$, respectively. Using (3.34) and (3.35) with $L_y = 0$, and since $\sin^2(\gamma) < 1$ and $\cos^2(\gamma) < 1$, one can easily show

$$E[|P_1^z(f,t)|^2] < 1, \quad E[|P_1^y(f,t)|^2] < 1, \quad E[|P_1^z(f,t)|^2] + E[|P_1^y(f,t)|^2] = 1. \tag{3.36}$$

Therefore, the received powers via the two velocity channels are not equal. However, through both of them together we receive the same total power that a pressure sensor collects, as shown by the last equation in (3.36). Note that in this dissertation the

power received by a pressure sensor is $E[|P_1(f,t)|^2] = C_{P_2P_1}(0,0,0,0) = 1$, obtained from (3.30).

Finally, the correlation between the z and y components of the velocity is $E[P_2^z(f,t)\{P_1^y(f,t)\}^*] = k^{-2}E[P_2'(f,t)\{\dot{P}_1(f,t)\}^*]$, with $P_2^z(f,t)$ and $P_1^y(f,t)$ substituted according to (3.8). A straightforward generalization of (3.22) results in $E[P_2'(f,t)\{\dot{P}_1(f,t)\}^*] = -\partial^2 E[P_2(f,t)P_1^*(f,t)]/\partial L_z \partial L_y$, as $L_y \to 0$ $= -\partial^2 C_{P_2P_1}(0,0,L_z,L_y)/\partial L_2 \partial L_y$,as $L_y \to 0$. By taking the derivatives of (3.30) with respect to L_z and L_y we obtain

$$\begin{aligned} C_{P_2^zP_1^y}(L_z) &= E[P_2^z(f,t)\{P_1^y(f,t)\}^*] = -k^{-2}\partial^2 C_{P_2P_1}(0,0,L_z,L_y)/\partial L_z \partial L_y \\ &= \int_{\gamma=0}^{2\pi} w(\gamma)\sin(\gamma)\cos(\gamma)\exp(jk[L_y\cos(\gamma)+L_z\sin(\gamma)])d\gamma, \text{ as } L_y \to 0. \end{aligned} \tag{3.37}$$

With $L_z = 0$, there are two possibilities for which (3.37) becomes zero: $w(\gamma)$ is even-symmetric with respect to the y axis, or $w(\gamma)$ is even-symmetric around the z axis. In both cases the co-located z and y components of the velocity are uncorrelated.

3.2.1.2 *Frequency correlations for one vector sensor*

(a) Pressure Correlation: Simply with $L_y = L_z = 0$ and $\Delta t = 0$, equations (3.10)-(3.18) in Section 3.1.2 result in $\gamma_2^b = \gamma_1^b = \gamma^b$, $\gamma_2^s = \gamma_1^s = \gamma^s$, $\tau_2^b = \tau_1^b = \tau^b$, $\tau_2^s = \tau_1^s = \tau^s$, the frequency correlation of pressure channel for vertical vector sensor array can be obtained from (3.9) as

$$\begin{aligned} C_{PP}(\Delta f,0,L_z,L_y) &= \Lambda_b \int_{\gamma^b=0}^{\pi} w^b(\gamma^b)\exp[jk(L_y\cos(\gamma)+L_z\sin(\gamma))]\exp[-j2\pi\Delta f\tau^b]d\gamma^b \\ &+ (1-\Lambda_b)\int_{\gamma^s=\pi}^{2\pi} w^s(\gamma^s)\exp[jk(L_y\cos(\gamma)+L_z\sin(\gamma))]\exp[-j2\pi\Delta f\tau^s]d\gamma^s, \text{as } L_y, L_z \to 0. \end{aligned} \tag{3.38}$$

The component $\exp(jk[L_y\cos(\gamma)+L_z\sin(\gamma)])$ is remained here to help illustrating the differentiation process for the velocity channel correlations.

(b) Pressure-Velocity Correlations: Still we look at the *z*-component of the velocity first. Now we need $E[P_1(f,t)\{P_1^z(f,t)\}^*] = (-jk)^{-1}E[P_1(f,t)\{P_1'(f,t)\}^*]$. Similar to the spatial correlation derivation, using (3.23) with $L_y = L_z = 0$ and $\Delta t = 0$, one can obtain

$$\begin{aligned} C_{PP^z}(\Delta f) &= E[P_1(f,t)\{P_1^z(f,t)\}^*] = (jk)^{-1}\partial C_{P_2P_1}(\Delta f, 0, L_z, L_y)/\partial L_z \\ &= \Lambda_b \int_{\gamma^b=0}^{\pi} w^b(\gamma^b)\sin(\gamma^b)\exp[-j2\pi\Delta f\tau^b]d\gamma^b \\ &+ (1-\Lambda_b)\int_{\gamma^s=\pi}^{2\pi} w^s(\gamma^s)\sin(\gamma^s)\exp[-j2\pi\Delta f\tau^s]d\gamma^s. \end{aligned} \tag{3.39}$$

Similarly, replacing $L_y = L_z = 0$ and $\Delta t = 0$ in (3.24) results in

$$\begin{aligned} C_{PP^y}(\Delta f) &= E[P_1(f,t)\{P_1^y(f,t)\}^*] = (jk)^{-1}\partial C_{P_2P_1}(\Delta f, 0, L_z, L_y)/\partial L_y \\ &= \Lambda_b \int_{\gamma^b=0}^{\pi} w^b(\gamma^b)\cos(\gamma^b)\exp[-j2\pi\Delta f\tau^b]d\gamma^b \\ &+ (1-\Lambda_b)\int_{\gamma^s=\pi}^{2\pi} w^s(\gamma^s)\cos(\gamma^s)\exp[-j2\pi\Delta f\tau^s]d\gamma^s. \end{aligned} \tag{3.40}$$

(c) Velocity Correlations: Using (3.9) and (3.23)-(3.27), with $L_y = L_z = 0$ and $\Delta t = 0$, the frequency auto-correlations of z-velocity and y-velocity channel can be expressed as

$$\begin{aligned} C_{P^zP^z}(\Delta f) &= \Lambda_b \int_{\gamma^b=0}^{\pi} w^b(\gamma^b)\sin^2(\gamma^b)\exp[-j2\pi\Delta f\tau^b]d\gamma^b \\ &+ (1-\Lambda_b)\int_{\gamma^s=\pi}^{2\pi} w^s(\gamma^s)\sin^2(\gamma^s)\exp[-j2\pi\Delta f\tau^s]d\gamma^s, \end{aligned} \tag{3.41}$$

$$\begin{aligned} C_{P^yP^y}(\Delta f) &= \Lambda_b \int_{\gamma^b=0}^{\pi} w^b(\gamma^b)\cos^2(\gamma^b)\exp[-j2\pi\Delta f\tau^b]d\gamma^b \\ &+ (1-\Lambda_b)\int_{\gamma^s=\pi}^{2\pi} w^s(\gamma^s)\cos^2(\gamma^s)\exp[-j2\pi\Delta f\tau^s]d\gamma^s, \end{aligned} \tag{3.42}$$

$$\begin{aligned} C_{P^zP^y}(\Delta f) &= \Lambda_b \int_{\gamma^b=0}^{\pi} w^b(\gamma^b)\sin(\gamma^b)\cos(\gamma^b)\exp[-j2\pi\Delta f\tau^b]d\gamma^b \\ &+ (1-\Lambda_b)\int_{\gamma^s=\pi}^{2\pi} w^s(\gamma^s)\sin(\gamma^s)\cos(\gamma^s)\exp[-j2\pi\Delta f\tau^s]d\gamma^s. \end{aligned} \tag{3.43}$$

3.2.1.3 *Temporal correlations for one vector sensor*

(a) Pressure Correlation: Simply with $L_y = L_z = 0$ and $\Delta f = 0$, and using the same approach, the temporal correlation of pressure channel for vertical vector sensor array can be obtained from (3.9) as

$$\begin{aligned} C_{PP}(\Delta t) &= \Lambda_b \int_{\gamma^b=0}^{\pi} w^b(\gamma^b) \exp[jk(L_y \cos(\gamma) + L_z \sin(\gamma))] \exp[j2\pi f_M \cos(\gamma^b - \varphi)\Delta t] d\gamma^b \\ &+ (1-\Lambda_b) \int_{\gamma^s=\pi}^{2\pi} w^s(\gamma^s) \exp[jk(L_y \cos(\gamma) + L_z \sin(\gamma))] \exp[j2\pi f_M \cos(\gamma^s - \varphi)\Delta t] d\gamma^s \\ &, \text{as } L_y, L_z \to 0 \end{aligned} \tag{3.44}$$

(b) Velocity Correlations: From (3.9), using (3.23)-(3.27), with $L_y = L_z = 0$ and $\Delta f = 0$, the time domain auto-correlations of z-velocity and y-velocity channel can be expressed as

$$\begin{aligned} C_{P^z P^z}(\Delta t) &= \Lambda_b \int_{\gamma^b=0}^{\pi} w^b(\gamma^b) \sin^2(\gamma^b) \exp[j2\pi f_M \cos(\gamma^b - \varphi)\Delta t] d\gamma^b \\ &+ (1-\Lambda_b) \int_{\gamma^s=\pi}^{2\pi} w^s(\gamma^s) \sin^2(\gamma^s) \exp[j2\pi f_M \cos(\gamma^s - \varphi)\Delta t] d\gamma^s, \end{aligned} \tag{3.45}$$

$$\begin{aligned} C_{P^y P^y}(\Delta t) &= \Lambda_b \int_{\gamma^b=0}^{\pi} w^b(\gamma^b) \cos^2(\gamma^b) \exp[j2\pi f_M \cos(\gamma^b - \varphi)\Delta t] d\gamma^b \\ &+ (1-\Lambda_b) \int_{\gamma^s=\pi}^{2\pi} w^s(\gamma^s) \cos^2(\gamma^s) \exp[j2\pi f_M \cos(\gamma^s - \varphi)\Delta t] d\gamma^s. \end{aligned} \tag{3.46}$$

The temporal crossing-correlation between the pressure and velocity channels and within the velocity channels are not concerned in this dissertation, but the interesting reader can derive it out simply following the principle of spatial correlation derivation.

3.2.2 A Closed-from Integral-free Correlation Expression

Similarly by using the small spread AOAs by Gaussian PDFs as (3.28) and taking the first-order and second-order Taylor expansion, as shown in Appendix C, and using the characteristic function of a zero-mean Gaussian variable, which is $\int \exp(j\theta x)(2\pi\sigma^2)^{-1/2} \exp[-x^2/(2\sigma^2)] dx = \exp(-\sigma^2\theta^2/2)$ [45], one can obtain the

closed-from integral-free correlation expressions. Since in this section, only the vertical vector sensor array are concerned, which means $L_y = 0$ and $L = L_z$, here we use L instead of L_z to represent the element spacing to simplify the notations.

In what follows we focus on the closed-form integral-free expressions of the spatial correlations for two vector sensors at the same frequency as well as the frequency and temporal correlations for a single vector sensor.

3.2.2.1 *Spatial correlations for two vector sensors at the same frequency*

(a) Pressure correlation: With $\Delta f = \Delta t = 0$ and $L_y = 0$ from (3.28), (3.30) and (3.31), similar to Appendix C, using L to replace L_z, one can obtain the approximated integral-free spatial correlation of pressure channel as

$$\begin{aligned} C_{P_2P_1}(L) = \Lambda_b \exp\left[jkL\sin(\mu_b) - 0.5\sigma_b^2 k^2 L^2 \cos^2(\mu_b)\right] \\ + (1-\Lambda_b)\exp\left[jkL\sin(\mu_s) - 0.5\sigma_s^2 k^2 L^2 \cos^2(\mu_s)\right]. \end{aligned} \tag{3.47}$$

The magnitude of (3.47) is plotted in Figure 3.7 with the comparing of the exact pressure correlation. The close agreement between the two curves verifies the usefulness of the approximate yet simpler pressure spatial correlation model in (3.47).

(b) Pressure-Velocity Correlations: From (3.28), (3.31) and (3.32) we obtain

$$\begin{aligned} C_{P_2P_1^z}(L) = \Lambda_b[\sin(\mu_b) + j\sigma_b^2 kL\cos^2(\mu_b)]\exp\left[jkL\sin(\mu_b) - 0.5\sigma_b^2 k^2 L^2\cos^2(\mu_b)\right] \\ + (1-\Lambda_b)[\sin(\mu_s) + j\sigma_s^2 kL\cos^2(\mu_s)]\exp\left[jkL\sin(\mu_s) - 0.5\sigma_s^2 k^2 L^2\cos^2(\mu_s)\right]. \end{aligned} \tag{3.48}$$

Moreover, (3.28), (3.31) and (3.33) results in

$$\begin{aligned} C_{P_2P_1^y}(L) = \Lambda_b[\cos(\mu_b) - j\sigma_b^2 kL\sin(\mu_b)\cos(\mu_b)]\exp\left[jkL\sin(\mu_b) - 0.5\sigma_b^2 k^2 L^2\cos^2(\mu_b)\right] \\ + (1-\Lambda_b)[\cos(\mu_s) - j\sigma_s^2 kL\sin(\mu_s)\cos(\mu_s)]\exp\left[jkL\sin(\mu_s) - 0.5\sigma_s^2 k^2 L^2\cos^2(\mu_s)\right]. \end{aligned} \tag{3.49}$$

For $L = L_z = 0$, i.e., a single vector sensor, co-located pressure/vertical-velocity and co-located pressure/horizontal-velocity correlations are $\Lambda_b \sin(\mu_b) + (1-\Lambda_b)\sin(\mu_s)$ and

$\Lambda_b \cos(\mu_b) + (1-\Lambda_b)\cos(\mu_s)$, respectively. As an example, let $\Lambda_b = 0.4$, $\sigma_b = \pi/90$ (2°) , $\mu_b = \pi/18$ (10°) , $\sigma_s = \pi/120$ (1.5°) , and $\mu_s = 348\pi/180$ $(348^\circ \equiv -12^\circ)$. This results in -0.055 and 0.98 for P_1/P_1^z and P_1/P_1^y correlations, respectively. Plots of the magnitudes of (3.48) and (3.49) are provided in Figure 3.7. Those correlation results confirm that the upon the small AOA spread and near horizontal mean of AOAs, the velocity-y channel is almost the same as the pressure channel and the velocity-z channel is totally different with them. This phenomenon has been indicated and proved by several figures, for example Figure 3.5 and Figure 3.6.

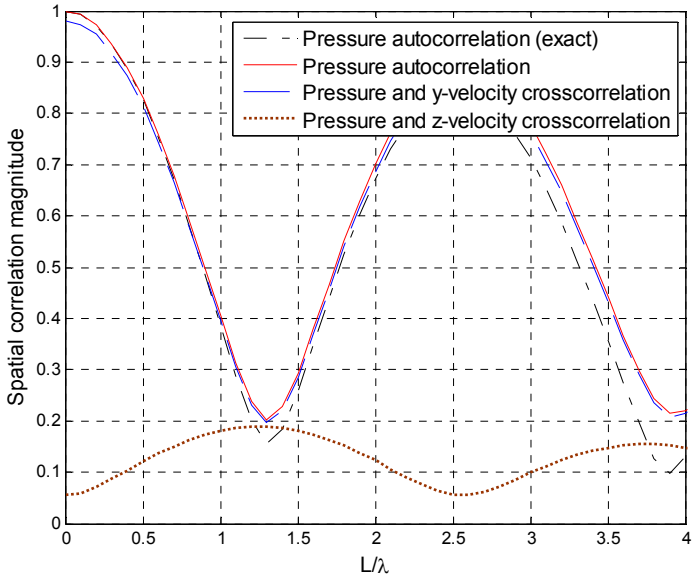

Figure 3.7 The magnitudes of the pressure spatial autocorrelation in (3.47) and pressure-velocity spatial crosscorrelations in (3.48) and (3.49) versus L/λ.

(c) Velocity Correlations: Similarly, from (3.34), (3.35) and (3.37), we can get

$$
\begin{aligned}
&C_{P_2^z P_1^z}(L) \\
&= \Lambda_b[\sin^2(\mu_b) + \sigma_b^2\cos^2(\mu_b) - \sigma_b^4 k^2 L^2 \cos^4(\mu_b) + j2\sigma_b^2 kL\sin(\mu_b)\cos^2(\mu_b)] \\
&\times \exp\left[jkL\sin(\mu_b) - 0.5\sigma_b^2 k^2 L^2 \cos^2(\mu_b)\right] \\
&+ (1-\Lambda_b)[\sin^2(\mu_s) + \sigma_s^2\cos^2(\mu_s) - \sigma_s^4 k^2 L^2 \cos^4(\mu_s) + j2\sigma_s^2 kL\sin(\mu_s)\cos^2(\mu_s)] \\
&\times \exp\left[jkL\sin(\mu_s) - 0.5\sigma_s^2 k^2 L^2 \cos^2(\mu_s)\right],
\end{aligned}
\tag{3.50}
$$

$$
\begin{aligned}
&C_{P_2^y P_1^y}(L) \\
&= \Lambda_b[\cos^2(\mu_b) + \sigma_b^2 \sin^2(\mu_b) - \sigma_b^4 k^2 L^2 \sin^2(\mu_b)\cos^2(\mu_b) - j2\sigma_b^2 kL \sin(\mu_b)\cos^2(\mu_b)] \\
&\times \exp\left[jkL\sin(\mu_b) - 0.5\sigma_b^2 k^2 L^2 \cos^2(\mu_b)\right] \\
&+(1-\Lambda_b)[\cos^2(\mu_s) + \sigma_s^2 \sin^2(\mu_s) - \sigma_s^4 k^2 L^2 \sin^2(\mu_s)\cos^2(\mu_s) - j2\sigma_s^2 kL \sin(\mu_s)\cos^2(\mu_s)] \\
&\times \exp\left[jkL\sin(\mu_s) - 0.5\sigma_s^2 k^2 L^2 \cos^2(\mu_s)\right],
\end{aligned}
\tag{3.51}
$$

$$
\begin{aligned}
&C_{P_2^z P_1^y}(L) \\
&= \Lambda_b \left[(1-\sigma_b^2)\sin(\mu_b)\cos(\mu_b) + \sigma_b^4 k^2 L^2 \sin(\mu_b)\cos^3(\mu_b) - jkL\sigma_b^2 \cos(\mu_b)\{\sin^2(\mu_b) - \cos^2(\mu_b)\}\right] \\
&\times \exp\left[jkL\sin(\mu_b) - 0.5\sigma_b^2 k^2 L^2 \cos^2(\mu_b)\right] \\
&+(1-\Lambda_b)\left[(1-\sigma_s^2)\sin(\mu_s)\cos(\mu_s) + \sigma_s^4 k^2 L^2 \sin(\mu_s)\cos^3(\mu_s) - jkL\sigma_s^2 \cos(\mu_s)\{\sin^2(\mu_s) - \cos^2(\mu_s)\}\right] \\
&\times \exp\left[jkL\sin(\mu_s) - 0.5\sigma_s^2 k^2 L^2 \cos^2(\mu_s)\right].
\end{aligned}
\tag{3.52}
$$

For a single vector sensor, by plugging $L = L_z = 0$ into the above equations we obtain

$$
\begin{aligned}
C_{P^z P^z}(0) &= \Lambda_b[\sin^2(\mu_b) + \sigma_b^2 \cos^2(\mu_b)] + (1-\Lambda_b)[\sin^2(\mu_s) + \sigma_s^2 \cos^2(\mu_s)] \\
&\approx \Lambda_b \sin^2(\mu_b) + (1-\Lambda_b)\sin^2(\mu_s),
\end{aligned}
\tag{3.53}
$$

$$
\begin{aligned}
C_{P^y P^y}(0) &= \Lambda_b[\cos^2(\mu_b) + \sigma_b^2 \sin^2(\mu_b)] + (1-\Lambda_b)[\cos^2(\mu_s) + \sigma_s^2 \sin^2(\mu_s)] \\
&\approx \Lambda_b \cos^2(\mu_b) + (1-\Lambda_b)\cos^2(\mu_s),
\end{aligned}
\tag{3.54}
$$

$$
\begin{aligned}
C_{P^z P^y}(0) &= \Lambda_b(1-\sigma_b^2)\sin(\mu_b)\cos(\mu_b) + (1-\Lambda_b)(1-\sigma_s^2)\sin(\mu_s)\cos(\mu_s) \\
&\approx (1/2)[\Lambda_b \sin(2\mu_b) + (1-\Lambda_b)\sin(2\mu_s)].
\end{aligned}
\tag{3.55}
$$

The almost equal sign $\approx$ in (3.53)-(3.55) comes from the assumption of $\sigma_b, \sigma_s \ll 1$ in this case study. As a numerical example, let $\Lambda_b = 0.4$, $\sigma_b = \pi/90$ (2°), $\mu_b = \pi/18$ (10°), $\sigma_s = \pi/120$ (1.5°), and $\mu_s = 348\pi/180$ $(348^\circ \equiv -12^\circ)$. According to (3.53) and (3.54), the average powers of the vertical and horizontal velocity channels are 0.038 and 0.962, respectively. Furthermore, the correlation between the vertical and horizontal channels is -0.0536, calculated using (3.55). Plots of the magnitudes of (3.50)-(3.52) are provided in Figure 3.8.

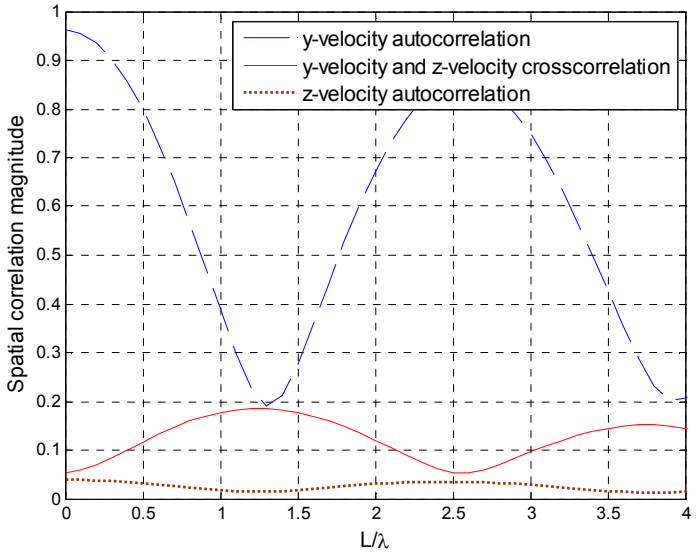

Figure 3.8 The magnitudes of the velocity spatial autocorrelations in (3.50) and (3.51), and velocity-velocity spatial crosscorrelation in (3.52) versus L / λ.

3.2.2.2 *Frequency correlations for one vector sensor*

(a) Pressure correlation: From (3.38), using the same approach as the spatial correlations, one can obtain

$$C_{PP}(\Delta f) = \Lambda_b \exp\left[-j2\pi \csc(\mu_b) T_b \Delta f\right] \exp\left[-2\sigma_b^2 \csc^2(\mu_b) \cot^2(\mu_b) T_b^2 \pi^2 \Delta f^2\right] + (1-\Lambda_b) \exp\left[j2\pi \csc(\mu_s) T_s \Delta f\right] \exp\left[-2\sigma_s^2 \csc^2(\mu_s) \cot^2(\mu_s) T_s^2 \pi^2 \Delta f^2\right]. \quad (3.56)$$

Here $\csc(\mu_b) = \sin^{-1}(\mu_b)$, $\csc(\mu_s) = \sin(\mu_s)^{-1}$, $\cot(\mu_b) = \tan(\mu_b)^{-1}$ and $\cot(\mu_s) = \tan(\mu_s)^{-1}$. $T_b = (D_0 - D)/c$ is the vertical travel time from bottom to *Rx* and $T_s = D/c$ is the vertical travel time from surface to *Rx*. The magnitude of (3.56) is plotted in Figure 3.9, with the comparison of the exact correlation. The close agreement between the two curves verifies the usefulness of the approximate yet simpler pressure frequency correlation model in (3.56).

(b) Pressure-Velocity correlations: From (3.39) and (3.40), one can obtain the following results, respectively

$$
\begin{aligned}
C_{PP^z}(\Delta f) = {} & \Lambda_b[\sin(\mu_b) + j\sigma_b^2 \cot(\mu_b) T_b 2\pi\Delta f] \\
& \times \exp\left[-j \csc(\mu_b) T_b 2\pi\Delta f - 2\sigma_b^2 \csc^2(\mu_b) \cot^2(\mu_b) T_b^2 \pi^2 \Delta f^2\right] \\
& + (1-\Lambda_b)[\sin(\mu_s) - j\sigma_s^2 \cot(\mu_s) T_s 2\pi\Delta f] \\
& \times \exp\left[j \csc(\mu_s) T_s 2\pi\Delta f - 2\sigma_s^2 \csc^2(\mu_s) \cot^2(\mu_s) T_s^2 \pi^2 \Delta f^2\right],
\end{aligned}
\tag{3.57}
$$

$$
\begin{aligned}
C_{PP^y}(\Delta f) = {} & \Lambda_b[\cos(\mu_b) - j\sigma_b^2 \cot(\mu_b) T_b 2\pi\Delta f] \\
& \times \exp\left[-j \csc(\mu_b) T_b 2\pi\Delta f - 2\sigma_b^2 \csc^2(\mu_b) \cot^2(\mu_b) T_b^2 \pi^2 \Delta f^2\right] \\
& + (1-\Lambda_b)[\cos(\mu_s) + j\sigma_s^2 \cot(\mu_s) T_s 2\pi\Delta f] \\
& \times \exp\left[j \csc(\mu_s) T_s 2\pi\Delta f - 2\sigma_s^2 \csc^2(\mu_s) \cot^2(\mu_s) T_s^2 \pi^2 \Delta f^2\right].
\end{aligned}
\tag{3.58}
$$

For $\Delta f = 0$, (3.57) and (3.58) can be simplified to the results given in Subsection 3.2.2.1. The magnitudes of (3.57) and (3.58) are plotted in Figure 3.9.

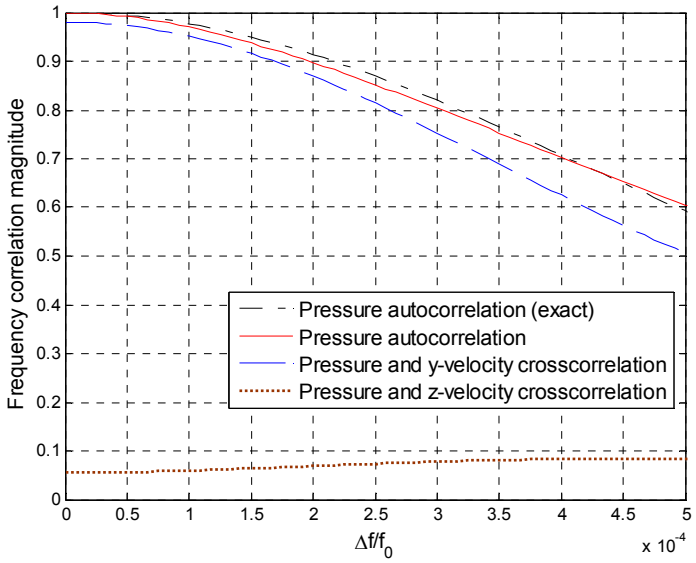

Figure 3.9 The magnitudes of the pressure frequency autocorrelation in (3.56) and the pressure-velocity frequency crosscorrelations in (3.57) and (3.58) versus $\Delta f / f_0$.

(c) Velocity correlations: From (3.41), (3.42) and (3.43), one can obtain the following results at $L_z = 0$, respectively

$$
\begin{aligned}
&C_{P^z P^z}(\Delta f)\\
&=\Lambda_b[\sin^2(\mu_b)+\sigma_b^2\cos^2(\mu_b)-4\pi^2\sigma_b^4\cot^4(\mu_b)\tau_b^2\Delta f^2+j4\pi\sigma_b^2\cos^2(\mu_b)\csc(\mu_b)\tau_b\Delta f]\\
&\times\exp\left[-j2\pi\csc(\mu_b)\tau_b\Delta f-2\pi^2\sigma_b^2\csc^2(\mu_b)\cot^2(\mu_b)\tau_b^2\Delta f^2\right]\\
&+(1-\Lambda_b)[\sin^2(\mu_s)+\sigma_s^2\cos^2(\mu_s)-4\pi^2\sigma_s^4\cot^4(\mu_s)\tau_s^2\Delta f^2-j4\pi\sigma_s^2\cos^2(\mu_s)\csc(\mu_s)\tau_s\Delta f]\\
&\times\exp\left[j2\pi\csc(\mu_s)\tau_s\Delta f-2\pi^2\sigma_s^2\csc^2(\mu_s)\cot^2(\mu_s)\tau_s^2\Delta f^2\right],
\end{aligned}
\tag{3.59}
$$

$$
\begin{aligned}
&C_{P^y P^y}(\Delta f)\\
&=\Lambda_b[\cos^2(\mu_b)+\sigma_b^2\sin^2(\mu_b)-4\pi^2\sigma_b^4\cot^2(\mu_b)\tau_b^2\Delta f^2-j4\pi\sigma_b^2\cos^2(\mu_b)\csc(\mu_b)\tau_b\Delta f]\\
&\times\exp\left[-j2\pi\csc(\mu_b)\tau_b\Delta f-2\pi^2\sigma_b^2\csc^2(\mu_b)\cot^2(\mu_b)\tau_b^2\Delta f^2\right]\\
&+(1-\Lambda_b)[\cos^2(\mu_s)+\sigma_s^2\sin^2(\mu_s)-4\pi^2\sigma_s^4\cot^2(\mu_s)\tau_s^2\Delta f^2+j4\pi\sigma_s^2\cos^2(\mu_s)\csc(\mu_s)\tau_s\Delta f]\\
&\times\exp\left[j2\pi\csc(\mu_s)\tau_s\Delta f-2\pi^2\sigma_s^2\csc^2(\mu_s)\cot^2(\mu_s)\tau_s^2\Delta f^2\right],
\end{aligned}
\tag{3.60}
$$

$$
\begin{aligned}
C_{P^z P^y}(\Delta f)=\Lambda_b&\begin{bmatrix}(1-\sigma_b^2)\sin(\mu_b)\cos(\mu_b)+4\pi^2\sigma_b^4\cot^3(\mu_b)\tau_b^2\Delta f^2\\-j2\pi\sigma_b^2(\cos(\mu_b)-\cos^3(\mu_b)\csc(\mu_b))\tau_b\Delta f\end{bmatrix}\\
&\times\exp\left[-j2\pi\csc(\mu_b)\tau_b\Delta f-2\pi^2\sigma_b^2\csc^2(\mu_b)\cot^2(\mu_b)\tau_b^2\Delta f^2\right]\\
&+(1-\Lambda_b)\begin{bmatrix}(1-\sigma_s^2)\sin(\mu_s)\cos(\mu_s)+4\pi^2\sigma_s^4\cot^3(\mu_s)\tau_s^2\Delta f^2\\+j2\pi\sigma_s^2(\cos(\mu_s)-\cos^3(\mu_s)\csc(\mu_s))\tau_s\Delta f\end{bmatrix}\\
&\times\exp\left[j2\pi\csc(\mu_s)\tau_s\Delta f-2\pi^2\sigma_s^2\csc^2(\mu_s)\cot^2(\mu_s)\tau_s^2\Delta f^2\right].
\end{aligned}
\tag{3.61}
$$

When $\Delta f=0$, (3.59)-(3.61) reduce to (3.53)-(3.55). The plots of the magnitudes of (3.59)-(3.61) are given in Figure 3.10.

3.2.2.3 *Temporal correlations for one vector sensor*

(a) Pressure correlation: Similar to (3.47)-(3.61), from (3.44) the following closed-form pressure channel temporal correlations can be obtained

$$
\begin{aligned}
&C_{PP}(\Delta t)\\
&=\Lambda_b\exp[j2\pi f_M\Delta t\cos(\mu_b-\varphi)]\exp[-2\sigma_b^2\pi^2 f_M^2\Delta t^2\sin^2(\mu_b-\varphi)]\\
&+(1-\Lambda_b)\exp[j2\pi f_M\Delta t\cos(\mu_s-\varphi)]\exp[-2\sigma_s^2\pi^2 f_M^2\Delta t^2\sin^2(\mu_s-\varphi)],
\end{aligned}
\tag{3.62}
$$

The pressure channel temporal correlation, eq. (3.62), is plotted in Figure 3.11 for $\varphi=0^\circ$ and $u=2.5m/s$.

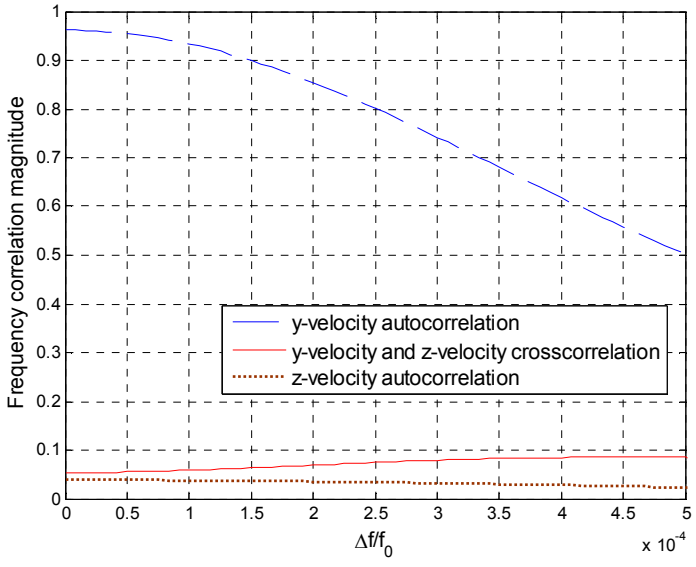

Figure 3.10 The magnitudes of the velocity frequency autocorrelations in (3.59) and (3.60), and velocity-velocity frequency crosscorrelation in (3.61) versus $\Delta f / f_0$.

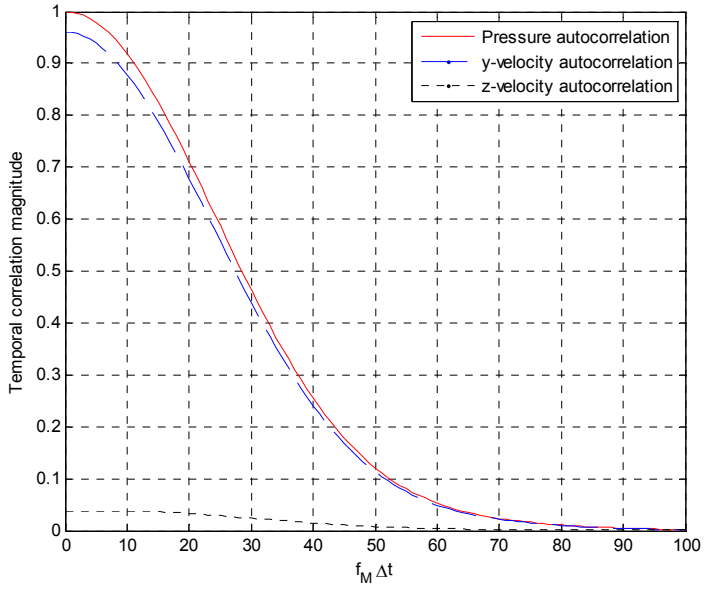

Figure 3.11 The magnitudes of the approximated pressure and velocity channel temporal autocorrelations.

(b) Velocity correlation: By using (3.45) and (3.46), the following closed-form velocity channel temporal correlations can be obtained respectively

$$
\begin{aligned}
&C_{P^z P^z}(\Delta t) \\
&= \Lambda_b \begin{bmatrix} \sin^2(\mu_b) - \sigma_b^2 \cos^2(\mu_b) \\ +4\pi f_M \Delta t \sigma_b^2 \cos(\mu_b)\sin(\mu_b)\sin(\mu_b - \varphi) \\ +4\pi^2 f_M^2 \Delta t^2 \sigma_b^4 \cos^2(\mu_b)\sin^2(\mu_b - \varphi) \end{bmatrix} \exp\begin{bmatrix} j2\pi f_M \Delta t \cos(\mu_b - \varphi) \\ -2\sigma_b^2 \pi^2 f_M^2 \Delta t^2 \sin^2(\mu_b - \varphi) \end{bmatrix} \\
&+(1-\Lambda_b) \begin{bmatrix} \sin^2(\mu_s) - \sigma_s^2 \cos^2(\mu_s) \\ +4\pi f_M \Delta t \sigma_s^2 \cos(\mu_s)\sin(\mu_s)\sin(\mu_s - \varphi) \\ +4\pi^2 f_M^2 \Delta t^2 \sigma_s^4 \cos^2(\mu_s)\sin^2(\mu_s - \varphi) \end{bmatrix} \exp\begin{bmatrix} j2\pi f_M \Delta t \cos(\mu_s - \varphi) \\ -2\sigma_s^2 \pi^2 f_M^2 \Delta t^2 \sin^2(\mu_s - \varphi) \end{bmatrix},
\end{aligned}
\tag{3.63}
$$

$$
\begin{aligned}
&C_{P^y P^y}(\Delta t) \\
&= \Lambda_b \begin{bmatrix} \cos^2(\mu_b) - \sigma_b^2 \sin^2(\mu_b) \\ -4\pi f_M \Delta t \sigma_b^2 \cos(\mu_b)\sin(\mu_b)\sin(\mu_b - \varphi) \\ +4\pi^2 f_M^2 \Delta t^2 \sigma_b^4 \sin^2(\mu_b)\sin^2(\mu_b - \varphi) \end{bmatrix} \exp\begin{bmatrix} j2\pi f_M \Delta t \cos(\mu_b - \varphi) \\ -2\sigma_b^2 \pi^2 f_M^2 \Delta t^2 \sin^2(\mu_b - \varphi) \end{bmatrix} \\
&+(1-\Lambda_b) \begin{bmatrix} \cos^2(\mu_s) - \sigma_s^2 \sin^2(\mu_s) \\ -4\pi f_M \Delta t \sigma_s^2 \cos(\mu_s)\sin(\mu_s)\sin(\mu_s - \varphi) \\ +4\pi^2 f_M^2 \Delta t^2 \sigma_s^4 \sin^2(\mu_s)\sin^2(\mu_s - \varphi) \end{bmatrix} \exp\begin{bmatrix} j2\pi f_M \Delta t \cos(\mu_s - \varphi) \\ -2\sigma_s^2 \pi^2 f_M^2 \Delta t^2 \sin^2(\mu_s - \varphi) \end{bmatrix}.
\end{aligned}
\tag{3.64}
$$

Analytical temporal correlations in (3.62) - (3.64) are plotted in Figure 3.11 as well. Please note that as discussed in Chapter 2, the average pressure channel power is equal to the sum of the average powers of *z* and *y* particle velocity channels. This can also be observed here by having $\Delta t = 0$ in (3.62) - (3.64). Simulation results are also provided to verify analytical expressions.

In the ambient noise field, correlations among the elements of a vector sensor array are calculated in [48]. The emphasis of this manuscript, however, is the development of a geometrical-statistical model for the shallow water waveguide, as shown in Figure 3.2 and analyzed in appendices. Upon using Gaussian PDFs for small spread AOAs, a set of closed-form integral-free expressions are derived. Another focal point of the present dissertation is the emphasis on the frequency domain representation of the acoustic field, e.g., the frequency transfer functions in (3.5) and (3.6). This allows to derive frequency domain correlations that are important for communication system

design. For example, eq. (3.56) can be used to determine the correlation between two Δf -separated tones received by a vector sensor, in a multi-carrier system such as OFDM (orthogonal frequency division multiplexing). Overall, the proposed shallow water geometrical-statistical channel model provides useful expressions for space, frequency and time domain vector sensor correlations, in terms of the physical parameters of the channel such as mean angle of arrivals and angle spreads.

3.2.2.4 *Comparison with measured data*

To experimentally verify the proposed model, in this section we compare the derived pressure correlation function in (3.47) with the measured data of [59]. Once the accuracy of the pressure correlation function is experimentally confirmed, one can take the derivatives of the pressure correlation, to find different types of correlations in a vector sensor array, as discussed in previous sections.

A uniform 33-element array with 0.5 m element spacing was deployed at a 10 km range, where the bottom depth was 103 m [59]. The measurements were conducted at the center frequency of $f_0 = 1.2$ kHz. The empirical vertical correlation of the pressure field, estimated from the measured data, is shown in Figure 3.12. The vertical correlation in [59] is measured with respect to the eighth element from the bottom of the 33-element array. This explains the horizontal axis in Figure 3.12 and the peak value at the eight element. To compare the proposed correlation model in (3.47) with measured correlation, its parameters need to be determined. We chose $\mu_b = 3^{\circ}$ and $\mu_s = 353^{\circ} \equiv -7^{\circ}$, as according to [59], there are two dominant arrivals from these directions. After inserting these numbers into (3.47), the remaining parameters were estimated using a numerical least squares approach. Similarly to [59], the model was compared with the measured correlation over the eight neighboring receivers (elements one to fifteen in Figure 3.12). This resulted in $\Lambda_b = 0.56$, $\sigma_b = 0.04$ and $\sigma_s = 0.14$ rad. The magnitude of the proposed model in (3.47) is plotted in Figure 3.12. The close agreement between the model and

measured correlations in Figure 3.12 indicates the usefulness of the model. As a reference, the exponential model of [59], i.e., $\exp(-L^2/(2\lambda)^2)$ is also included in Figure 3.12. Here $\lambda = 1.2$ m is the wavelength.

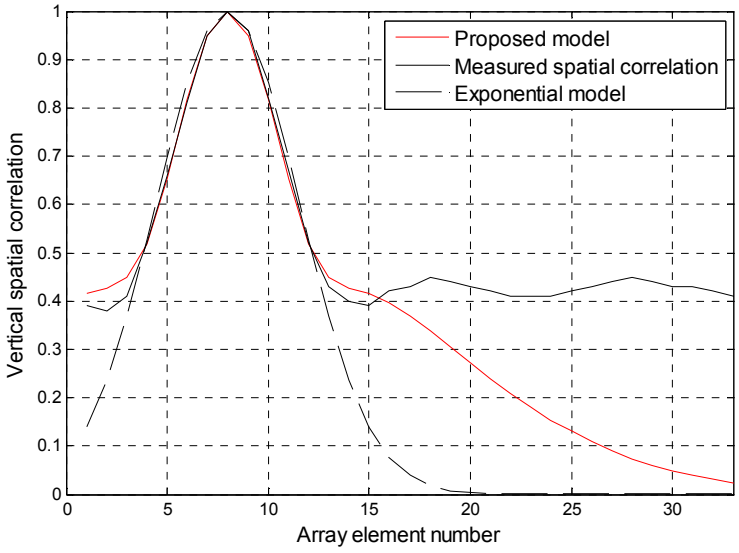

Figure 3.12 Comparison of the proposed model with measured data.

One can observe the proposed model provides a closer match to experimental correlation at the first and fifteenth elements. The main advantage of the proposed model is that it expresses the acoustic field correlation as a function of important physical parameters of the channel such as angle of arrivals and angle spreads. This allows system engineers to understand how these channel parameters affect the correlation, which in turn provides useful guidelines for proper array and system design.

3.3 Summary and Conclusion

In this chapter we have presented a ray-based statistical/geometrical framework for characterization of acoustic vector sensor array correlations in shallow waters. Exact correlation expressions for an arbitrary vector sensor array are derived which relate signal correlations to some key channel parameters such as mean angle of arrivals and angle spreads. Using these expressions one can calculate the correlations of pressure and

velocity channels, in terms of element spacing, frequency separation, time separation, angle of arrivals, water depth and array locations. Closed-form expressions are derived as well for vertical vector sensor array in case of exact correlation expression calculation complex and time consuming. Using those approximated expressions, one can simply calculate the correlations of the pressure and velocity channels. The results of those studies are useful for the design and performance analysis of vector sensor systems and array processing algorithms.

Overall, depending on the AOA of the pressure wave, correlations among pressure and velocity components vary. In the numerical example of Section 3.2, the mean AOA of impinging waves is almost horizontal, as shown in Figure 3.3. This is why in Figure 3.7 and Figure 3.9, crosscorrelation among P and P^y channels are high, whereas P and P^z channels are less correlated. Figure 3.8 and Figure 3.10 further confirm that P^y and P^z channels are almost uncorrelated.

To further confirm the above argument, let us focus on a single vector sensor. Without loss of generality we consider $\Lambda_b = 1$. Then according to the paragraph immediately after (3.49), P/P^y and P/P^z crosscorrelations are given by $\cos(\mu_b)$ and $\sin(\mu_b)$, respectively. For small values of μ_b, i.e., mostly horizontal wave propagation towards the receiver, we note that P/P^y crosscorrelation is high whereas P/P^z crosscorrelation is small. On the other hand, as μ_b approaches 90^o, i.e., nearly vertical AOAs, P/P^y crosscorrelation becomes small whereas P/P^z crosscorrelation is large.

To look at the P^y/P^z crosscorrelattion under the above setup, we use (3.55), which results in a crosscorrelation proportional to $\sin(2\mu_b)$. As expected, for the two extreme cases of mostly horizontal ($\mu_b \approx 0^o$) and vertical ($\mu_b \approx 90^o$) AOAs, P^y and P^z are almost uncorrelated. Crosscorrelation between P^y and P^z reaches its maximum when $\mu_b = 45^o$, as expected. This is the case where AOAs are not biased towards horizontal and vertical directions.

Vector sensor correlations that are calculated in this chapter provide useful guidelines which are highly needed for transceiver design. For example, in the numerical example of Section 3.1.2.3, also discussed at the beginning of this section, the *y* and *z* components of the acoustic particle velocity are nearly uncorrelated for different element spacings and frequency separations. This is true even for a single vector sensor. This means that *y* and *z* channels of a single vector sensor receiver can provide a diversity gain of order two in our numerical example, which in turn reduces the symbol detection error probability.

CHAPTER 4

CHARACTERIZATION OF DELAY AND DOPPLER SPREADS

4.1 Principle and Preparation

In the previous chapter, the complete spatial, frequency and temporal correlations are established and the closed-form integral-free expressions for those correlations are derived as well. Since the frequency and time domain zero crossing rates can be obtained by using the corresponding correlations, and the frequency and time domain zero crossing rates are proportional to the delay and Doppler spreads. One can analyze the delay and Doppler spreads of the underwater pressure and particle velocity channels mathematically by calculating the frequency and time domain ZCRs, respectively. In this chapter, we derive the frequency and time domain ZCRs first, then based on those ZCRs, the channel delay and Doppler spreads of particle velocity channels are discussed.

4.1.1 Zero Crossing Rate

Let $\alpha(t)$ be a real random process with the temporal autocorrelation $\Gamma_\alpha(\Delta t) = E[\alpha(t+\Delta t)\alpha(t)]$. Then the ZCR of $\alpha(t)$, the average number of times that $\alpha(t)$ crosses the threshold zero per unit time, can be calculated according to [45]

$$n_\alpha^t = \frac{1}{\pi}\sqrt{\frac{-\Gamma_\alpha''(\Delta t)\big|_{\Delta t=0}}{\Gamma_\alpha(0)}}, \tag{4.1}$$

where double prime is the second derivative. Similarly, if $\alpha(f)$ is a real random process is the frequency domain, then its ZCR, n_α^f, the average number of times that $\alpha(f)$ crosses the threshold zero per unit frequency, is given by

$$n_\alpha^f = \frac{1}{\pi}\sqrt{\frac{-\Gamma_\alpha''(\Delta f)\big|_{\Delta f=0}}{\Gamma_\alpha(0)}}, \tag{4.2}$$

where $\Gamma_\alpha(\Delta f) = E[\alpha(f+\Delta f)\alpha(f)]$ is the frequency autocorrelation of $\alpha(f)$.

4.1.2 Review of Frequency and Temporal Correlations

Now, we focus on the vector sensor receiver *Rx*, to calculate the delay and Doppler spreads of particle velocity channels. With $L_z = L_y = 0$ in (3.9), it is straight forward to obtain the frequency-time autocorrelation of $P(f,t)$, the time-varying transfer function of the pressure channel, at *Rx*

$$\begin{aligned} &C_{PP}(\Delta f,\Delta t) \\ &= \Lambda_b E_{\gamma^b}\left[\exp[-j2\pi\Delta f T_b/\sin(\gamma^b)]\exp[j2\pi f_M\cos(\gamma^b-\varphi)\Delta t]\right] \\ &+(1-\Lambda_b)E_{\gamma^s}\left[\exp[-j2\pi\Delta f T_s/\sin(\gamma^s)]\exp[j2\pi f_M\cos(\gamma^s-\varphi)\Delta t]\right]. \end{aligned} \tag{4.3}$$

Here $T_b = (D_0 - D)/c$, the vertical travel time from bottom to *Rx* and $T_s = D/c$, the vertical travel time from surface to *Rx*. Eq. (4.3) is obtained because when $L_z = L_y = 0$, equations (3.10)-(3.18) in Section 3.1.2 result in $\gamma_2^b = \gamma_1^b$, $\tau_2^b = \tau_1^b$, $\tau_2^b = T_b/\sin(\gamma^b)$, $\gamma_2^s = \gamma_1^s$, $\tau_2^s = \tau_1^s$ and $\tau_2^s = T_s/\sin(\gamma^s)$. As shown in (3.8), using (3.25) and (3.26), second derivative of (3.9) at $L_z = L_y = 0$ provide the following frequency-time autocorrelations of $P^z(f,t)$ and $P^y(f,t)$ at *Rx*, respectively.

$$\begin{aligned} &C_{P^zP^z}(\Delta f,\Delta t) \\ &= \Lambda_b E_{\gamma^b}\left[\sin^2(\gamma^b)\exp[-j2\pi\Delta f T_b/\sin(\gamma^b)]\exp[j2\pi f_M\cos(\gamma^b-\varphi)\Delta t]\right] \\ &+(1-\Lambda_b)E_{\gamma^s}\left[\sin^2(\gamma^s)\exp[-j2\pi\Delta f T_s/\sin(\gamma^s)]\exp[j2\pi f_M\cos(\gamma^s-\varphi)\Delta t]\right], \end{aligned} \tag{4.4}$$

$$\begin{aligned} &C_{P^yP^y}(\Delta f,\Delta t) \\ &= \Lambda_b E_{\gamma^b}\left[\cos^2(\gamma^b)\exp[-j2\pi\Delta f T_b/\sin(\gamma^b)]\exp[j2\pi f_M\cos(\gamma^b-\varphi)\Delta t]\right] \\ &+(1-\Lambda_b)E_{\gamma^s}\left[\cos^2(\gamma^s)\exp[-j2\pi\Delta f T_s/\sin(\gamma^s)]\exp[j2\pi f_M\cos(\gamma^s-\varphi)\Delta t]\right]. \end{aligned} \tag{4.5}$$

4.1.3 Correlation of Real Part of Channel Transfer Function

To calculate the ZCRs, the correlations between the real parts of $P_1(f,t)$ and $P_2(f,t)$ in (3.5) and (3.6) have to be derived first. This will be needed to compute the ZCR of real channel functions in the next section. If W is complex, then $\mathrm{Re}\{W\} = (W + W^*)/2$. This results in

$$E\left[\mathrm{Re}\{P_2(f+\Delta f,t+\Delta t)\}\,\mathrm{Re}\{P_1(f,t)\}\right] = \frac{1}{2}\mathrm{Re}\left\{C_{P_2P_1}(\Delta f,\Delta t,L_z,L_y)\right\} + \frac{1}{2}\mathrm{Re}\left\{E\left[P_2(f+\Delta f,t+\Delta t)P_1(f,t)\right]\right\}, \tag{4.6}$$

where $C_{P_2P_1}(\Delta f,\Delta t,L_z,L_y)$ is given in (3.9). Based on the statistical properties of phases ψ_i^b and ψ_m^s, independent and uniformly distributed over [0, 2π), it can be verified that the second term on the right hand side of (4.6) is zero. This yields

$$E\left[\mathrm{Re}\{P_2(f+\Delta f,t+\Delta t)\}\,\mathrm{Re}\{P_1(f,t)\}\right] = \frac{1}{2}\mathrm{Re}\left\{C_{P_2P_1}(\Delta f,\Delta t,L_z,L_y)\right\}. \tag{4.7}$$

Similarly, based on the definitions of $P_q^z(f,t)$ and $P_q^y(f,t)$, q = 1, 2, provided after (3.5), we obtain

$$E\left[\mathrm{Re}\{P_2^z(f+\Delta f,t+\Delta t)\}\,\mathrm{Re}\{P_1^z(f,t)\}\right] = \frac{1}{2}\mathrm{Re}\left\{C_{P_2^zP_1^z}(\Delta f,\Delta t,L_z,L_y)\right\}, \tag{4.8}$$

$$E\left[\mathrm{Re}\{P_2^y(f+\Delta f,t+\Delta t)\}\,\mathrm{Re}\{P_1^y(f,t)\}\right] = \frac{1}{2}\mathrm{Re}\left\{C_{P_2^yP_1^y}(\Delta f,\Delta t,L_z,L_y)\right\}, \tag{4.9}$$

where $C_{P_2^zP_1^z}(\Delta f,\Delta t,L_z,L_y)$ and $C_{P_2^yP_1^y}(\Delta f,\Delta t,L_z,L_y)$ are given as (4.4) and (4.5), respectively.

4.2 Frequency and Time Domain ZCRS

To study the delay and Doppler spreads of particle velocity channels, we need to calculate frequency and time domain ZCRs of the real parts of the complex channels $P^z(f,t)$ and $P^y(f,t)$. To do this, first the autocorrelation of the real part of the pressure channel, $\mathrm{Re}\{P(f,t)\}$, should be determined. Using (3.9) and (4.7) we have

$$\Gamma_{\mathrm{Re}\{P\}}(\Delta f,\Delta t) = E\left[\mathrm{Re}\{P(f+\Delta f,t+\Delta t)\}\,\mathrm{Re}\{P(f,t)\}\right] = \frac{1}{2}\mathrm{Re}\left\{C_{PP}(\Delta f,\Delta t)\right\}. \tag{4.10}$$

The autocorrelation of the real part of the vertical particle velocity channel, $\mathrm{Re}\{P^z(f,t)\}$, can be written using (4.4) and (4.8)

$$\Gamma_{\mathrm{Re}\{P^z\}}(\Delta f,\Delta t)=E\left[\mathrm{Re}\{P^z(f+\Delta f,t+\Delta t)\}\,\mathrm{Re}\{P^z(f,t)\}\right]=\frac{1}{2}\mathrm{Re}\{C_{P^zP^z}(\Delta f,\Delta t)\}. \quad (4.11)$$

Similarly, based on (4.5) and (4.9), the autocorrelation of the real part of the horizontal velocity channel, $\mathrm{Re}\{P^y(f,t)\}$, is given by

$$\Gamma_{\mathrm{Re}\{P^y\}}(\Delta f,\Delta t)=E\left[\mathrm{Re}\{P^y(f+\Delta f,t+\Delta t)\}\,\mathrm{Re}\{P^y(f,t)\}\right]=\frac{1}{2}\mathrm{Re}\{C_{P^yP^y}(\Delta f,\Delta t)\}. \quad (4.12)$$

In what follows, first we derive the general expressions for the frequency and time domain ZCRs. Then we show how to obtain the simple closed-form ZCRs for given small spread AOAs.

4.2.1 General Expressions of ZCRs

4.2.1.1 *Frequency domain ZCRs*

Here we have $\Delta t=0$. By inserting (4.3) into (4.10), taking derivative with respect to Δf twice and then replacing Δf with zero, for the pressure channel we obtain

$$-\Gamma''_{\mathrm{Re}\{P\}}(\Delta f,0)\Big|_{\Delta f=0}=\frac{\Lambda_b(2\pi T_b)^2}{2}E_{\gamma^b}\left[\frac{1}{\sin^2(\gamma^b)}\right]+\frac{(1-\Lambda_b)(2\pi T_s)^2}{2}E_{\gamma^s}\left[\frac{1}{\sin^2(\gamma^s)}\right]. \quad (4.13)$$

Similarly, by inserting (4.4) into (4.11) (or (4.5) into (4.12)), differentiation with respect to Δf twice and then replacing Δf with zero, for the vertical (or the horizontal) velocity channel we obtain

$$-\Gamma''_{\mathrm{Re}\{P^z\}}(\Delta f,0)\Big|_{\Delta f=0}=\frac{\Lambda_b(2\pi T_b)^2}{2}+\frac{(1-\Lambda_b)(2\pi T_s)^2}{2}, \quad (4.14)$$

$$-\Gamma''_{\mathrm{Re}\{P^y\}}(\Delta f,0)\Big|_{\Delta f=0}=\frac{\Lambda_b(2\pi T_b)^2}{2}E_{\gamma^b}\left[\frac{\cos^2(\gamma^b)}{\sin^2(\gamma^b)}\right]+\frac{(1-\Lambda_b)(2\pi T_s)^2}{2}E_{\gamma^s}\left[\frac{\cos^2(\gamma^s)}{\sin^2(\gamma^s)}\right]. \quad (4.15)$$

Moreover, by inserting (4.3) ,(4.4) and (4.5) into (4.10), (4.11) and (4.12), respectively, it is easy to verify

$$\Gamma_{\mathrm{Re}\{P\}}(0,0)=\frac{1}{2}, \tag{4.16}$$

$$\Gamma_{\mathrm{Re}\{P^z\}}(0,0)=\frac{\Lambda_b}{2}E_{\gamma^b}\left[\sin^2(\gamma^b)\right]+\frac{(1-\Lambda_b)}{2}E_{\gamma^s}\left[\sin^2(\gamma^s)\right], \tag{4.17}$$

$$\Gamma_{\mathrm{Re}\{P^y\}}(0,0)=\frac{\Lambda_b}{2}E_{\gamma^b}\left[\cos^2(\gamma^b)\right]+\frac{(1-\Lambda_b)}{2}E_{\gamma^s}\left[\cos^2(\gamma^s)\right]. \tag{4.18}$$

To obtain $n^f_{\mathrm{Re}\{P\}}$, $n^f_{\mathrm{Re}\{P^z\}}$ and $n^f_{\mathrm{Re}\{P^y\}}$, frequency domain ZCRs, one needs to simply divide (4.13), (4.14) and (4.15) by (4.16), (4.17) and (4.18), respectively.

4.2.1.2 *Time domain ZCRs*

Now we have $\Delta f=0$. Similarly to the previous frequency domain derivations, we can obtain the following results in time domain

$$-\Gamma''_{\mathrm{Re}\{P\}}(0,\Delta t)\Big|_{\Delta t=0}=\frac{\Lambda_b(2\pi f_M)^2}{2}E_{\gamma^b}\left[\cos^2(\gamma^b-\varphi)\right]+\frac{(1-\Lambda_b)(2\pi f_M)^2}{2}E_{\gamma^s}\left[\cos^2(\gamma^s-\varphi)\right], \tag{4.19}$$

$$\begin{aligned}-\Gamma''_{\mathrm{Re}\{P^z\}}(0,\Delta t)\Big|_{\Delta t=0}&=\frac{\Lambda_b(2\pi f_M)^2}{2}E_{\gamma^b}\left[\sin^2(\gamma^b)\cos^2(\gamma^b-\varphi)\right]\\&\quad+\frac{(1-\Lambda_b)(2\pi f_M)^2}{2}E_{\gamma^s}\left[\sin^2(\gamma^s)\cos^2(\gamma^s-\varphi)\right],\end{aligned} \tag{4.20}$$

$$\begin{aligned}-\Gamma''_{\mathrm{Re}\{P^y\}}(0,\Delta t)\Big|_{\Delta t=0}&=\frac{\Lambda_b(2\pi f_M)^2}{2}E_{\gamma^b}\left[\cos^2(\gamma^b)\cos^2(\gamma^b-\varphi)\right]\\&\quad+\frac{(1-\Lambda_b)(2\pi f_M)^2}{2}E_{\gamma^s}\left[\cos^2(\gamma^s)\cos^2(\gamma^s-\varphi)\right].\end{aligned} \tag{4.21}$$

By dividing (4.19), (4.20) and (4.21) by (4.16), (4.17) and (4.18), respectively, time domain ZCRs $n^t_{\mathrm{Re}\{P\}}$, $n^t_{\mathrm{Re}\{P^z\}}$ and $n^t_{\mathrm{Re}\{P^y\}}$ will be obtained.

4.2.2 Numerical Results

Similar to Section 3.2.2, for Gaussian AOA PDFs with small angle spreads, mathematical expectations in (4.13) - (4.21) can be calculated in closed-forms, using the Taylor series expansions of γ^b and γ^s around μ_b and μ_s, respectively. For example

$$\csc^2(\gamma^b) \approx \csc^2(\mu_b) - 2\csc^2(\mu_b)\cot(\mu_b)(\gamma^b - \mu_b) + \left(\cos(2\mu_b) + 2\right)\csc^4(\mu_b)(\gamma^b - \mu_b)^2, \tag{4.22}$$

where $\csc(\cdot) = 1/\sin(\cdot)$ and $\cot(\cdot) = \cos(\cdot)/\sin(\cdot)$. Since $E_{\gamma^b}[\gamma^b - \mu_b] = 0$ and $E_{\gamma^b}[(\gamma^b - \mu_b)^2] = \sigma_b^2$, (4.22) simplifies to

$$E_{\gamma^b}\left[\csc^2(\gamma^b)\right] \approx \csc^2(\mu_b) + \left(\cos(2\mu_b) + 2\right)\csc^4(\mu_b)\sigma_b^2 \tag{4.23}$$

Following the same approach, one can calculate other $E_{\gamma^b}[\cdot]$ in (4.15) - (4.21) as

$$E_{\gamma^b}\left[\cot^2(\gamma^b)\right] \approx \cot^2(\mu_b) + \left(\cos(2\mu_b) + 2\right)\csc^4(\mu_b)\sigma_b^2, \tag{4.24}$$

$$E_{\gamma^b}\left[\sin^2(\gamma^b)\right] \approx \sin^2(\mu_b) + \cos(2\mu_b)\sigma_b^2, \tag{4.25}$$

$$E_{\gamma^b}\left[\cos^2(\gamma^b)\right] \approx \cos^2(\mu_b) - \cos(2\mu_b)\sigma_b^2, \tag{4.26}$$

$$E_{\gamma^b}\left[\cos^2(\gamma^b - \varphi)\right] \approx \cos^2(\mu_b - \varphi) + \cos(2\mu_b - 2\varphi)\sigma_b^2, \tag{4.27}$$

$$\begin{aligned} &E_{\gamma^b}\left[\sin^2(\gamma^b)\cos^2(\gamma^b - \varphi)\right] \\ &\approx \cos^2(\mu_b - \varphi)\sin^2(\mu_b) + \frac{1}{2}\left(\cos(2\mu_b) + 2\cos(4\mu_b - 2\varphi) - \cos(2\mu_b - 2\varphi)\right)\sigma_b^2, \end{aligned} \tag{4.28}$$

$$\begin{aligned} &E_{\gamma^b}\left[\cos^2(\gamma^b)\cos^2(\gamma^b - \varphi)\right] \\ &\approx \cos^2(\mu_b)\cos^2(\mu_b - \varphi) - \frac{1}{2}\left(\cos(2\mu_b) + 2\cos(4\mu_b - 2\varphi) + \cos(2\mu_b - 2\varphi)\right)\sigma_b^2. \end{aligned} \tag{4.29}$$

Clearly, similar results can be obtained for γ^s , in terms of μ_s and σ_s .

To obtain some insight, we consider a case where the bottom components are dominate, i.e., $\Lambda_b = 1$. Then we provide closed-form frequency and time domain ZCRs in the following subsections.

4.2.2.1 *Frequency domain ZCRs*

By inserting (4.13) - (4.18) into the ZCR formula in (4.2), and using the small angle spread results in , one can show that

$$n^{f}_{\mathrm{Re}\{P\}} = 2T_b\left[\csc^2(\mu_b)+\left(\cos(2\mu_b)+2\right)\csc^4(\mu_b)\sigma_b^2\right]^{\frac{1}{2}}, \tag{4.30}$$

$$n^{f}_{\mathrm{Re}\{P^z\}} = 2T_b\left[\frac{1}{\sin^2(\mu_b)+\cos(2\mu_b)\sigma_b^2}\right]^{\frac{1}{2}}, \tag{4.31}$$

$$n^{f}_{\mathrm{Re}\{P^y\}} = 2T_b\left[\frac{\cot^2(\mu_b)+\left(\cos(2\mu_b)+2\right)\csc^4(\mu_b)\sigma_b^2}{\cos^2(\mu_b)-\cos(2\mu_b)\sigma_b^2}\right]^{\frac{1}{2}}. \tag{4.32}$$

Equations (4.30) - (4.32), normalized by T_b, are plotted in Figure 4.1. Simulation results are also included, which show the accuracy of derived formulas.

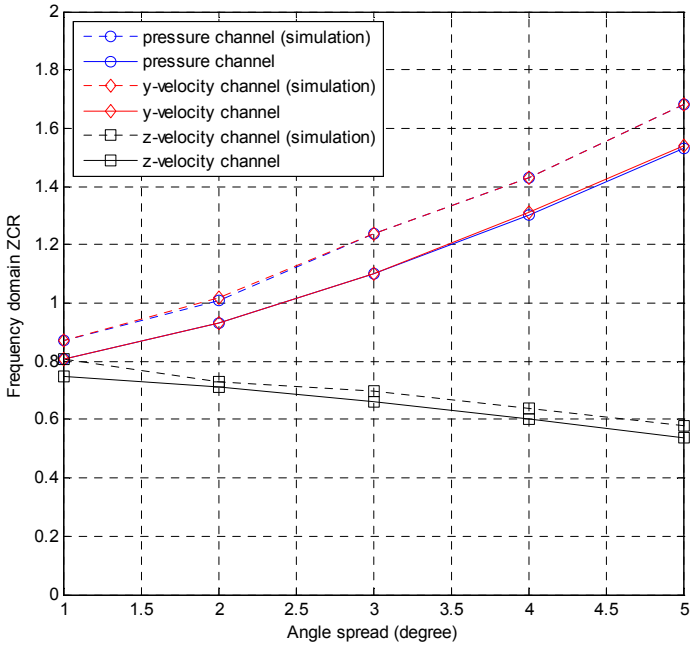

Figure 4.1 Frequency-domain zero crossing rates of particle velocity and pressure channels versus the angle spread σ_b ($\mu_b = 5^\circ$).

Figure 4.1 shows the dependence of frequency domain ZCRs on the angle spread. As expected, the ZCRs of y-velocity and pressure channels are very close. This is because the waves are coming through an almost horizontal direction ($\mu_b = 5$). Increase of ZCRs with the angle spread can be related to the fact that as the angle spread increases,

more rays from different directions reach the receiver. This means larger delay spreads, which results in large ZCRs in the frequency domain. Since in the case considered in Figure 4.1, most of the angle of arrivals are horizontal, the coming rays do not contribute much to the z-velocity channel. This explains the lower values of the frequency domain z-velocity ZCR. This can be better understood by comparing the impulse responses of particle velocity and pressure channels in Figure 4.2. This figure is obtained by plotting (3.5), and its derivatives with respect to y and z, for $\mu_b = 5^\circ$ and $\sigma_b = 3^\circ$. Clearly the impulse response of the z channel is spread over a small range of delays in this example. These are consistent with the delay spread results in [62], obtained via a different approach.

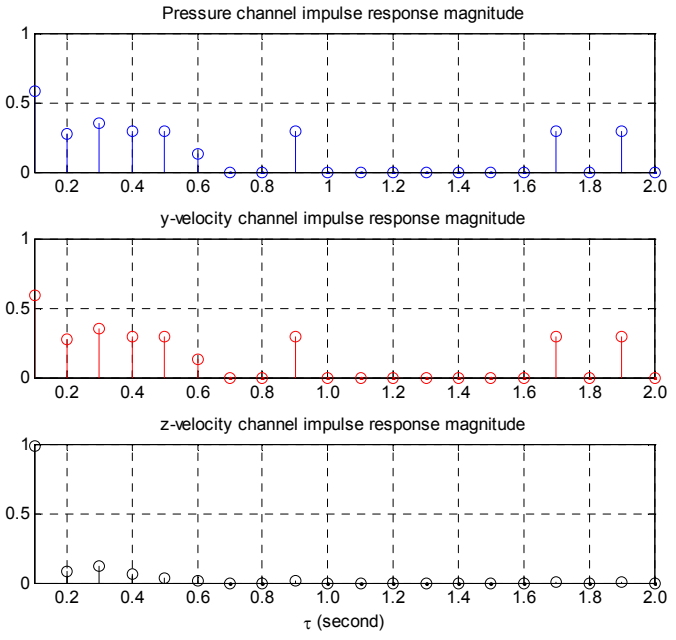

Figure 4.2 Normalized impulse responses of particle velocity channel and pressure channel.

4.2.2.2 *Time domain ZCRs*

By inserting (4.19) - (4.21) and (4.16) - (4.18) into the ZCR formula in (4.1), and using the small angle spread results in (4.25) - (4.29), the following results can be obtained

$$n^t_{\mathrm{Re}\{P\}} = 2 f_M \left[\cos^2(\mu_b - \varphi) + \cos(2\mu_b - 2\varphi)\sigma_b^2\right]^{\frac{1}{2}}, \tag{4.33}$$

$$n^t_{\mathrm{Re}\{P^z\}} = 2f_M \left[\frac{\cos^2(\mu_b - \varphi)\sin^2(\mu_b) + 0.5(\cos(2\mu_b) + 2\cos(4\mu_b - 2\varphi) - \cos(2\mu_b - 2\varphi))\sigma_b^2}{\sin^2(\mu_b) + \cos(2\mu_b)\sigma_b^2} \right]^{\frac{1}{2}}, \tag{4.34}$$

$$n^t_{\mathrm{Re}\{P^y\}} = 2f_M \left[\frac{\cos^2(\mu_b)\cos^2(\mu_b - \varphi) - 0.5(\cos(2\mu_b) + 2\cos(4\mu_b - 2\varphi) + \cos(2\mu_b - 2\varphi))\sigma_b^2}{\cos^2(\mu_b) - \cos(2\mu_b)\sigma_b^2} \right]^{\frac{1}{2}}. \tag{4.35}$$

Equations (4.33) - (4.35), normalized by f_M are plotted Figure 4.3, along with simulation results, which demonstrate the accuracy of the analytical results. According to this figure, time domain ZCRs of particle velocity and pressure channels are about the same, and not dependent much on the angle spread, for the case considered. The analysis conducted in next section for other conditions provides more insight on Doppler spread in these communication channels.

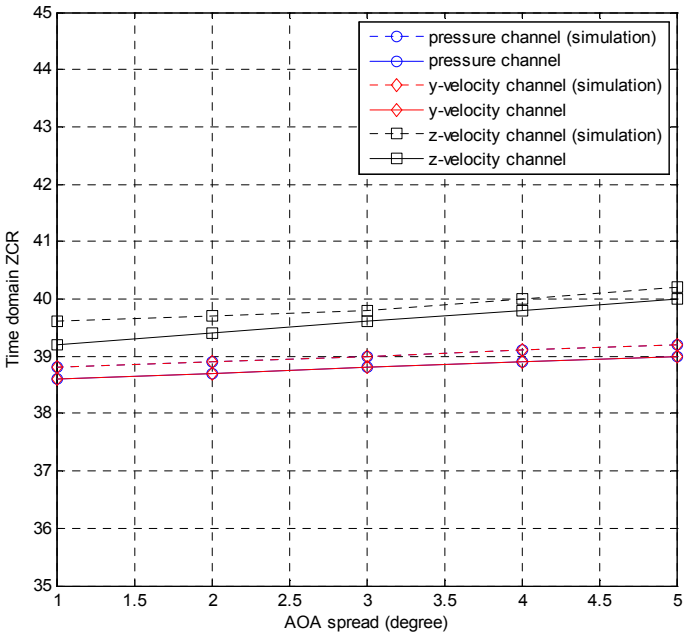

Figure 4.3 Time-domain zero crossing rates of particle velocity and pressure channels versus the angle spread σ_b ($\mu_b = 5^\circ, \varphi = 0^\circ$).

4.2.3 Comparison of Velocity Channel ZCRs

To better understand delay and Doppler spreads of acoustic particle velocity channels, here we consider the practical case where most of the rays in shallow water come along the horizontal direction. This implies that mean AOAs are relatively small, which enable us to further analyze velocity channel ZCRs. Similarly to Section 4.2.2, we consider the case where the bottom rays are dominant. With pressure channel ZCR as a reference, in what follows we compare the ZCRs of particle velocity channels.

4.2.3.1 *Frequency Domain ZCRs:*

Without less of generality and to simplify the notation, we consider the square value of ZCRs. Using (4.30) - (4.32), the frequency domain ZCRs of velocity channels with respect to the pressure channel can be written as

$$\left(\frac{n^f_{\mathrm{Re}\{P^z\}}}{n^f_{\mathrm{Re}\{P\}}}\right)^2 = \frac{1}{\dfrac{\sin^2(\mu_b)+\cos(2\mu_b)\sigma_b^2}{\csc^2(\mu_b)+(\cos(2\mu_b)+2)\csc^4(\mu_b)\sigma_b^2}}, \tag{4.36}$$

$$\left(\frac{n^f_{\mathrm{Re}\{P^y\}}}{n^f_{\mathrm{Re}\{P\}}}\right)^2 = \frac{\dfrac{\cot^2(\mu_b)+(\cos(2\mu_b)+2)\csc^4(\mu_b)\sigma_b^2}{\cos^2(\mu_b)-\cos(2\mu_b)\sigma_b^2}}{\csc^2(\mu_b)+(\cos(2\mu_b)+2)\csc^4(\mu_b)\sigma_b^2}. \tag{4.37}$$

Using the first-order Taylor series expansions $\sin(\mu_b)\approx\mu_b$, and $\cos(\mu_b)$, $\cos(2\mu_b)\approx 1$, when μ_b is small, it is straightforward to verify,

$$\left(\frac{n^f_{\mathrm{Re}\{P^z\}}}{n^f_{\mathrm{Re}\{P\}}}\right)^2 \approx \frac{1}{1+4(\sigma_b/\mu_b)^2+3(\sigma_b/\mu_b)^4}, \tag{4.38}$$

$$\left(\frac{n^f_{\mathrm{Re}\{P^y\}}}{n^f_{\mathrm{Re}\{P\}}}\right)^2 \approx \frac{1}{1-\sigma_b^2}. \tag{4.39}$$

According to (4.38), ZCR of the z-velocity channel can be smaller than the pressure channel, whereat (4.39) shows the ZCRs of the y-velocity channel and pressure channels are nearly the same.

4.2.3.2 *Time Domain ZCRs:*

Based on (4.33) - (4.35), time-domain ZCRs of *z* and *y* velocity channels with respect to the pressure channel are given

$$\left(\frac{n^t_{\mathrm{Re}\{P^z\}}}{n^t_{\mathrm{Re}\{P\}}}\right)^2 = \frac{\cos^2(\mu_b-\varphi)\sin^2(\mu_b)+0.5(\cos(2\mu_b)+2\cos(4\mu_b-2\varphi)-\cos(2\mu_b-2\varphi))\sigma_b^2}{\left(\cos^2(\mu_b-\varphi)+\cos(2\mu_b-2\varphi)\sigma_b^2\right)\left(\sin^2(\mu_b)+\cos(2\mu_b)\sigma_b^2\right)}, \tag{4.40}$$

$$\left(\frac{n^t_{\mathrm{Re}\{P^y\}}}{n^t_{\mathrm{Re}\{P\}}}\right)^2 = \frac{\cos^2(\mu_b)\cos^2(\mu_b-\varphi)-0.5(\cos(2\mu_b)+2\cos(4\mu_b-2\varphi)+\cos(2\mu_b-2\varphi))\sigma_b^2}{\left(\cos^2(\mu_b-\varphi)+\cos(2\mu_b-2\varphi)\sigma_b^2\right)\left(\cos^2(\mu_b)-\cos(2\mu_b)\sigma_b^2\right)}. \tag{4.41}$$

For $\varphi = 0$ and using the first order Taylor series mentioned previously, equations (4.40) and (4.41) simplify to

$$\left(\frac{n^t_{\mathrm{Re}\{P^z\}}}{n^t_{\mathrm{Re}\{P\}}}\right)^2 \approx \frac{1}{1+\sigma_b^2}, \tag{4.42}$$

$$\left(\frac{n^t_{\mathrm{Re}\{P^y\}}}{n^t_{\mathrm{Re}\{P\}}}\right)^2 \approx 1-2\sigma_b^2. \tag{4.43}$$

On the other hand, $\varphi = \frac{\pi}{2}$ simplifies (4.40) and (4.41) to

$$\left(\frac{n^t_{\mathrm{Re}\{P^z\}}}{n^t_{\mathrm{Re}\{P\}}}\right)^2 \approx \frac{1}{1-\left(\sigma_b/\mu_b\right)^4}, \tag{4.44}$$

$$\left(\frac{n^t_{\mathrm{Re}\{P^y\}}}{n^t_{\mathrm{Re}\{P\}}}\right)^2 \approx \frac{1+\left(\sigma_b/\mu_b\right)^2}{1-\left(\sigma_b/\mu_b\right)^2}. \tag{4.45}$$

Here we observe that when the receiver moves horizontally towards the transmitter, ZCRs of z and y velocity channels are almost the same as the pressure channel ZCR, according to (4.42) and (4.43). When the receiver moves vertically towards the bottom, there ratios could be somewhat different. Given the shallow depth of the channel, this holds only over a short period of time.

4.3 Summary and Conclusion

In this chapter, a zero crossing framework is developed to study the delay and Doppler spreads in multipath underwater acoustic particle velocity and pressure channels. The delay and Doppler spreads are calculated by deriving closed-form expressions for the channel zero-crossing rates in frequency and time, respectively. These expressions show how velocity channel delay and Doppler spreads may depend on some key parameters of the channel such as mean angle of arrival and angle spread. The advantage of the proposed velocity channel delay spread analysis here via frequency domain ZCR is that it provides analytical expressions such as (4.31) and (4.32). These types of expressions quantify the delay spreads of acoustic particle velocity and pressure channels in terms of key channel parameters such as mean angle of arrivals and angle spreads. The results are useful for design and performance predication of vector sensor systems that operate in acoustic particle velocity channels.

CHAPTER 5

CONCLUSION AND FUTURE WORKS

5.1 Conclusion and Remarks

In this dissertation, the new idea about the underwater acoustic communication is introduced and developed by using the acoustic vector sensor receiver and taking the advantage of the particle velocity channels. Basic system equations for such a receiver are derived and channel equalization using these sensors is formulated. Signal and noise power characteristics, delay spread and channel correlations in such sensors are also investigated. Via extensive simulations under different propagation scenarios, the performance of a vector sensor equalizer is determined and compared with single and multiple pressure sensor receivers.

Following the single user vector sensor system, a multiple users system is proposed that does not need spreading codes. Performance of a vector sensor receiver for three users is investigated as well. The BER of the proposed multiuser space-time coded vector sensor system is close to the BER of the single user system. This means that the data symbols of the three users are successfully separated and estimated using a vector sensor without reduction in the transmission rate. This is particularly useful in highly bandwidth-constrained underwater channels.

In Chapter 3 we have presented a ray-based statistical/geometrical framework for characterization of acoustic vector sensor array correlations in shallow waters. Exact correlation expressions for an arbitrary vector sensor array are derived. Using these expressions one can calculate the exact correlations of pressure and velocity channels, in terms of element spacing, frequency and time separation, angle of arrivals, water depth and array locations. Then the useful approximate correlation expressions for vertical vector sensor arrays are also derived, when angle spreads are small. The simple close-form approximation provides the sub-accurate but much easier method to calculate those

correlations. The comparison with the exact correlation and the experiment correlation results prove the usefulness of the approximation. The results of those correlation analysis are required for the design and performance assessment of single user [30][31] and multiuser [60][61] underwater communication systems that operate through acoustic particle velocity channels.

Based on the frequency and temporal correlations, a zero crossing framework is developed to study the delay and Doppler spreads for multipath underwater acoustic particle velocity and pressure channels in Chapter 4. The delay and Doppler spreads are calculated by deriving closed-form expressions for the channel zero-crossing rates in frequency and time, respectively. These expressions show how velocity channel delay and Doppler spreads may depend on some key parameters of the channel such as mean angle of arrival and angle spread. The results are useful for design and performance predication of vector sensor systems that operate in acoustic particle velocity channels

In summary, we have shown that small size of the vector sensor receiver in the proposed system is noteworthy, as the compact vector sensor measures all particle velocity channels at a single point in space. This is important for systems which have size limitations such as unmanned underwater vehicles.

5.2 Suggestion for Future Researches

With this new underwater communication system setup, all aspects of this communication system need to be investigated such as channel estimation methods, better equalizer, etc. At the same time, with the introducing of the particle velocity channels into the wireless acoustic communication area, more detailed channel characteristics are waiting for uncover. Through the different ways, mathematical and experimental, the more channel characteristics, for example, channel capacities, need to be figured out.

As the RF communication, when a new communication system is built up, from transmitter to the receiver, there are a lot of possible optimizations for each part of the communication system. Since the shallow water acoustic channel is a multipath channel with severe delay spread, which is usually defined as sparse channel. The channel estimation is important for system performance. Using any possible the channel estimation methods for sparse channel, introduced in the literatures, one needs to establish a way for the particle velocity channels estimation.

On the other hand, when the channel estimation is not easy to obatin, the equalizer will be the major issue to improve the system performance. In this dissertation, the simple zero forcing and MSE equalizer are applied to evaluate the system BER performance. However, both of above equalizer are according to the perfect acknowledgement of channel information. In case of channel information absent, the blind and less complex equalizers are necessary. Or when the first order channel information is unknown but the second order channel information can be extracted, how can we design the optimal equalizer? Similar to the wireless RF communication, there are many possible optimizations, such that coding and interleaving methods, modulation schemes, etc. For this new underwater acoustic communication system via vector sensor receiver, there are still a lot of blank need to be fulfilled.

APPENDIX A

A CLOSED-FORM CORRELATION FOR THE PRESSURE CHANNEL

When angle spreads are small and $L \ll \min(D, D_0 - D)$, one can approximate the AOAs in (3.5) and (3.6) as $\gamma_{i,1}^b \approx \gamma_{i,2}^b \approx \gamma_i^b$ and $\gamma_{m,1}^s \approx \gamma_{m,2}^s \approx \gamma_m^s$, where γ_i^b and γ_m^s are shown in Figure 3.2. Furthermore, the traveled distances can be approximated as $\xi_{i,1}^b \approx \xi_{i,2}^b \approx \xi_i^b$ and $\xi_{m,1}^s \approx \xi_{m,2}^s \approx \xi_m^s$, with ξ_i^b and ξ_m^s depicted in Figure 3.2. Note that each delay is the traveled distance divided by the sound speed *c*. Therefore all the delays in (3.5) and (3.6) can be approximated by $\tau_{i,1}^b \approx \tau_{i,2}^b \approx \tau_i^b$ and $\tau_{m,1}^s \approx \tau_{m,2}^s \approx \tau_m^s$, where $\tau_i^b = \xi_i^b / c$ and $\tau_m^s = \xi_m^s / c$. According to Figure 3.2, it is easy to verify that $\sin(\gamma_i^b) = (D_0 - D) / \xi_i^b$ and $-\sin(\gamma_m^s) = D / \xi_m^s$. Hence

$$\begin{aligned} \tau_i^b &= T_b \big/ \sin(\gamma_i^b), \ 0 < \gamma_i^b < \pi, \\ \tau_m^s &= -T_s \big/ \sin(\gamma_m^s), \ \pi < \gamma_m^s < 2\pi. \end{aligned} \tag{A.1}$$

The parameters $T_b = (D_0 - D)/c$ and $T_s = D/c$ in (A.1) denote the vertical travel times from the sea bottom to the array center, and from the sea surface to the array center, respectively. Clearly the range of γ_m^s in (A.1) implies that $-1 \le \sin(\gamma_m^s) < 0$, which makes τ_m^s non-negative, as expected. In general we have $T_b \le \tau_i^b < \infty, \ \forall i$, and $T_s \le \tau_m^s < \infty, \ \forall m$. Now (3.5) and (3.6) can be simplified as follows

$$\begin{aligned} P_1(f,t) = &\left(\frac{\Lambda_b}{N^b}\right)^{1/2} \sum_{i=1}^{N^b} a_i^b \exp(j\psi_i^b) \exp(jk[y\cos(\gamma_i^b) + z\sin(\gamma_i^b)]) \\ &\exp(-j2\pi f T_b \big/ \sin(\gamma_i^b)) \exp(j2\pi f_M \cos(\gamma_i^b - \varphi)t)\Big|_{\substack{y=L_y/2,\\ z=D-L_z/2}} \\ &+ \left(\frac{1-\Lambda_b}{N^s}\right)^{1/2} \sum_{m=1}^{N^s} a_m^s \exp(j\psi_m^s) \exp(jk[y\cos(\gamma_m^s) + z\sin(\gamma_m^s)]) \\ &\exp(j2\pi f T_s \big/ \sin(\gamma_m^s)) \exp(j2\pi f_M \cos(\gamma_m^s - \varphi)t)\Big|_{\substack{y=L_y/2,\\ z=D-L_z/2}}, \end{aligned} \tag{A.2}$$

$$\begin{aligned} P_2(f,t) = &\left(\frac{\Lambda_b}{N^b}\right)^{1/2} \sum_{i=1}^{N^b} a_i^b \exp(j\psi_i^b) \exp(jk[y\cos(\gamma_i^b) + z\sin(\gamma_i^b)]) \\ &\exp(-j2\pi f T_b \big/ \sin(\gamma_i^b)) \exp(j2\pi f_M \cos(\gamma_i^b - \varphi)t)\Big|_{\substack{y=-L_y/2,\\ z=D+L_z/2}} \\ &+ \left(\frac{1-\Lambda_b}{N^s}\right)^{1/2} \sum_{m=1}^{N^s} a_m^s \exp(j\psi_m^s) \exp(jk[y\cos(\gamma_m^s) + z\sin(\gamma_m^s)]) \\ &\exp(j2\pi f T_s \big/ \sin(\gamma_m^s)) \exp(j2\pi f_M \cos(\gamma_m^s - \varphi)t)\Big|_{\substack{y=-L_y/2,\\ z=D+L_z/2}}. \end{aligned} \tag{A.3}$$

Due to the uniform distribution of all the phases $\{\psi_i^b\}_i$ and $\{\psi_m^s\}_m$ over $[0,2\pi)$ we have $E[\exp(\pm j\psi_i^b)] = E[\exp(\pm j\psi_m^s)] = 0,\ \forall i,m$. This results in $E[\exp(\pm j\psi_i^b)\exp(\pm j\psi_m^s)] = 0,\ \forall i,m$, because all the phases are independent. Similarly we have $E[\exp(j\psi_i^b)\exp(-j\psi_{\tilde{i}}^b)] = 0,\ \forall i \neq \tilde{i}$ and $E[\exp(j\psi_m^s)\exp(-j\psi_{\tilde{m}}^s)] = 0,\ \forall m \neq \tilde{m}$. Clearly the last two expressions become 1, when $i = \tilde{i}$ and $m = \tilde{m}$. Therefore, after substituting (A.2) and (A.3) into $C_{P_2P_1}(\Delta f, \Delta t, L_z, L_y) = E[P_2(f+\Delta f, t+\Delta t)P_1^*(f,t)]$, only the following two single summations remain

$$
\begin{aligned}
&C_{P_2P_1}(\Delta f, \Delta t, L_z, L_y) \\
&= \frac{\Lambda_b}{N^b}\sum_{i=1}^{N^b}\left\{\begin{array}{l} E[(a_i^b)^2]\exp(jk[L_y\cos(\gamma_i^b) + L_z\sin(\gamma_i^b)]) \\ \exp(-jT_b 2\pi\Delta f / \sin(\gamma_i^b))\exp(j2\pi f_M\cos(\gamma_i^b - \varphi)\Delta t)\end{array}\right\} \\
&+ \frac{(1-\Lambda_b)}{N^s}\sum_{m=1}^{N^s}\left\{\begin{array}{l} E[(a_m^s)^2]\exp(jk[L_y\cos(\gamma_m^s) + L_z\sin(\gamma_m^s)]) \\ \exp(jT_s 2\pi\Delta f / \sin(\gamma_m^s))\exp(j2\pi f_M\cos(\gamma_m^s - \varphi)\Delta t)\end{array}\right\},
\end{aligned}
\tag{A.4}
$$

The terms $E[(a_i^b)^2]/N^b$ and $E[(a_m^s)^2]/N^s$ in (A.4) represent the normalized (average) powers received from the two scatterers S_i^b and S_m^s on the sea bottom and its surface, respectively. Let $\sum_{i=1}^{N^b} E[(a_i^b)^2]/N^b = 1$ and $\sum_{m=1}^{N^s} E[(a_m^s)^2]/N^s = 1$. We also define $w^b(\gamma^b)$ and $w^s(\gamma^s)$ as the probability density functions (PDFs) of the AOAs of the waves coming from the sea bottom and its surface, respectively, such that $0 < \gamma^b < \pi$ and $\pi < \gamma^s < 2\pi$. When N^b and N^s are large, one can think of $E[(a_i^b)^2]/N^b$ and $E[(a_m^s)^2]/N^s$ as the normalized powers received through the infinitesimal angles $d\gamma^b$ and $d\gamma^s$, respectively, centered at the AOAs γ_i^b and γ_m^s. Thus, with the chosen normalizations $\sum_{i=1}^{N^b} E[(a_i^b)^2]/N^b = 1$ and $\sum_{m=1}^{N^s} E[(a_m^s)^2]/N^s = 1$, we can write $E[(a_i^b)^2]/N^b = w^b(\gamma_i^b)d\gamma^b$ and $E[(a_m^s)^2]/N^s = w^s(\gamma_m^s)d\gamma^s$. These relations allow the summations in (A.4) to be replaced by integrals

$$
\begin{aligned}
&C_{P_2P_1}(\Delta f, \Delta t, L_z, L_y) \\
&= \Lambda_b \int_{\gamma^b=0}^{\pi} \left\{ \begin{array}{l} w^b(\gamma^b)\exp[-jk(L_y\cos(\gamma^b)+L_z\sin(\gamma^b))] \\ \exp[-jT_b 2\pi\Delta f / \sin(\gamma^b)]\exp[j2\pi f_M \cos(\gamma^b-\varphi)\Delta t]d\gamma^b \end{array} \right\} \\
&+(1-\Lambda_b) \int_{\gamma^s=\pi}^{2\pi} \left\{ \begin{array}{l} w^s(\gamma^s)\exp[-jk(L_y\cos(\gamma^s)+L_z\sin(\gamma^s))] \\ \exp[jT_s 2\pi\Delta f / \sin(\gamma^s)]\exp[j2\pi f_M \cos(\gamma^s-\varphi)\Delta t]d\gamma^s \end{array} \right\}.
\end{aligned}
\tag{A.5}
$$

Note that according to (A.5) we have $C_P(0,0,0,0) = \Lambda_b + (1-\Lambda_b) = 1$, which represents the convenient unit (total average) received pressure power. The factor $0 \le \Lambda_b \le 1$ was defined to stand for the amount of the power coming from the sea bottom, whereas $1-\Lambda_b$ shows the power coming from the surface.

APPENDIX B

THE HIGH ORDER APPROXIMATION OF THE PRESSURE CHANNEL CORRELATIONS

Exact correlation expressions include integrals over AOAs which are time consuming to compute. For small angle spread and under certain conditions such as small spacing between array elements, useful integral-free approximation, for vertical and horizontal arrays can be obtained using (3.19) and (3.20).

B.1 Vertical Vector Sensor Array

For $L = L_z << \min(D, D_0 - D)$ and $L_y = 0$ and using $\sqrt{1+x} \approx 1 + (x/2)$ when $|x| << 1$, distances ξ_1^b, ξ_2^b, ξ_1^s and ξ_2^s given in (3.14)-(3.17) can be approximated as

$$\begin{aligned} \xi_1^b &\approx [(D_0 - D) + L\sin^2(\gamma^b)/2]/\sin(\gamma^b), \\ \xi_2^b &\approx [(D_0 - D) - L\sin^2(\gamma^b)/2]/\sin(\gamma^b), \\ \xi_1^s &\approx -[D - (L\sin^2(\gamma^s)/2)]/\sin(\gamma^s), \\ \xi_2^s &\approx -[D + (L\sin^2(\gamma^s)/2)]/\sin(\gamma^s). \end{aligned} \tag{B.1}$$

Then substituting (B.1) into (3.10)-(3.13), results in

$$\begin{aligned} \sin(\gamma_2^b) - \sin(\gamma_1^b) &\approx L\sin^3(\gamma^b)/(D_0 - D), \\ \sin(\gamma_2^s) - \sin(\gamma_1^s) &\approx -L\sin^3(\gamma^s)/D, \end{aligned} \tag{B.2}$$

$$\begin{aligned} \sin(\gamma_2^b) + \sin(\gamma_1^b) &\approx 2\sin(\gamma^b), \\ \sin(\gamma_2^s) + \sin(\gamma_1^s) &\approx 2\sin(\gamma^s), \end{aligned} \tag{B.3}$$

$$\begin{aligned} \tau_1^b - \tau_2^b &\approx L\sin(\gamma^b)/c, \\ \tau_1^s - \tau_2^s &\approx L\sin(\gamma^s)/c, \end{aligned} \tag{B.4}$$

$$\begin{aligned} \tau_2^b &\approx (D_0 - D)/(c\sin(\gamma^b)), \\ \tau_2^s &\approx -D/(c\sin(\gamma^s)). \end{aligned} \tag{B.5}$$

By substituting (B.2)-(B.5) into (3.19), we obtain the approximation given in (B.6) below.

$$C_{P_2P_1}(\Delta f,\Delta t,L)=\Lambda_b\int_{\gamma^b=0}^{\pi}\left\{\begin{array}{l} w^b(\gamma^b)\exp\left[jkL\dfrac{D}{D_0-D}\sin^3(\gamma^b)+2jkL\sin(\gamma^b)\right] \\ \exp\left[-j\dfrac{2\pi\Delta f(D_0-D)}{c\sin(\gamma^b)}\right]\exp\left[j2\pi f_M\cos(\gamma^b-\varphi)\Delta t\right]d\gamma^b \end{array}\right\} \\ +(1-\Lambda_b)\int_{\gamma^s=\pi}^{2\pi}\left\{\begin{array}{l} w^s(\gamma^s)\exp\left[-jkL\sin^3(\gamma^s)+2jkL\sin(\gamma^s)\right] \\ \exp\left[j\dfrac{2\pi\Delta fD}{c\sin(\gamma^s)}\right]\exp\left[j2\pi f_M\cos(\gamma^s-\varphi)\Delta t\right]d\gamma^s \end{array}\right\}. \tag{B.6}$$

B.2 Horizontal Vector Sensor Array

Here, we have $L=L_y<<\min(D,D_0-D)$ and $L_z=0$. The distances ξ_1^b, ξ_2^b, ξ_1^s and ξ_2^s given in (3.14)-(3.17) can be similarly approximated as

$$\begin{aligned} \xi_1^b &\approx[(D_0-D)-(L\sin(\gamma^b)\cos(\gamma^b))/2]/\sin(\gamma^b),\\ \xi_2^b &\approx[(D_0-D)+(L\sin^2(\gamma)\cos(\gamma^b))/2]/\sin(\gamma^b),\\ \xi_1^s &\approx-[D+(L\sin(\gamma^s)\cos(\gamma^s))/2]/\sin(\gamma^s),\\ \xi_2^s &\approx-[D-(L\sin(\gamma^s)\cos(\gamma^s))/2]/\sin(\gamma^s). \end{aligned} \tag{B.7}$$

Substitution (B.7) into (3.10)-(3.13), results in

$$\begin{aligned} \sin(\gamma_2^b)-\sin(\gamma_1^b) &\approx-\frac{L}{D_0-D}\left(\frac{\cos(\gamma^b)-\cos(3\gamma^b)}{4}\right),\\ \sin(\gamma_2^s)-\sin(\gamma_1^s) &\approx\frac{L}{D}\left(\frac{\cos(\gamma^s)-\cos(3\gamma^s)}{4}\right), \end{aligned} \tag{B.8}$$

$$\begin{aligned} \cos(\gamma_2^b)+\cos(\gamma_1^b) &\approx 2\cos(\gamma^b),\\ \cos(\gamma_2^s)+\cos(\gamma_1^s) &\approx 2\cos(\gamma^s), \end{aligned} \tag{B.9}$$

$$\begin{aligned} \tau_1^b-\tau_2^b &\approx-L\cos(\gamma^b)/c,\\ \tau_1^s-\tau_2^s &\approx-L\cos(\gamma^s)/c, \end{aligned} \tag{B.10}$$

$$\begin{aligned} T_2^b &\approx(D_0-D)/(c\sin(\gamma^b)),\\ T_2^s &\approx-D/(c\sin(\gamma^s)). \end{aligned} \tag{B.11}$$

Therefore, the space-frequency correlation in (3.20) for the horizontal array can be approximated as (B.12).

$$
\begin{aligned}
&C_{P_2P_1}(\Delta f, \Delta t, L) \\
&= \Lambda_b \int_{\gamma^b=0}^{\pi} \left\{ \begin{array}{l} w^b(\gamma^b) \exp\left[-jkL(1+\frac{D}{4(D_0-D)})\cos(\gamma^b) + jkL\frac{D}{4(D_0-D)}\cos(3\gamma^b) \right] \\ \exp\left[-j\frac{2\pi\Delta f(D_0-D)}{c\sin(\gamma^b)} \right] \exp\left[j2\pi f_M \cos(\gamma^b-\varphi)\Delta t \right] d\gamma^b \end{array} \right\} \\
&+ (1-\Lambda_b) \int_{\gamma^s=\pi}^{2\pi} \left\{ \begin{array}{l} w^s(\gamma^s) \exp\left[-jkL(1-\frac{D}{4D_0})\cos(\gamma^s) - jkL\frac{D}{4D_0}\cos(3\gamma^s) \right] \\ \exp\left[j\frac{2\pi\Delta fD}{c\sin(\gamma^s)} \right] \exp\left[j2\pi f_M \cos(\gamma^s-\varphi)\Delta t \right] d\gamma^s \end{array} \right\}.
\end{aligned}
\tag{B.12}
$$

APPENDIX C

THE APPROXIMATION CORRELATION DERIVATION

Similarly we model the small spread AOAs by Gaussian PDFs as (3.28). And the first-order Taylor expansion of γ^b around μ_b gives the following results

$$\begin{aligned}
&\cos(\gamma^b) \approx \cos(\mu_b) - \sin(\mu_b)(\gamma^b - \mu_b), \\
&\sin(\gamma^b) \approx \sin(\mu_b) + \cos(\mu_b)(\gamma^b - \mu_b), \\
&\frac{1}{\sin(\gamma^b)} \approx \frac{1}{\sin(\mu_b)} - \frac{1}{\sin(\mu_b)}\frac{1}{\tan(\mu_b)}(\gamma^b - \mu_b) \quad , \\
&\cos(\gamma^b - \varphi) \approx \cos(\mu_b - \varphi) - \sin(\mu_b - \varphi)(\gamma^b - \mu_b)
\end{aligned} \tag{C.1}$$

Of course similar relations can be obtained for γ^s . The utility of these first-order expansions comes from the considered small angle spreads, which means the AOAs γ^b and γ^s are mainly concentrated around μ_b and μ_s , respectively. By substituting these relations into (3.9), $C_{P_2P_1}(\Delta f, \Delta t, L_z, L_y)$ can be written as

$$\begin{aligned}
&C_{P_2P_1}(\Delta f, \Delta t, L_z, L_y) \\
&\approx \Lambda_b \exp\left(jkL_y \cos(\mu_b) + jkL_z \sin(\mu_b) - j\csc(\mu_b)2\pi T_b \Delta f + j2\pi f_M \cos(\mu_b - \varphi)\Delta t \right) \\
&\times \int_{\gamma^b=0}^{\pi} w^b(\gamma^b) \exp\left[j \begin{pmatrix} -kL_y \sin(\mu_b) + kL_z \cos(\mu_b) \\ +2\pi \csc(\mu_b)\cot(\mu_b) T_b \Delta f - 2\pi f_M \sin(\mu_b - \varphi)\Delta t \end{pmatrix} (\gamma^b - \mu_b) \right] d\gamma^b \\
&+ (1 - \Lambda_b) \exp\left(jkL_y \cos(\mu_s) + jkL_z \sin(\mu_s) + j\csc(\mu_s)2\pi T_s \Delta f + j2\pi f_M \cos(\mu_s - \varphi)\Delta t \right) \\
&\times \int_{\gamma^s=\pi}^{2\pi} w^s(\gamma^s) \exp\left[j \begin{pmatrix} -kL_y \sin(\mu_s) + kL_z \cos(\mu_s) \\ -2\pi \csc(\mu_s)\cot(\mu_s) T_s \Delta f + 2\pi f_M \sin(\mu_s - \varphi)\Delta t \end{pmatrix} (\gamma^s - \mu_s) \right] d\gamma^s ,
\end{aligned} \tag{C.2}$$

Here, $\csc(\bullet) = 1/\sin(\bullet)$ and $\cot(\bullet) = 1/\tan(\bullet)$ .The integrals in (C.2) resemble the characteristic function of a zero-mean Gaussian variable, which is $\int \exp(j\theta x)(2\pi\sigma^2)^{-1/2} \exp[-x^2/(2\sigma^2)]dx = \exp(-\sigma^2\theta^2/2)$ [45] . This simplifies (C.2) to the following closed form

$$
\begin{aligned}
&C_{P_2P_1}(\Delta f, \Delta t, L_z, L_y) \\
&= \Lambda_b \exp\left[j\left(kL_y \cos(\mu_b) + kL_z \sin(\mu_b) - j \csc(\mu_b) 2\pi T_b \Delta f + j2\pi f_M \cos(\mu_b - \varphi)\Delta t\right)\right] \\
&\times \exp\left[-0.5\sigma_b^2 \left(-kL_y \sin(\mu_b) + kL_z \cos(\mu_b) + 2\pi \csc(\mu_b)\cot(\mu_b) T_b \Delta f - 2\pi f_M \sin(\mu_b - \varphi)\Delta t\right)^2 \right] \\
&+ (1-\Lambda_b) \exp\left[j\left(kL_y \cos(\mu_s) + kL_z \sin(\mu_s) + j \csc(\mu_s) 2\pi T_s \Delta f + j2\pi f_M \cos(\mu_s - \varphi)\Delta t\right)\right] \\
&\times \exp\left[-0.5\sigma_s^2 \left(-kL_y \sin(\mu_s) + kL_z \cos(\mu_s) - 2\pi \csc(\mu_s)\cot(\mu_s) T_s \Delta f + 2\pi f_M \sin(\mu_s - \varphi)\Delta t\right)^2 \right].
\end{aligned}
\tag{C.3}
$$

According to (C.3), we have $C_{P_2P_1}(0,0,0,0) = 1$, consistent with the convention of unit (total average) received pressure power, introduced in Appendix A. By taking the derivatives of (C.3) with respect to L_z and L_y as listed in (3.23)-(3.27), closed-form expressions for a variety of correlations in vector sensor receivers can be obtained.

REFERENCES

[1] D. B. Kilfoyle and A. B. Baggeroer, "The state of the art in underwater acoustic telemetry," *IEEE J. Oceanic Eng*., vol. 25, pp. 4-27, 2000.

[2] M. Stojanovic, J. A. Catipovic and J. G. Proakis, "Reduced-complexity spatial and temporal processing of underwater acoustic communication signals," *J. Acoust. Soc. Am.*, vol. 98, pp. 961-972, 1995.

[3] M. Stojanovic, J. A. Catipovic, and J. G. Proakis, "Phase-coherent digital communications for underwater acoustic channels," *IEEE J. Oceanic Eng*., vol. 19, pp. 100–111, Jan. 1994.

[4] A. Song, M. Badiey, and V. K. McDonald, "Multichannel combining and equalization for underwater acoustic MIMO channels," in *Proc. MTS/IEEE Oceans*, Kobe, Japan, 2008.

[5] S. Roy, T. M. Duman, V. McDonald, and J. G. Proakis, "High rate communication for underwater acoustic channels using multiple transmitters and space-time coding: Receiver structures and experimental results," *IEEE J. Oceanic Eng*., vol. 32, pp. 663–688, 2007.

[6] H. C. Song,W. S. Hodgkiss,W. A. Kuperman,W. J. Higley, K. Raghukumar, and T. Akal, "Spatial diversity in passive time reversal communications," *J. Acoust. Soc. Am.*, vol. 120, pp. 2067-2076, 2006.

[7] D. B. Kilfoyle, J. C. Preisig, and A. B. Baggeroer, "Spatial modulation experiments in the underwater acoustic channel," *IEEE J. Oceanic Eng.*, vol. 30, pp. 406-415, 2005.

[8] H. F. Olson, "Mass controlled electrodynamic microphones: the ribbon microphone," *J. Acoust. Soc. Am.*, vol. 3, pp. 56-68, 1931.

[9] M. E. Higgins, "DIFAR system overview," in *Proc. Workshop Directional Acoustic Sensors (CD-ROM)*, New Port, RI, 2001.

[10] M. T. Silvia and R. T. Richards, "A theoretical and experimental investigation of low-frequency acoustic vector sensors," in *Proc. MTS/IEEE Oceans*, Biloxi, MS, 2002, pp. 1886-1897.

[11] Proc. AIP Conf. *Acoustic Particle Velocity Sensors: Design, Performance, and Applications*, Mystic, CT, 1995.

[12] *Proc. Workshop Directional Acoustic Sensors* (CD-ROM), New Port, RI, 2001.

[13] A. Nehorai and E. Paldi, "Acoustic vector-sensor array processing," *IEEE Trans. Signal Processing*, vol. 42, pp. 2481-2491, 1994.

[14] M. Hawkes and A. Nehorai, "Acoustic vector-sensor beamforming and Capon direction estimation," *IEEE Trans. Signal Processing*, vol. 46, pp. 2291-2304, 1998.

[15] B. Hochwald and A. Nehorai, "Identifiability in array processing models with vector-sensor applications," *IEEE Trans. Signal Processing*, vol. 44, pp. 83-95, 1996.

[16] M. D. Zoltowski and K. T. Wong, "Closed-form eigenstructure-based direction finding using arbitrary but identical subarrays on a sparse uniform Cartesian array grid," *IEEE Trans. Signal Processing*, vol. 48, pp. 2205-2210, 2000.

[17] M. Hawkes and A. Nehorai, "Wideband source localization using a distributed acoustic vector-sensor array," *IEEE Trans. Signal Processing*, vol. 51, pp. 1479-1491, 2003.

[18] A. D. Pierce, *Acoustics: An Introduction to Its Physical Principles and Applications*, 2nd ed., Acoustic Soc. Am., 1989.

[19] B. A. Cray, V. M. Evora, and A. H. Nuttall, "Highly directional acoustic receivers," *J. Acoust. Soc. Am.*, vol. 113, pp. 1526-1532, 2003.

[20] B. A. Cray and A. H. Nuttall, "Directivity factors for linear arrays of velocity sensors," *J. Acoust. Soc. Am.*, vol. 110, pp. 324-331, 2001.

[21] T. B. Gabrielson, "Design problems and limitations in vector sensors," in *Proc. Workshop Directional Acoustic Sensors (CD-ROM)*, New Port, RI, 2001.

[22] T. C. Yang, "Temporal resolutions of time-reversal and passive-phase conjugation for underwater acoustic communications," *IEEE J. Oceanic Eng.*, vol. 28, pp. 229–245, 2003.

[23] C. C. Tsimenidis, O. R. Hinton, A. E. Adams, and B. S. Sharif, "Underwater acoustic receiver employing direct-sequence spread spectrum and spatial diversity combining for shallow-water multi-access networking," *IEEE J. Oceanic Eng.*, vol. 26, pp. 594–603, 2001.

[24] S. N. Diggavi, N. Al-Dhahir and A. R. Calderbak, "Algebraic properties of space-time block codes in intersymbol interference multiple-access channels," *IEEE Trans. Inform. Theory*, vol. 49, pp. 2403-2414, 2003.

[25] W. M. Younis, A. H. Sayed and N. Al-Dhahir, "Efficient adaptive receivers for joint equalization and interference cancellation in multiuser space-time block-coded systems," *IEEE Trans. Signal Processing*, vol. 51, pp. 2849-2862, 2003.

[26] E. G. Larsson and P. Stoica, *Space-time Block Coding for Wireless Communications*. Cambridge, UK: Cambridge University Press, 2003.

[27] N. Al-Dhahir, "Single-carrier frequency-domain equalization for space-time block-coded transmissions over broadband wireless channels," in *Proc. IEEE Int. Symp. Personal, Indoor, Mobile Radio Commun*., San Diego, CA, 2001, pp. 143–146.

[28] S. M. Alamouti, "A simple transmit diversity technique for wireless communications," *IEEE J. Select. Areas Commun*., vol. 16, pp.1451-1458, 1998.

[29] S. Barbarossa, *Multiantenna Wireless Communication Systems*. Norwood, MA: Artech House, 2005.

[30] A. Abdi and H. Guo, "A new compact multichannel receiver for underwater wireless communication networks," *IEEE Trans. Wireless Commun.*, vol. 8, pp. 3326-3329, 2009.

[31] A. Abdi, H. Guo and P. Sutthiwan, "A new vector sensor receiver for underwater acoustic communication," in *Proc. MTS/IEEE Oceans*, Vancouver, BC, Canada, 2007.

[32] P. C. Etter, *Underwater Acoustic Modeling and Simulation*, 3rd ed., New York: Spon, 2003.

[33] M. O. Damen, A. Abdi, and M. Kaveh, "On the effect of correlated fading on several space-time coding and detection schemes," in *Proc. IEEE Vehic. Technol. Conf.*, Atlantic City, NJ, 2001, pp. 13-16.

[34] M. Chiani, M. Z. Win and A. Zanella, "On the capacity of spatially correlated MIMO Rayleigh-fading channels," *IEEE Trans. Inform. Theory*, vol. 49, pp. 2363-2371, 2003.

[35] V. K. Nguyen and L. B. White, "Joint space-time trellis decoding and channel estimation in correlated fading channels," *IEEE Signal Processing Lett.*, vol. 11, pp. 633-636, 2004.

[36] C. B. Ribeiro, E. Ollila and V. Koivunen, "Stochastic maximum-likelihood method for MIMO propagation parameter estimation," *IEEE Trans. Signal Processing*, vol. 55, pp. 46-55, 2007.

[37] C. B. Ribeiro, A. Richter and V. Koivunen, "Joint angular- and delay-domain MIMO propagation parameter estimation using approximate ML method," *IEEE Trans. Signal Processing*, vol. 55, pp. 4775-4790, 2007.

[38] A. Abdi and M. Kaveh, "Parametric modeling and estimation of the spatial characteristics of a source with local scattering," in *Proc. IEEE Int. Conf. Acoust., Speech, Signal Processing*, Orlando, FL, 2002, pp. 2821-2824.

[39] K. Witrisal, "On estimating the RMS delay spread from the frequency-domain level crossing rate," *IEEE Commun. Lett*., vol. 5, pp. 287-289, 2001.

[40] K. Witrisal, Y. Kim and R. Prasad, "A new method to measure parameters of frequency-selective radio channels using power measurements," *IEEE Trans. Commun*., vol. 49, pp. 1788-1800, 2001.

[41] H. Zhang and A. Abdi, "On the average crossing rates in selection diversity," *IEEE Trans. Wireless Commun*., vol. 6, pp. 448-451, 2007.

[42] N. C. Beaulieu and X. Dong. "Level crossing rate and average fade duration of MRC and EGC diversity in Ricean fading," *IEEE Trans. Commun*., vol. 51, pp. 722-726, 2003.

[43] C. Bjerrum-Niese, L. Bjorno, M. A. Pinto and B. Quellec, "A simulation tool for high data-rate acoustic communication in a shallow-water, time-varying channel," *IEEE J. Ocean. Eng*., vol. 21, pp143-149, 1996.

[44] J. Clay Shipps and K. Deng, "A miniature vector sensor for line array applications," in *Proc. MTS/IEEE Oceans*, San Diego, CA, 2003, pp. 2367-2370.

[45] A. Papoulis, *Probability, Random Variables, and Stochastic Processes*, 3rd ed., Singapore: McGraw-Hill, 1991.

[46] H. Cox, "Spatial correlation in arbitrary noise fields with application to ambient sea noise," *J. Acoust. Soc. Am.*, vol. 54, pp. 1289-1301, 1973.

[47] W. Magnus, F. Oberhettinger, and R. P. Soni, *Formulas and Theorems for the Special Functions of Mathematical Physics*, 3rd ed., New York: Springer, 1966.

[48] M. Hawkes and A. Nehorai, "Acoustic vector-sensor correlations in ambient noise," *IEEE J. Oceanic Eng.*, vol. 26, pp. 337-347, 2001.

[49] J. G. Proakis, *Digital Communications*, 4th ed., New York: McGraw-Hill, 2001.

[50] J. R. Barry, E. A. Lee and D. G. Messerschmitt, *Digital Communication*, 3rd ed., Boston, MA: Kluwer, 2004.

[51] A. Duncan and A. Maggi. Underwater acoustic propagation modeling software. [Online]. Available: http://www.cmst.curtin.edu.au/

[52] S. M. Kay, *Fundamentals of Statistical Signal Processing: Estimation Theory*. Englewood Cliffs, NJ: PTR Prentice-Hall, 1993, pp. 529-530.

[53] P. S. Duke, "Direct-sequence spread-spectrum modulation for utility packet transmission in underwater acoustic communication networks," M.S. thesis, Dept. Elec. Comp. Eng., Naval Postgraduate School, Monterey, CA, 2002.

[54] P. Sutthiwan, "Multichannel underwater communication receivers," M.S. project report, Dept. Elec. Comp. Eng., New Jersey Institute of Technology, Newark, NJ, 2006.

[55] T. S. Rappaport, *Wireless Communications: Principles and Practice*, 2nd ed., Upper Saddle River, NJ: Prentice Hall PTR, 2002.

[56] H. L. Van Trees, *Optimum Array Processing*. New York: Wiley, 2002.

[57] A. Abdi, J. A. Barger, and M. Kaveh, "A parametric model for the distribution of the angle of arrival and the associated correlation function and power spectrum at the mobile station," *IEEE Trans. Vehic. Technol.*, vol. 51, pp. 425-434, 2002.

[58] A. Abdi and M. Kaveh, "A space-time correlation model for multielement antenna systems in mobile fading channels," *IEEE J. Select. Areas Commun.*, vol. 20, pp. 550-560, 2002.

[59] T. C. Yang, "A study of spatial processing gain in underwater acoustic communications," *IEEE J. Oceanic Eng.*, vol. 32, pp. 689-709, 2007.

[60] H. Guo and A. Abdi, "Multiuser underwater communication with space-time block codes and acoustic vector sensors," in *Proc. MTS/IEEE Oceans*, Quebec City, QC, Canada, 2008.

[61] A. Song, M. Badiey, P. Hursky and A. Abdi, "Time reversal receivers for underwater acoustic communication using vector sensors," in *Proc. MTS/IEEE Oceans*, Quebec City, QC, Canada, 2008.

[62] H. Guo, A. Abdi, A. Song and M. Badiey., "Correlations in underwater acoustic pressure and particle velocity channels," in *Proc. Conf. Inform. Sci. Syst*., Johns Hopkins University, Baltimore, MD, 2009, pp. 913-918.